Max-Planck-Institut
für Meteorologie

MAX-PLANCK-GESELLSCHAFT

International Max Planck Research School
on Earth System Modelling

Climate and ocean variability during the last millennium in paleo-observations and Earth system model simulations

Eduardo Moreno Chamarro

Hamburg 2016

Berichte zur Erdsystemforschung
Reports on Earth System Science

184
2016

Hinweis

Die Berichte zur Erdsystemforschung werden vom Max-Planck-Institut für Meteorologie in Hamburg in unregelmäßiger Abfolge herausgegeben.

Sie enthalten wissenschaftliche und technische Beiträge, inklusive Dissertationen.

Die Beiträge geben nicht notwendigerweise die Auffassung des Instituts wieder.

Die "Berichte zur Erdsystemforschung" führen die vorherigen Reihen "Reports" und "Examensarbeiten" weiter.

Notice

The Reports on Earth System Science are published by the Max Planck Institute for Meteorology in Hamburg. They appear in irregular intervals.

They contain scientific and technical contributions, including Ph. D. theses.

The Reports do not necessarily reflect the opinion of the Institute.

The "Reports on Earth System Science" continue the former "Reports" and "Examensarbeiten" of the Max Planck Institute.

Anschrift / Address

Max-Planck-Institut für Meteorologie
Bundesstrasse 53
20146 Hamburg
Deutschland

Tel./Phone: +49 (0)40 4 11 73 - 0
Fax: +49 (0)40 4 11 73 - 298

name.surname@mpimet.mpg.de
www.mpimet.mpg.de

Layout

Bettina Diallo and Norbert P. Noreiks
Communication

Copyright

Climate and ocean variability during the last millennium in paleo-observations and Earth system model simulations

Dissertation with the aim of achieving a doctoral degree
at the Faculty of Mathematics, Informatics and Natural Sciences
Department of Earth Sciences of Universität Hamburg

submitted by

Eduardo Moreno Chamarro

Hamburg 2016

Eduardo Moreno Chamarro

Max-Planck-Institut für Meteorologie
Bundesstrasse 53
20146 Hamburg

Tag der Disputation: 13.7.2016

Folgende Gutachter empfehlen die Annahme der Dissertation:

Prof. Dr. Gerhard Schmiedl
Dr. Johann H. Jungclaus

Title picture:
Winter Landscape by Caspar David Friedrich (National Gallery, London) 1811. The harsh and severe winters that Europe experienced during the Little Ice Age, between the 15th and 19th centuries, did not only lead to social catastrophes and human hardships; they also inspired artists to depict the nature they were facing, however cruel it might be. This winter scene is a beatiful example, in which the artist, Caspar David Friedrich, represents the hope for salvation through faith.

Berichte zur Erdsystemforschung / Max-Planck-Institut für Meteorologie 184
Reports on Earth System Science / Max Planck Institute for Meteorology 2016

ISSN 1614-1199

The illusion that we understand the past fosters overconfidence in our ability to predict the future

Thinking, Fast and Slow
Daniel Kahneman

Contents

Abstract

Reconstructed climate changes in the North Atlantic, Arctic, and European regions during the past millennium are commonly associated with variations in the Atlantic meridional overturning circulation (AMOC) or in the North Atlantic Oscillation (NAO). However, newer studies do not completely support these hypotheses and suggest, instead, a more important role of the North Atlantic subpolar gyre (SPG). This thesis therefore investigates SPG dynamics above decadal time scales in a three-member ensemble of transient climate simulations for the past millennium performed with a state-of-the-art Earth system model. Our modeling results shall thus offer a physical interpretation of the climatic phenomena reconstructed in this region and period.

We first study simulated decadal cold events in the subpolar North Atlantic of features similar to events reconstructed in the 14th and 15th centuries. The simulated events are mainly attributed to internal regional climate variability. Their underlying general mechanism entails a feedback loop that is driven by a SPG weakening and deep convection shutdown, but not by a hemispheric climate reorganization or AMOC slowdown. Climate deterioration in the Labrador Sea and South Greenland during such events is further compatible with conditions that could have led to the failure of the Norse settlements in these centuries.

We continue by investigating a simulated abrupt weakening shift in the SPG strength. This shift resembles reconstructed evidence of a transition between a stronger and weaker SPG during the relatively warm medieval climate and cold Little Ice Age (LIA) respectively, although model and data differ in the timing of occurrence. In the model, the SPG shift triggers multicentennial anomalies in the North Atlantic climate driven by long-lasting internal feedbacks relating anomalous oceanic and atmospheric circulation, sea ice extent, and upper-ocean salinity in the Labrador Sea, but not persistent changes in the AMOC or NAO. The simulated shift itself is caused by a rapid increase in the Arctic freshwater export to the Labrador Sea, which can be forced, although not necessarily, by volcanic activity. Internal climate variability therefore explains the different timing in the reconstructed and simulated LIA's onset.

We finally explore the role of the SPG-related northward heat transport in setting the seasonal patterns and variability of the cold anomalies that are reconstructed over Europe in winter and summer during the LIA. In winter, the simulated reduced heat transport in the 15th to 18th centuries causes widespread changes in the atmospheric circulation over Europe that entail a regional amplification of the LIA cooling, with anomalous easterlies and reduced westerlies, and increased frequency of atmospheric blocking events. In summer, by contrast, European cooling is caused by an externally forced reduction in the Earth's energy input, but not by persistent changes in atmospheric or oceanic circulation, unlike in winter. Neither of these two mechanisms is, nonetheless, related to changes in the AMOC or NAO. Sensitivity experiments further suggest that the solar forcing alone cannot suffice to trigger the LIA, although the Maunder solar minimum might be necessary to deepen and lengthen it into the 18th century.

To summarize, this thesis shows that SPG, and not AMOC or NAO, dynamics alone allow explaining the nature of the most relevant climate changes in North Atlantic, Arctic and European regions during the past millennium.

Zusammenfassung

Rekonstruktionen des vorindustriellen Klimas weisen charakteristische langfristige Schwankungen auf, wie den Übergang von einer relativ warmen mittelalterlichen Klimaanomalie (MCA) zu einer relativ kalten Kleinen Eiszeit (LIA). Als dynamische Ursachen für diese Entwicklung werden oft Schwankungen der meridionalen Umwälzzirkulation im Atlantischen Ozean (AMOC) oder der Nordatlantischen Oszillation (NAO) genannt. Neuere Studien weisen dagegen auf eine bedeutende Rolle der gross-skaligen ozeanischen Wirbelsysteme, insbesondere des nordatlantischen Subpolarwirbels (SPG), hin. In dieser Arbeit untersuchen wir die Dynamik des SPG auf Zeitskalen von Jahrzehnten bis Jahrhunderten und verwenden dazu drei Simulationen des vorindustriellen Millenniums, die mit dem Max Planck Institut Earth System Model (MPI-ESM) durchgeführt wurden. Es ist das Ziel dieser Arbeit, physikalische Erklärungen für die rekonstruierten Klimaphänomene in den vorindustriellen Jahrhunderten zu finden.

In einer ersten Studie untersuchen wir in den Simulationen extreme Kälteereignisse im westlichen subpolaren Nordatlantik von der Dauer einer Dekade oder mehr und vergleichen diese mit rekonstruierten Ereignissen aus der ersten Hälfte des vorindustriellen Jahrtausends. Wir interpretieren diese Ereignisse als Ausdruck interner Variabilität, die in der Region um Grönland einen besonders starken Ausdruck findet. Wir identifizieren einen Rückkopplungsmechanismus, der von einer abnehmenden SPG-Stärke und einer Reduktion der Tiefenwasserbildung in der Labradorsee gesteuert wird. Ausmaß und Dauer der simulierten Kälteperioden sind kompatibel mit den Klimabedingungen, die zum Niedergang der Besiedlung Südgrönlands durch norwegische Siedler beigetragen haben.

Im zweiten Abschnitt der Arbeit untersuchen wir eine abrupte und lang-anhaltende Abschwächung des SPG in einer der Simulationen. Diese sprunghafte Änderung ähnelt dem in Rekonstruktionen evidenten Übergang von einem relativ starken SPG während der MCA zu einem anhaltend schwächeren SPG in der LIA. In der Simulation initiiert der Übergang zu einem relativ schwachen SPG langanhaltende Anomalien im nordatlantischen Klima, die durch Wechselwirkungen zwischen atmosphärischer und ozeanischer Zirkulation, Meereisausdehnung und Salzgehaltsänderungen in der Labradorsee bestimmt werden. Änderungen in der AMOC oder der NAO spielen dagegen keine wesentliche Rolle. Initiiert wird die Abschwächung des SPG am Ende des 17. Jh durch verstärkten Süßwasserausstrom aus der Arktis in die Labradorsee. Dieser intensivierte Ausstrom kann durch die erhöhte Vulkantätigkeit am Ende des 17. Jh begünstigt worden sein. Sensitivitätsexperimente ohne vulkanischen Antrieb zeigen jedoch, dass dies keine notwendige Bedingung darstellt.

Abschließend untersuchen wir im dritten Teil der Arbeit wie sich die Abschwächung des SPG und die damit verbundene Verringerung des nordwärtigen Wärmetransportes auf das Klima im Nordmeer und auf den angrenzenden Kontinent auswirkt. Dabei finden wir neben regionalen auch saisonale Unterschiede. Im Winter führt die reduzierte Wärmezufuhr vor allem in der Barents See zu deutlichen Änderungen in den Wärmeflüssen zwischen Ozean und Atmosphäre. Diese erzeugen spezifische Luftdruckanomalien mit hohem Druck über Skandinavien wie sie für besonders kalte Winter in Europa typisch sind. Östliche Winde über dem Kontinent und Blocking Situationen über dem nordwestlichen Atlantik charakterisieren

auch in historischen Aufzeichnungen die Winter der LIA. Dagegen finden wir im Sommer einen geringeren Einfluss des Ozeans. Das europäische Klima, wie auch das der Nordhemisphäre, wird durch einen geringeren Strahlungsantrieb abgekühlt. Veränderliche ozeanische Wärmetransporte verstärken also die Klimaanomalie der LIA im Winter. Sensitivitätsexperimente, in denen wir die Zusammensetzung des externen Antriebes verändern, zeigen, dass Änderungen in der Sonnenintensität allein die LIA nicht erklären können. Die anhaltend geringe Strahlungsintensivität während des Maunder Minimums kann allerdings ein bedeutender Faktor gewesen sein, den kalten Zustand bis in das 18. Jh. zu erhalten.

Zusammenfassend untermauert diese Arbeit die besondere Rolle des Subpolarwirbels für die Klimaentwicklung im nordatlantischen/europäischen Raum. Im Gegensatz dazu finden wir in den Simulationen keine Anzeichen, dass Änderungen der AMOC oder der NAO den Übergang von der MCA zur LIA gesteuert haben.

List of Acronyms

AMOC	Atlantic Meridional Overturning Circulation
CE	Common Era
CMIP5	Coupled Model Intercomparison Project, Phase 5
DJF	December–February (winter season)
EDSST(S)	Eirik Drift sea surface temperature (or salinity)
EMT	European mean temperature
EOF	empirical orthogonal function
FWTR	freshwater transport
HTTR	heat transport
ISR	Iceland–Scotland Ridge
JJA	June–August (summer season)
LIA	Little Ice Age
LUT04	Luterbacher et al. (2004)
MCA	Medieval Climate Anomaly
MLD	mixed layer depth
MOI	meridional overturning index
MPI-ESM-P	Max Plank Institute Earth System Model for paleo-applications
NAO	North Atlantic Oscillation
NH	Northern Hemisphere
PC	principal component
PMIP3	Paleoclimate Modeling Intercomparison Project, Phase 3
SAT	near-surface (10 m) air temperature
SLP	sea level pressure
SPG	subpolar gyre
SSS	sea surface salinity
SST	sea surface temperature
stdv	standard deviation
Sv	Sverdrup (10^6 m^3/s)
TSI	total solar irradiance

Chapter 1

Introduction

Changes in Earth's climate can occur on a wide range of time scales, from months to thousands or millions of years. To investigate, understand, and even predict such changes, we need to measure climate and meteorological conditions over time. However, although some instrumental records cover some centuries in the past [e.g., Parker et al., 1992], they are generally restricted to local conditions over land areas. Direct observations on hemispheric or global scales are in turn only available since the late 19th century (for example, the HadISST data set), and they are therefore not long enough for full assessment of climate variability on time scales longer than a few decades. Such climate observations, in addition, show noticeable trends in the last century due to anthropogenic climate change that complicate their use for research on natural climate phenomena. Because of these limitations, we need to look farther back in climate history in order to investigate relatively long, natural climate changes.

This thesis in particular focuses on the climate of the pre-industrial past millennium, from medieval times to the onset of the Industrial Revolution (hereafter the period 850–1849 CE). The pre-industrial past millennium is specially important because it is the immediate period that precedes current instrumental records, and thus provides a longer background to understand the magnitude and nature of present or future variations of the current climate [e.g., Jungclaus et al., 2014; Rahmstorf et al., 2015]. Yet, evidence of the past millennium climate evolution relies on reconstructions based on climate proxies, which are but indirect sources of climate information, such as tree rings, documentary sources, or sediment and ice cores. Considerable efforts have been made in the last few years to reconstruct climate variables, like near-surface temperature, with relatively high—annual or even seasonal—temporal resolution on continental and hemispheric spatial scales [e.g., Pages 2k Consortium, 2013; Luterbacher et al., 2016]. Similar reconstructions for ocean-related variables are, in contrast, still difficult to obtain, and they commonly present lower temporal resolution than their analogues on land, and/or cover shorter periods [e.g., Cunningham et al., 2013; McGregor et al., 2015; Tierney et al., 2015]. One focus area for such oceanic reconstructions is the North Atlantic/Arctic region, where the main climate components, that is, ocean, atmosphere, cryosphere, and land, are tightly coupled [e.g., Grossmann and Klotzbach, 2009]. Here, climate reconstructions generally provide rather local information about one single climate variable (for example, upper-ocean temperature) that is insufficient to fully understand the physical processes underlying the reconstructed variability. One way to overcome such drawback is to compare these climate reconstructions with paleo-simulations performed with numerical climate models, which provide detailed information about all simulated climatic variables and, hence, a physically consistent context to interpret proxy-based records. In this thesis we shall follow this approach: by merging information from climate model simulations and reconstructions, we investigate natural climate variability and its driving processes on decadal to multicentennial times scales over the past millennium in the North Atlantic, Arctic, and European regions. Within this spatio-temporal framework, we shall show that the North

Atlantic subpolar gyre (SPG) alone can consistently explain some of its most remarkable climate episodes.

1.1 Open questions relating the climate of the North Atlantic/Arctic region in the past millennium

Temperature reconstructions of the Northern Hemisphere (NH) depict two major intervals in the pre-industrial past millennium: the Medieval Climate Anomaly (MCA), characterized by relatively warm temperatures in the 10th through 12th centuries approximately, and the Little Ice Age (LIA), with cold temperatures persisting into the 15th to 19th centuries (Fig. 1.1). The transition between these two episodes is commonly attributed to external forcing factors that can alter the Earth's radiative balance, such as volcanic eruptions or a reduction in the solar activity, although the relative contribution of each forcing is still subject of debate. While early modeling studies suggested a central role of the solar activity minima in the development of the LIA cold conditions during the 13th to 18th centuries [e.g., Crowley, 2000; Swingedouw et al., 2012], later works gave more relevance to the increase in the volcanic activity throughout this period [e.g., Schurer et al., 2014; Atwood et al., 2015]. Other forcing factors, as for example, greenhouse gas concentrations [e.g., Atwood et al., 2015], land cover changes [e.g., Bauer et al., 2003], or Earth's orbit parameters [e.g., Kaufman et al., 2009], are thought to have contributed marginally to the LIA onset.

However, although there is relative good agreement between hemispheric reconstructions on the general picture, there exist important regional differences in the reconstructed timing, magnitude, and spatial extent of the MCA and LIA [e.g., Mann et al., 2009; Pages 2k Consortium, 2013]. For example, reconstructions of the European climate suggest an earlier LIA onset than those for North America or Asia [Pages 2k Consortium, 2013], and exhibit

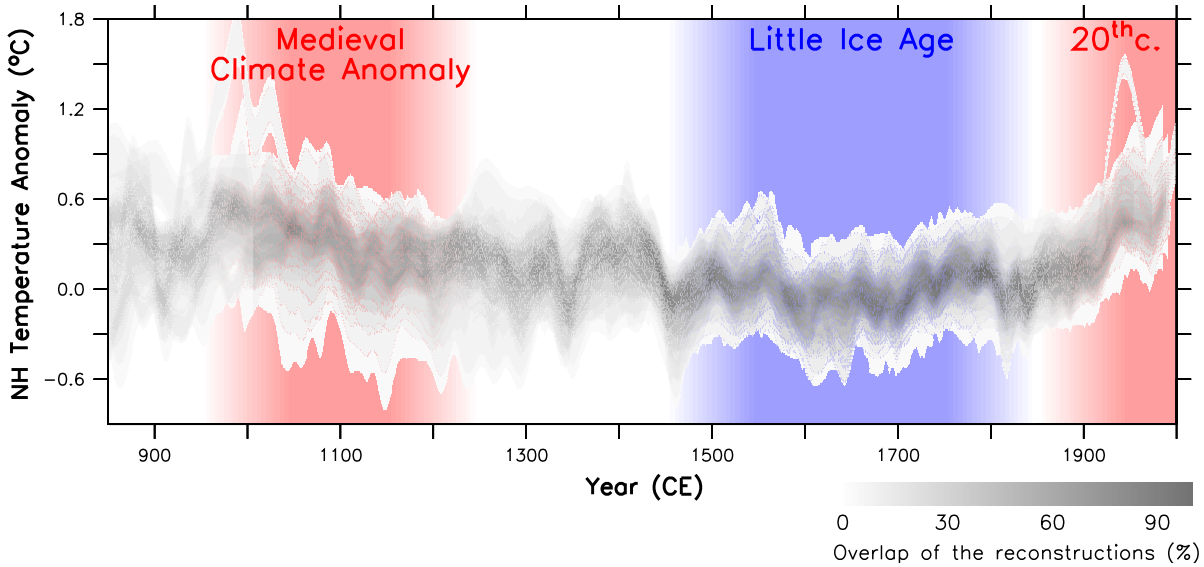

Figure 1.1: Reconstructed NH temperature (in °C), shown as anomalies with respect to the period 1500–1850 CE. Gray shading illustrates the overlap of available reconstructions (in percent), as in Masson-Delmotte et al. [2013].

discrepancies in the magnitude of the cooling between seasons [Luterbacher et al., 2004; Dobrovolnỳ et al., 2010]. Assuming that external forcings can trigger cascades of dynamical responses in climate modes of variability that persist over multidecadal to centennial time scales [e.g., Zhong et al., 2011; Zanchettin et al., 2012; Lehner et al., 2013], heterogeneity in past millennium reconstructions across different regions is nowadays interpreted as an expression of complex interactions between external forcing and internal climate dynamics and feedback mechanisms [e.g., Miller et al., 2012; Fernández-Donado et al., 2013; Lehner et al., 2013; Schleussner and Feulner, 2013]. In particular for the North Atlantic and Europe, simulated cold episodes similar to the LIA were explained as a result of reduced northward heat transport by the Atlantic meridional overturning circulation (AMOC) in both forced, transient [e.g., Miller et al., 2012; Lehner et al., 2013; Schleussner and Feulner, 2013] and unperturbed control experiments [Drijfhout et al., 2013]. Yet, these works disagree in both the main amplifying climate feedback and the external forcing responsible for such AMOC weakening. Attempts of reconstructing AMOC changes in the past millennium in turn suggest a reduction in some of its surface components during the LIA, like the Florida Current [Lund et al., 2006] or the North Atlantic Current [Wanamaker et al., 2012], but not in the AMOC as a whole [Rahmstorf et al., 2015]. Thus, the extent to which variations in the Atlantic Ocean circulation contributed to the LIA cooling in the North Atlantic is not fully understood yet.

Another theory to explain reconstructed climate changes in the North Atlantic and Europe in the past millennium related a shift in the North Atlantic Oscillation (NAO) from a more persistent positive phase during the MCA toward a more variable, yet mainly negative, phase during the LIA [Trouet et al., 2009], upon which an important amount of works has subsequently been built [e.g., Sicre et al., 2008; Patterson et al., 2010; Copard et al., 2012; Sicre et al., 2014; Young et al., 2015]. However, climate simulations first [e.g., Gómez-Navarro and Zorita, 2013; Lehner et al., 2012] and a newer NAO reconstruction later [Ortega et al., 2015] have put the NAO hypothesis into question. Given the lack of consensus in all previous studies, we will address the following question in this thesis:

What physical mechanisms allow explaining the main features of the cold conditions in the North Atlantic and Europe during the LIA?

An extensive compilation of paleoceanographic reconstructions from the North Atlantic/Arctic region can help shed light on the importance that variations of North Atlantic Ocean circulation could have had for the development of the LIA cooling. Records from this area, in fact, depict an abrupt transition from mostly warmer and saltier upper-ocean conditions during the MCA to colder and fresher ones, with expanded sea ice limits around Iceland and southern Greenland, during the LIA [Sicre et al., 2008; Massé et al., 2008; Moffa-Sánchez et al., 2014b, among others]. These climate changes were, again, primarily attributed to an AMOC slowdown and/or a NAO shift at the onset of the LIA; however, recent evidence suggests that the SPG could have modulated this transition in the North Atlantic/Arctic climate [e.g., Miettinen et al., 2012; Moffa-Sánchez et al., 2014b], as it seems to coincide with a reconstructed shift between a strong and a weak SPG circulation regime during the MCA and LIA respectively [Copard et al., 2012]. Whether and how all these climate changes were interrelated are still open questions, as well as the extent to which they can explain the onset of the LIA. Hence, we will also tackle the following question in this thesis:

What relative role did the reconstructed changes in the SPG play in driving the North Atlantic and European cooling during the LIA, with respect to those in the AMOC or NAO?

Embedded in a multicentennial cooling trend from the MCA to the LIA, reconstructions of the surface temperature also show decadal to multidecadal cold episodes in the subpolar North Atlantic [e.g., Sicre et al., 2011; Moffa-Sánchez et al., 2014a]. The importance of these events lies in the fact that they seem to have occurred before the demise of the North settlements in Greenland in the 14th and 15th centuries and, hence, might have contributed to it. Nevertheless, the exact mechanism underlying these events cannot be fully understood from single climate reconstructions, and the variety of explanations proposed so far have invoked both hemispheric-scale NAO shift and AMOC weakening at the onset of the LIA, as well as both volcanic eruptions and solar minima [e.g., Patterson et al., 2010; Sicre et al., 2011; Kuijpers et al., 2014; Moffa-Sánchez et al., 2014a]. We will therefore pose the following question in this thesis as well:

Is the physical mechanism that allows explaining decadal cold events in the North Atlantic related to any global or hemispheric phenomenon triggered by a particular external forcing?

1.2 Oceanographic and atmospheric setting

This thesis focuses on dynamics and processes relating the climate in the North Atlantic/Arctic region (Fig. 1.2). Here, the SPG is an important component of the large-scale surface circulation of the North Atlantic Ocean (Fig. 1.3). It presents a cyclonic circulation that comprises the North Atlantic Current, the Irminger Current, the East and West Greenland currents, and the Labrador Current, and that is surrounded by the Labrador Peninsula, Greenland, Iceland, the Faeroe Islands, and Scotland, between approximately 50°N and 65°N. The North Atlantic Current continues the path of the Gulf Stream north-northeastward, transporting relatively warm and salty tropical waters into the eastern subpolar basin. Here, such waters continue via two main flows: either over the Iceland–Scotland Ridge along the Norwegian Current northward, into the Nordic Seas first, and the Barents Seas later, already in the Arctic Ocean; or, through the Irminger and both Greenland currents westward into the

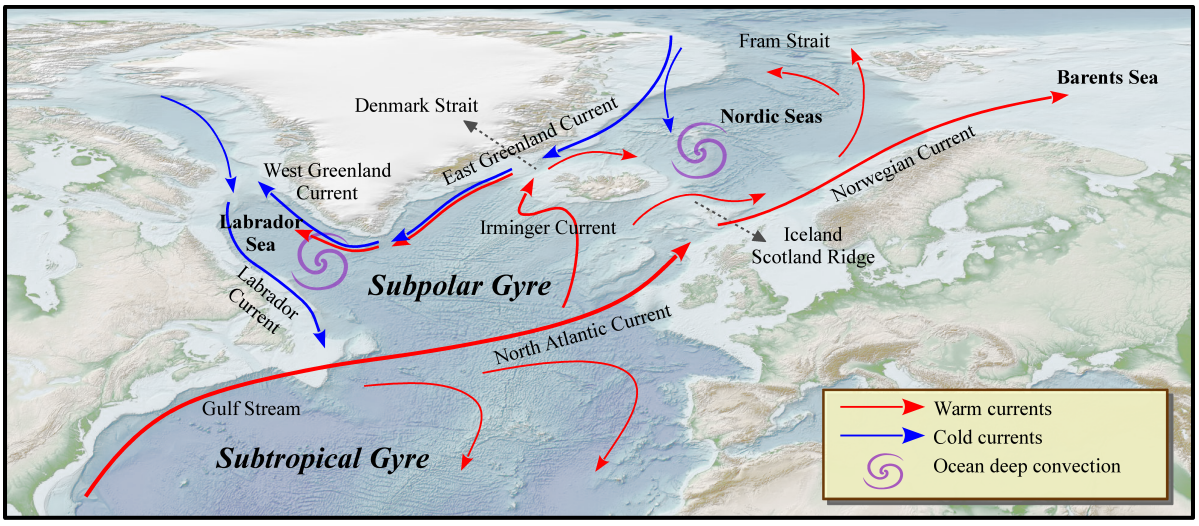

Figure 1.2: Study area, between the North Atlantic and Arctic oceans. Blue/red arrows indicate cold/warm currents, and spirals regions of deep water formation.

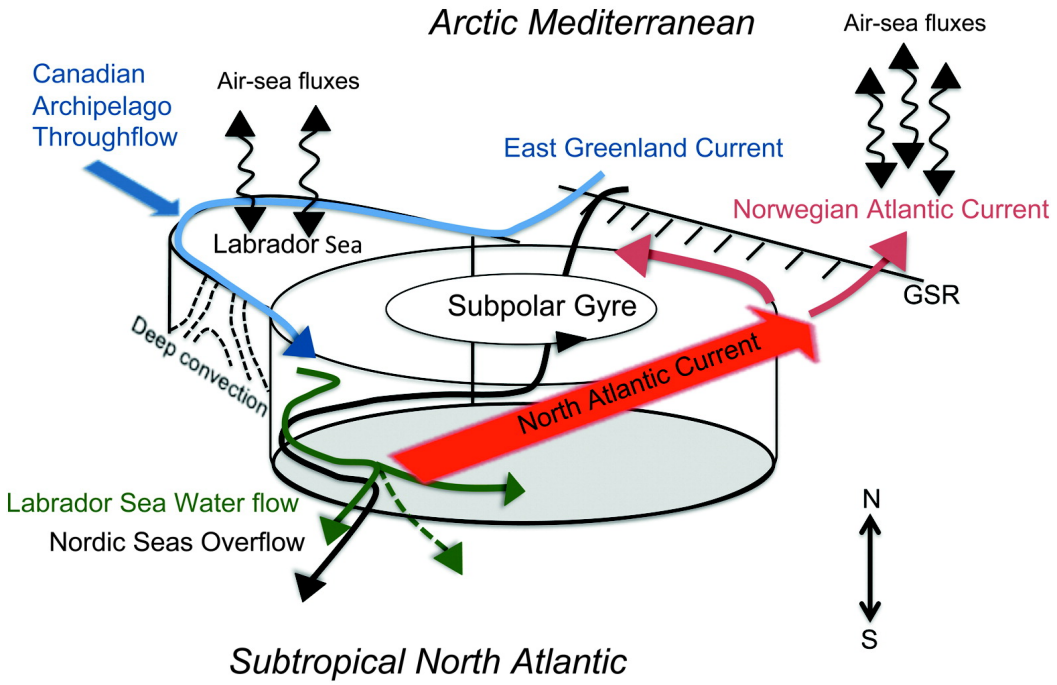

Figure 1.3: Schematic view of the main circulation in the subpolar North Atlantic. Arctic Mediterranean refers to the area comprising the Nordic and Barents seas in Fig. 1.2. GSR is for Greenland–Scotland Ridge (i.e., the Denmark Strait and the Iceland–Scotland Ridge). From Langehaug et al. [2012]. © American Meteorological Society. Used with permission.

Labrador Sea. Along both paths surface waters release heat (wavy vertical arrows in Fig 1.3) to the overlying atmosphere, where it is further transported westward and contributes to moderating winter temperatures of Western Europe and Scandinavia [Seager et al., 2002]. Additionally, buoyancy loss associated with such heat release leads to the formation of deep and intermediate waters most notably in the Labrador and Nordic seas (spirals in Fig. 1.2; also Fig. 1.3). Deep waters formed in the Nordic Seas flow back over the Iceland–Scotland Ridge and the Denmark Strait to join those from the Labrador Sea basin, moving altogether as the Deep Western Boundary Current southward out of the subpolar North Atlantic (Fig. 1.3). In order to compensate for the water inflow into the Nordic Seas and Arctic Ocean, the East Greenland Current flows southward along the eastern coast of Greenland, from the Fram Strait to southern Greenland through the Nordic Seas and the Denmark Strait. This current transports relatively cold and fresh polar waters into the subpolar basin and, more importantly, about 90% of the ice exported from the Arctic Ocean. The subpolar North Atlantic thus witnesses the confluence of tropical and polar waters within its basin. These characteristics render the SPG crucial, first, for heat and salt exchanges between the North Atlantic and the Arctic, second, for the formation of deep waters that eventually shape the AMOC, and last but not least, for tempering European climate.

Surface atmospheric circulation over the North Atlantic/Arctic region is primarily dominated by two main "center of actions": the Azores high-pressure system, a semi-permanent subtropical anticyclone that in summer can cover nearly all the North Atlantic; and the Icelandic Low, located mostly off the southern coast of Greenland in winter as part of a broad area of low pressure extending into the Barents and Kara seas. Due to the

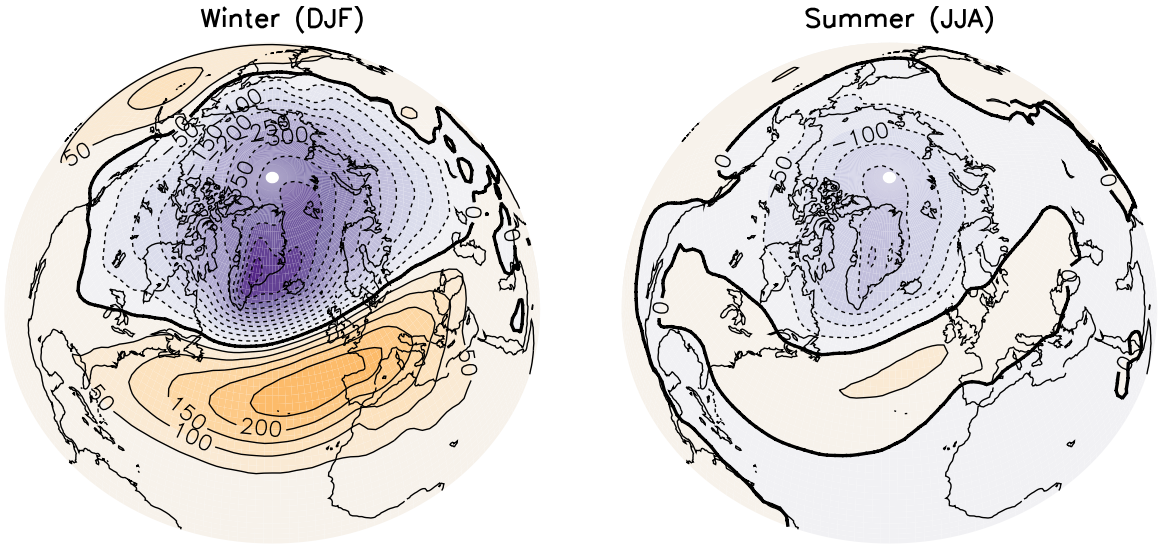

Figure 1.4: NAO in winter (December–February, DJF; left) and summer (June–August, JJA; right) simulated in PiControl (see Chapter 2 for further details) and calculated as described in Section 3.1. Patterns shown here (in Pa) are obtained by regressing the hemispheric sea-level pressure (SLP) anomalies onto the time series of the leading principal component.

pressure gradient between these two systems, surface westerlies prevail across middle latitudes of the North Atlantic all year round, not only bringing moist-rich and relatively warm air masses into the European continent, but also contributing to driving the oceanic surface circulation below. The NAO is the most prominent mode of atmospheric variability in this region and, although it can be identified any time of the year, it is best expressed in winter (Fig. 1.4). The NAO describes co-variability in pressure variations between the Icelandic Low and the Azores High, so that when both systems are strong, the NAO is in its positive mode, and vice versa. Swings between NAO phases therefore lead to important variations in the wind speed and direction over the Atlantic, as well as in the transport of heat and moisture between the Atlantic and the surrounding continents, and the intensity, number, and path of the storms that reach the European continent [e.g., Hurrell et al., 2001]. In addition to this, NAO variations can drive anomalous patterns of upper-ocean temperatures and sea ice cover in the North Atlantic and Arctic Ocean, and influence oceanic deep convection in the Labrador and Nordic seas and, by extension, the North Atlantic Ocean circulation and its related heat transport [Eden and Willebrand, 2001; Marshall et al., 2001; Visbeck et al., 2003].

1.3 Thesis outline

Chapters 4, 5, and 6 of this thesis are written in the style of scientific journal publications: they contain their own Introduction and Conclusions, and can be read largely independently of one another. Chapters 4 and 5 are published in *Geophysical Research Letter*[1] and *Climate*

[1]Moreno-Chamarro, E., Zanchettin, D., Lohmann, K., and Jungclaus, J. H. (2015). Internally generated decadal cold events in the northern North Atlantic and their possible implications for the demise of the Norse settlements in Greenland. *Geophysical Research Letters*, 42(3):908–915.

Dynamics[2] respectively, and are reproduced here with editorial adjustments. Finally, Chapter 6 is currently being prepared for submission. The structure of this thesis follows the order in which research was conducted, rather than the one given by the research questions posed above. This has the benefit that it allows us to describe climate dynamics from shorter (decadal to multicedacal) to longer (centennial to multicentennial) time scales in the North Atlantic/Arctic region. This thesis is thus structured:

- Chapter 2 describes the model and simulations used in this thesis.
- Chapter 3 defines climatic indices that are extensively used throughout this thesis, and details the methodology followed to calculate statistical significance of the identified climate signals.
- Chapter 4 investigates the dynamics of decadal cold events in the subpolar North Atlantic that could have contributed to the failure of the Norse colonies in Greenland; this Chapter therefore aims to answer the third question raised before.
- Chapter 5 studies an abrupt transition in the SPG toward a multicentennial LIA-type cold state in the North Atlantic, as well as the potential role of the volcanic forcing and background climate conditions in its onset; this Chapter will therefore help answer the first and second questions raised before.
- Chapter 6 explores to what extent a reduction in the SPG-related northward heat transport into the Nordic Seas and associated atmospheric circulation change can lead to a regional amplification of the cold conditions during the LIA over Europe in winter, with respect to summer; this Chapter will hence help answer the first and second questions raised before.
- Chapter 7 closes this thesis summarizing the major conclusions and open questions for future research.

[2]Moreno-Chamarro, E., Zanchettin, D., Lohmann, K., and Jungclaus, J. H. (2016). An abrupt weakening of the subpolar gyre as trigger of Little Ice Age-type episodes. *Climate Dynamics*, pages 1–18.

Chapter 2

Model and experimental setup

This thesis uses simulations performed with the Max Plank Institute Earth System Model for paleo-applications (MPI-ESM-P). The atmosphere general circulation model ECHAM6 [Stevens et al., 2013] is run at a horizontal resolution of spectral truncation T63 (1.875°), with 47 vertical levels that resolve the stratosphere up to 0.01 hPa. The ocean/sea-ice model MPIOM [Marsland et al., 2003; Jungclaus et al., 2013] has a conformal mapping horizontal grid of nominal 1.5° resolution and grid poles over Antarctica and southern Greenland. The convergence of the mesh size toward the poles translates into a grid spacing of 15 to 100 km in the North Atlantic and, thereby, provides a relatively high resolution in the regions of interest for this thesis, namely the northern North Atlantic (Fig. 1.2). Vertically, MPIOM applies 40 unevenly spaced z levels, with the first 20 covering the upper 700 m of the water column.

We use an ensemble of three full-forcing transient simulations of the last millennium, between 850 CE and 1849 CE (hereafter Past1000-R1, R2, and R3). These follow the protocol of the Paleoclimate Modeling Intercomparison Project, Phase 3 (PMIP3) [Schmidt et al., 2011; Braconnot et al., 2012] within the Coupled Model Intercomparison Project, Phase 5 (CMIP5). Prescribed external forcing factors are as follows (Fig. 2.1):

- Volcanic aerosol optical depth at 550 nm and effective radius from Crowley and Unterman [2013].

- Total solar irradiance (TSI), as reconstructed in Vieira et al. [2011], and from the data set for the period 1850–2005 CE given by Wang et al. [2005], with an artificial 11-year cycle of varying amplitude imposed over the pre-industrial period. A linear interpolation is applied to compute monthly TSI averages from reconstructed annual values between 850 CE and 1849 CE scaled to Total Irradiance Monitor data, except for the flux at 180.5 nm. Spectral Solar Irradiance for the 14 short-wave spectral bands of the ECHAM6's radiation scheme is calculated in a way that the sum of the Spectral Solar Irradiance yields TSI. Energy in the part of the spectrum below the shortest wavelength of the radiation scheme (200 nm) and above the longest (12195.1 nm) is added to the first and last bands respectively. In turn, monthly average ozone concentrations between 850 CE and 1849 CE are calculated from the 1850–1860 CE monthly climatology of ozone concentrations from the AC&C/SPARC Ozone Database as a basis, thus representing the ozone dependency on solar irradiance through regression coefficients between historical ozone concentrations and the annual 180.5 nm solar flux.

- Atmospheric concentrations of the most important well-mixed greenhouse gases and anthropogenic aerosols as indicated in Schmidt et al. [2011].

- Changes in global land-cover and agricultural areas from Pongratz et al. [2008].

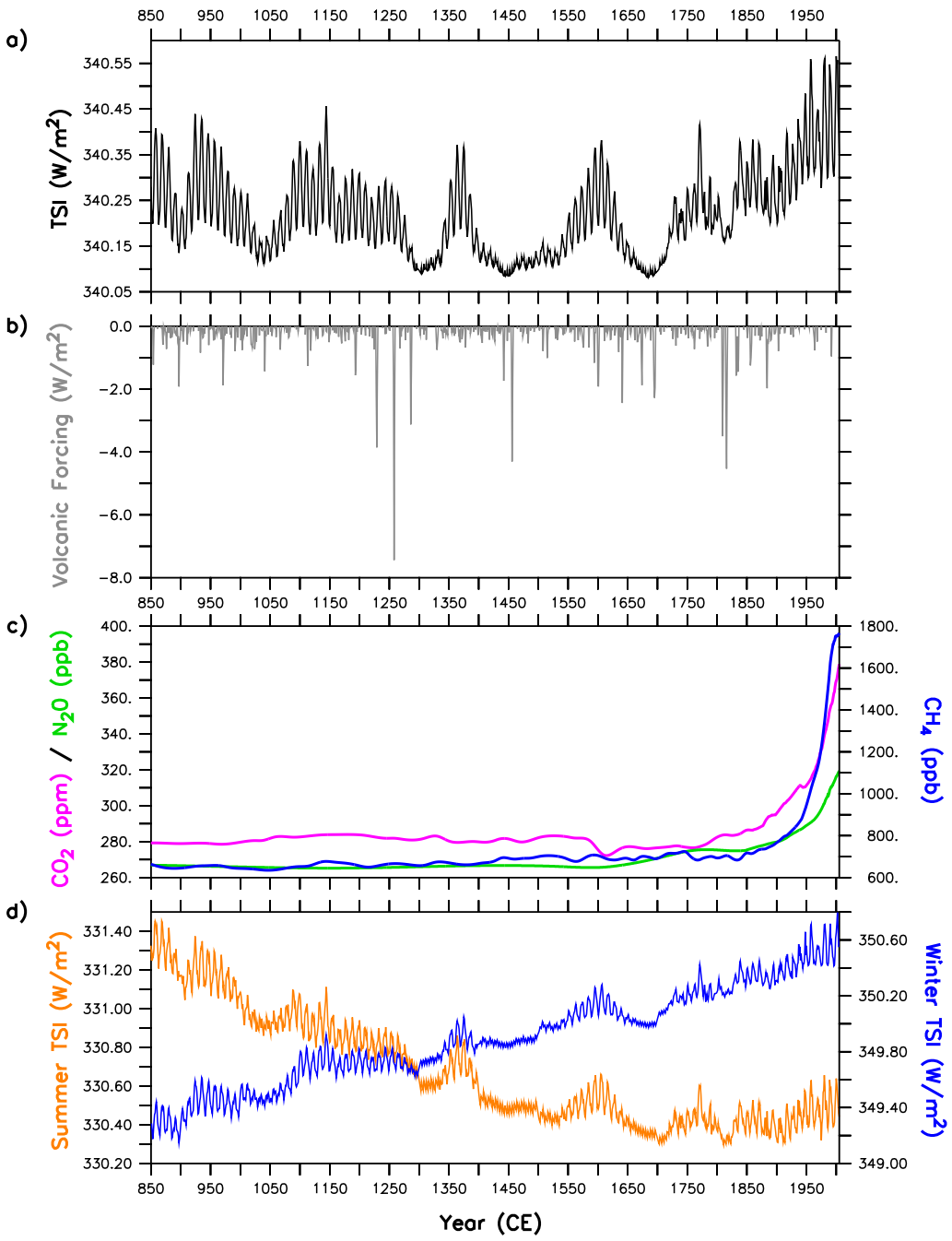

Figure 2.1: Prescribed forcings in the Past1000 ensemble between 850 CE and 2005 CE, here shown for Past1000-R2. Annual globally averaged values of the **(a)** reconstructed TSI (in W/m^2) and **(b)** simulated volcanic forcing, the latter shown as net radiative flux anomalies (long plus short waves, in W/m^2) at the top of the atmosphere with respect to the climatological mean. Timing of the volcanic eruptions is the same in all Past1000s as they all apply the reconstructed aerosol properties by Crowley and Unterman [2013], although the implementation of the forcing slightly differs among the simulations. **(c)** Well-mixed greenhouse gas concentration changes. **(d)** Changes in the Earth's orbit parameters, here shown through the seasonal trends in the globally averaged TSI in summer (JJA) and winter (DJF). For a more detailed description of the forcings, see text.

- Annual values for the Earth's orbital parameters, that is, eccentricity, obliquity, and perihelion.

We also use an 1156-year-long control simulation under constant pre-industrial (1850 CE) boundary conditions (hereafter PiControl) as a reference for the forced runs. The integration of the Past1000s is initiated after a 400-year-long spin-up with constant 850 CE boundary conditions, itself initiated from the last integration year of PiControl. Past1000-R1 and R2 are initialized with the same ocean state, but differ in the standard deviation on the assumed log-normal distribution of the volcanic aerosol size (1.2 μm in R1, 1.8 μm in R2 and R3). Past1000-R2 and R3, in turn, use the same parameter setting for the volcanic forcing, but are initiated from different initial conditions. Besides, ozone concentration data used in Past1000-R1 are affected by an 1-month-shift in the annual cycle from the AC&C/SPARC ozone climatology, an issue solved in Past1000-R2 and R3. Although the PMIP3 protocol defines the Past1000 integration period between 850 CE and 1849 CE, the Past1000 ensemble continues over the historical period (1850–2005 CE), following the CMIP5 protocol. Nonetheless, and to avoid possible spurious effects due to anthropogenic influences, this thesis mostly focused on the pre-industrial past millennium. The historical period is only considered in Chapter 6 for comparison with reconstructed temperatures over Europe.

Chapter 3

Methods

3.1 Indices

We define in the following some indices describing prominent patterns of large-scale climate variability that are used repeatedly in this thesis:

- Because of the vertical structure of the mean currents in the northern North Atlantic, the circulation of the SPG is well described by the barotropic streamfunction, itself derived from vertically integrated currents. We therefore define an index for the **strength of the SPG** as the absolute value of the barotropic streamfunction spatially averaged between 50°N–65°N and 10°W–60°W.

- The variability of the AMOC strength can be characterized by the **meridional overturning index (MOI)** [Delworth et al., 1993]. This is defined as the average of the zonally integrated overturning streamfunction in the North Atlantic between 35°N and 45°N at 1000 m depth, i.e., where the climatological maximum of the simulated AMOC is located in PiControl (see, for example, Fig. 4.2g).

- The **NAO** is defined as the first Principal Component of the SLP anomalies in the North Atlantic sector, between 20°N–90°N and 80°W–40°E. The NAO is calculated for both the winter (DJF) and summer (JJA) seasons (Fig. 1.4), when it explains about 55% and 45% of the total variance respectively.

Units of volume transport are in Sverdrup (Sv; 1 Sv = 10^6 m^3/s). Thus, for example, values for the simulated MOI and SPG strength in PiControl are ∼21 Sv and ∼13 Sv respectively.

3.2 Statistical significance

Statistical significance is most of the times estimated from the likelihood of a random occurrence of the signal in PiControl, so that we determine how likely it is that the signal can be attributed to internal climate variability alone. Thus, a signal detected in any of the Past1000s is compared to analog signals obtained by randomly sampling it 500 times in the full length of PiControl. Percentile intervals (commonly 5th–95th or 1st–99th) of the empirical anomaly distribution obtained from the randomization are subsequently used to determine the confidence levels associated with a random occurrence of the signal.

If this method is not applied, for example because of the lack of a suitable control simulation, statistical significance is calculated based on a two-sided *t* test [Von Storch and Zwiers, 2001], in which effective degrees of freedom are taken into account [Von Storch and Zwiers, 2001].

Chapter 4

Internally generated decadal cold events in the northern North Atlantic and their possible implications for the demise of the Norse settlements in Greenland

We attribute and describe the governing mechanism of decadal cold excursions in the subpolar North Atlantic, which are detected in an ensemble of three transient and one unperturbed climate simulation, and whose amplitude and duration are similar to those of cold events reconstructed in the last millennium. The simulated events are attributed to internal regional climate variability, with varying external forcing increasing their magnitude and frequency. The underlying general mechanism consists of a feedback loop initiated by a weakening of the North Atlantic SPG, which induces persistent colder and fresher surface conditions in the Labrador Sea and, eventually, a deep convection shutdown. We thus exclude hemispheric climate reorganization or weak ocean overturning circulation as necessary trigger for such events. An associated northeastward atmospheric cold advection over the Labrador Sea deteriorates local living conditions on south Greenland, essential for the sustainability of the Norse settlements.

4.1 Introduction

The Norse expansion to Iceland, Greenland, and, eventually, North America was likely favored by the mild NH climate conditions by the beginning of the last millennium during the MCA (Fig. 1.1) [Ogilvie et al., 2000; Kuijpers et al., 2014]. The loss of their Greenland settlements some centuries later, in contrast, roughly coincides with the onset of the LIA [Ogilvie et al., 2000; Kuijpers et al., 2014], the anomalously cold period between the 14th and 19th centuries (Fig. 1.1). Worsening in the local living conditions associated with a colder NH climate might thus have contributed, in combination with other factors, to this demise [Dugmore et al., 2012]. Since relevant aspects of such local environmental change remain unclear, this Chapter aims at investigating whether it was necessarily caused by external forcing, as well as whether regional, rather than global processes, were determinant.

Climate variability over southern Greenland is largely influenced by that of the northern North Atlantic sector [e.g., Kuijpers et al., 2014], which is in turn shaped by different modes of atmospheric and oceanic variability, such as the NAO or the AMOC [e.g., Marshall et al., 2001; Grossmann and Klotzbach, 2009]. Over the last years attention has focused on better understanding the dynamics of the surface circulation in the subpolar North Atlantic, namely the SPG (Fig. 1.2) [e.g., Langehaug et al., 2012; Born and Stocker, 2014]. This basin-wide cyclonic oceanic gyre is primarily driven by wind forcing and buoyancy differences within the subpolar North Atlantic between 50°N and 65°N [e.g., Marshall et al., 2001], and transports, on the one hand, relatively warm and saline tropical water northward, and on the other, cold and fresh polar water southward along its eastern and western rims respectively (Fig. 1.2). Furthermore, the SPG is an important component of the thermohaline circulation [Hátún et al., 2005], since variations in the gyre's strength modulate the transport of salt to the Labrador and Nordic seas, that is, to regions where oceanic deep water formation takes places. The SPG has thus been described as one relevant driver of the North Atlantic climate variability on different time scales [e.g., Moffa-Sánchez et al., 2014a; Jungclaus et al., 2014].

Climate reconstructions along the coasts of Iceland and southern Greenland show prominent interdecadal cold events before the demise of the Norse settlements in the 14th and 15th centuries [e.g., Patterson et al., 2010; Moffa-Sánchez et al., 2014b]. Such events have been associated with increased transport of cold and ice-rich polar waters by the East Greenland Current from the Arctic Ocean to the subpolar North Atlantic [e.g., Ran et al., 2011; Moffa-Sánchez et al., 2014b], as well as with weaker advection of warm, tropical waters by the SPG [Moffa-Sánchez et al., 2014a]. Hence, intrusion of relatively fresh waters into the Labrador Sea could also have contributed to reducing deep water formation and, by extension, to weakening the AMOC and its associated meridional heat transport (HTTR) [e.g., Miller et al., 2012]. Other works, in addition, have linked these changes to long-term fluctuations in large-scale atmospheric circulation, like those described by the NAO [see Patterson et al., 2010; Kuijpers et al., 2014] or by atmospheric blocking situations [Moffa-Sánchez et al., 2014a].

Nonetheless, it is still uncertain whether reconstructed cold events occurred as an externally forced response, that is, as consequence of variations of the Earths energy budget driven by external agents (e.g., volcanic eruptions), or due to internal climate variability, that is, from spontaneous dynamics and feedbacks within the climate system [e.g., Hasselmann, 1976]. Similar timing was found between proxy-based temperature reconstructions and the frequency and magnitude of solar minima [Ran et al., 2011; Moffa-Sánchez et al., 2014a] and a cluster of explosive volcanic eruptions [Sicre et al., 2011; Miller et al., 2012]. Last millennium

climate simulations supported both the solar [e.g., Jiang et al., 2005; Moffa-Sánchez et al., 2014a] and the volcanic hypotheses [e.g., Sicre et al., 2011]. However, cold excursions in the paleo-record also occurred during periods characterized by weak external forcing [e.g., Sicre et al., 2011], pointing to a non-negligible role of internal climate variability.

Accordingly, a realistic shift from a warm to a cold period over the Norse Greenland settlements spontaneously emerged in a multi-millennial unperturbed control climate simulation [Hunt, 2009]. The onset and persistence of such a cold regime was thus attributed to stochastic influences, excluding large-scale modes of atmospheric variability, like the NAO, as possible drivers [Hunt, 2009].

In view of these partly contradictory results, and in order to complement contributions from previous studies, we investigate in this Chapter the dynamics underlying decadal-scale cold events in the northern North Atlantic in the Past1000 ensemble and PiControl (see Chapter 2 for further details). We thus aim to answer the following questions: What mechanism is behind these cold events? And, is this similar for all cold events considered? Are such events triggered only by external forcing? Or are they part of the internal climate variability? Are these events necessarily linked to large-scale phenomena or hemispheric/global climate variability?

4.2 Methods

Proxy-based reconstructions of changes in seawater properties over the Eirik Drift have been recently used to investigate the northern North Atlantic climate variability during the last millennium [Moffa-Sánchez et al., 2014b, H. F. Kleiven et al., personal communication, 2014]. This location, at about 60°N and 55°W off south Greenland, is well situated to monitor and estimate surface and subsurface variations in both the East Greenland and Irminger currents, which constitute the northern rim of the SPG (Fig. 1.2).

Decadal-scale cold periods in the northern North Atlantic are detected based on smoothed (11-year running mean) annual sea surface temperature (SST) anomalies at the Eirik Drift site (EDSST hereafter), averaged between 55°N–60°N and 40°W–50°W (black box in Fig. 4.2a). These anomalies are calculated for each simulation with respect to the PiControl climatological mean, which provides estimates of the simulated internal climate variability. To focus on decadal-scale events, we only consider periods with sustained EDSST anomalies below –1.1°C during five or more consecutive years. This threshold value (Fig. 4.2b,c, horizontal gray dash-dotted lines) corresponds to the 5th percentile of the distribution of the combined Past1000's EDSST anomalies. This criterion therefore incorporates information about both the relative frequency and magnitude of clustered cold years, without further discrimination between these two contributions. Our results for the detected cold events do not appreciably change if a different criterion is applied (e.g., with respect to the distribution of EDSST anomalies in PiControl). Besides, long-lasting cold events are expected to have had a more significant impact on the Norse society in Greenland [Dugmore et al., 2012]. Dynamical interpretation of the cold events is based on analysis of the associated composite of anomalies, these calculated with respect to the unperturbed climatology. The coldest year of each event (hereafter year 0) is used as reference for the compositing (Figs. 4.2 and 4.3).

We further compare the response of the North Atlantic climate during a cold event to that after a strong volcanic eruption. To do so, we define a composite containing seven of the strongest volcanic events in the past millennium (vertical bars in Fig. 4.1b), whose global radiative perturbation exceeds –1.5 W/m^2 at the top of the atmosphere in the three Past1000s, similarly as in Zanchettin et al. [2012]. Volcanically forced North Atlantic anomalies (Fig. 4.5)

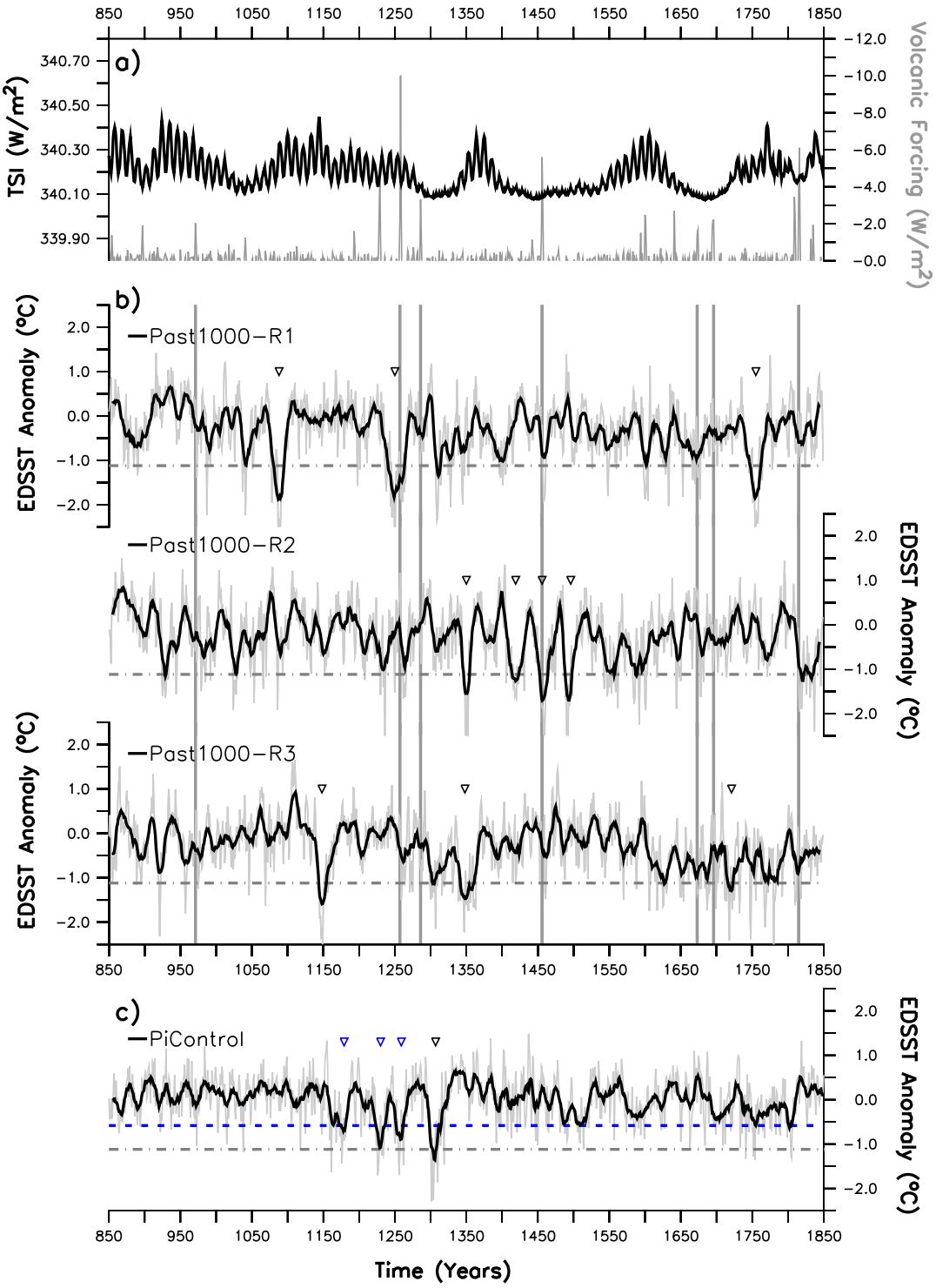

Figure 4.1: **(a)** Solar and volcanic forcings in Past1000-R1, as in Fig. 2.1. **(b–c)** Respectively, annual EDSST anomalies (in °C; gray lines) in the Past1000s and PiControl, calculated with respect to the PiControl climatological mean. Black lines are the corresponding 11-year running mean. Horizontal dash-dotted gray lines account for the –1.1 °C threshold, whereas the blue one accounts for the PiControl-only –0.58 °C threshold (see Sections 4.2 and 4.3). Gray/blue triangles outline cold events that satisfy the gray/blue criterion. Vertical lines in **(b)** are the ensemble of volcanic eruptions considered in Fig. 4.5.

remain substantially the same if different criteria are applied to select the volcanic events, like a selection of all eruptions with an associated radiative anomalies larger than –2W/m^2, for example. We refer the reader to Zanchettin et al. [2012] for a detailed description of the response of the North Atlantic to strong volcanic eruptions.

4.3 Results

We identify 10 cold events in the three Past1000s (gray triangles in 4.1b) according to our criterion. These show negative EDSST anomalies lasting for about 20 to 40 years, with the coldest anomalies ranging between –1.5°C and –2°C. Simulated cold events are thus of similar amplitude and duration to those reconstructed within the northern North Atlantic during the last millennium [e.g., Sicre et al., 2011; Moffa-Sánchez et al., 2014a]. Events appear scattered throughout the Past1000s, and events in different realizations do not robustly overlap in time. In addition, they develop both isolated in time (e.g., around 1090 in Past1000-R1) or in series of events (e.g., after 1400 in Past1000-R2). One cold event of similar characteristics, that is duration and amplitude, to those in the Past1000 ensemble is identified in PiControl (gray triangle in Fig. 4.1c). Other three events are also identified in PiControl if the criterion is instead based on a EDSST distribution from PiControl (blue triangles in Fig. 4.1c). This can be explained by the smaller standard deviation of the EDSST in PiControl (0.32 °C) compared to that in the Past1000s (0.46 °C, 0.48 °C, and 0.43 °C respectively in R1, R2, and R3), which most likely reflects the influence of the imposed external forcing on the North Atlantic mean climate state. EDSSTs are, however, not robustly lag-correlated with the TSI or the volcanic forcing in any of the Past1000s (forcings shown in Fig. 4.1a, and cross-correlation profiles in Fig. 4.4). Furthermore, cold events in the Past1000s are generally found outside periods characterized by anomalous external forcing, such as solar minima (Fig. 4.1a) or major volcanic eruptions (Fig. 4.1a, and vertical bars in Fig. 4.1b). Only few cold events occur after major volcanic eruptions, and the response of the EDSSTs is never robust across the three simulations: thus, for example, the 1228 CE-eruption is associated with a strong cold excursion in Past1000-R1, albeit with a slight warming in Past1000-R3. The North Atlantic response to volcanic forcing (Fig. 4.5) in turn differs from the evolution around the cold events (see below). On the other hand, the slightly negative trend in the EDSST time series might partly be attributed to varying orbital parameters (Fig. 2.1d) [Kaufman et al., 2009]; nonetheless, the detected cold events do not cluster on either side of the Past1000s, and rather occur throughout the whole integration time, which suggests a negligible role of millennial-scale changes in the background state. Taken together, these results indicate that cold events in the subpolar North Atlantic can be triggered by internal climate variability alone. External forcing appears to be indirectly involved though a general amplification of EDSST variability under forced conditions, favoring the development deeper cold events more frequently, which might be related to a colder climate background state in the forced runs. Understanding the role of external forcing in the general climate state is, however, beyond the scope of this Chapter.

In the following, composite anomalies of the 10 cold events detected in the Past1000s (gray triangles in Fig. 4.1b) are shown in order to describe their underlying mechanism and imprint on the North Atlantic climate. Figure 4.2 illustrates the North Atlantic climate anomalies associated with this composite, while Figure 4.3 shows the temporal evolution around year-0 of composite standardized indices of climatic quantities. Cold events are characterized by a broad cooling of the subpolar North Atlantic surface (Fig. 4.2a), more intense to the west of the oceanic basin, and with the coldest anomalies in the Labrador Sea and along the southern

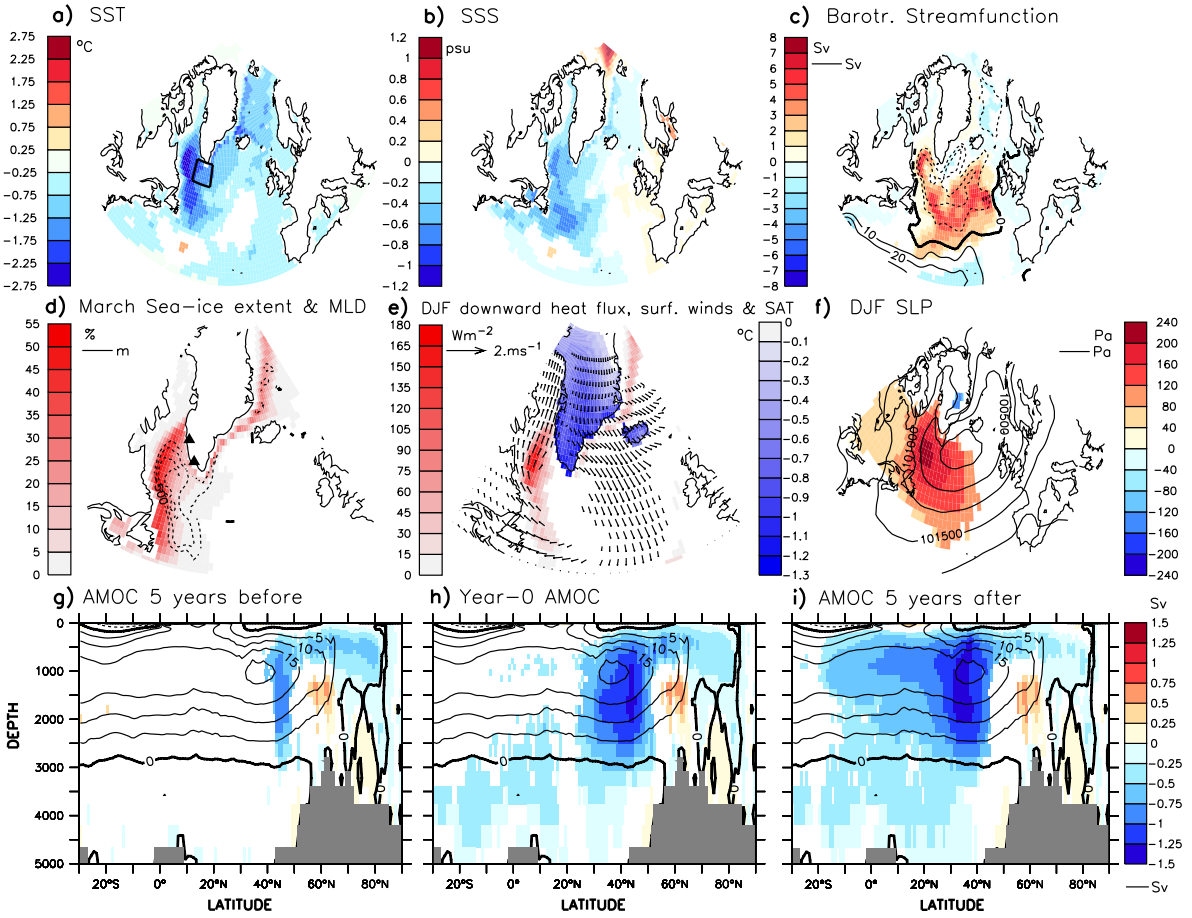

Figure 4.2: Anomalies for the composite of 10 cold events selected from the Past1000s (triangles in Fig. 4.1b): **(a)** SST (in °C); **(b)** SSS (in psu); **(c)** barotropic stream function (in Sv; shading), with contours representing the climatological mean in PiControl at 10 Sv intervals (dashed/solid lines correspond to cyclonic/anticyclonic flow); **(d)** ocean mixed layer depth (MLD, in m; in contours at 500 m intervals) and sea ice concentration (in percent of area; shading), both in March; **(e)** DJF surface heat flux into the atmosphere (in W/m^2; red shading), as well as yearly near-surface (~10 m) temperature (SAT) over Greenland (in °C; blue shading) and wind (in m/s; arrows); **(f)** DJF SLP (in Pa; shading) with contours representing the climatological mean in PiControl at 500 Pa intervals; AMOC (in Sv; shading) **(g)** 5 years before, **(h)** during, and **(i)** 5 years after the event's coldest year, with contours representing the climatological mean in PiControl at 5 Sv intervals. Anomalies are calculated with respect to the climatological mean of PiControl, after smoothing with an 11-year running mean. Only anomalies above the 99% confidence level are shown, based on the likelihood of occurrence of the signal in PiControl (see Chapter 3). Black box in **(a)** encloses the area within the Eirik Drift in which SST anomalies shown in Fig. 4.1 are averaged. Triangles in **(d)** indicate the locations of the former Norse settlements in Greenland [Ogilvie et al., 2000].

coast of Greenland. A similar pattern characterizes sea surface salinity (SSS) anomalies in this region (Fig. 4.2b), with a widespread surface freshening in the northwestern North Atlantic. The cooling and freshening of the upper northern North Atlantic becomes significant over the Eirik Drift about 11 years before the peak of the event (Fig. 4.3). More generally, simulated

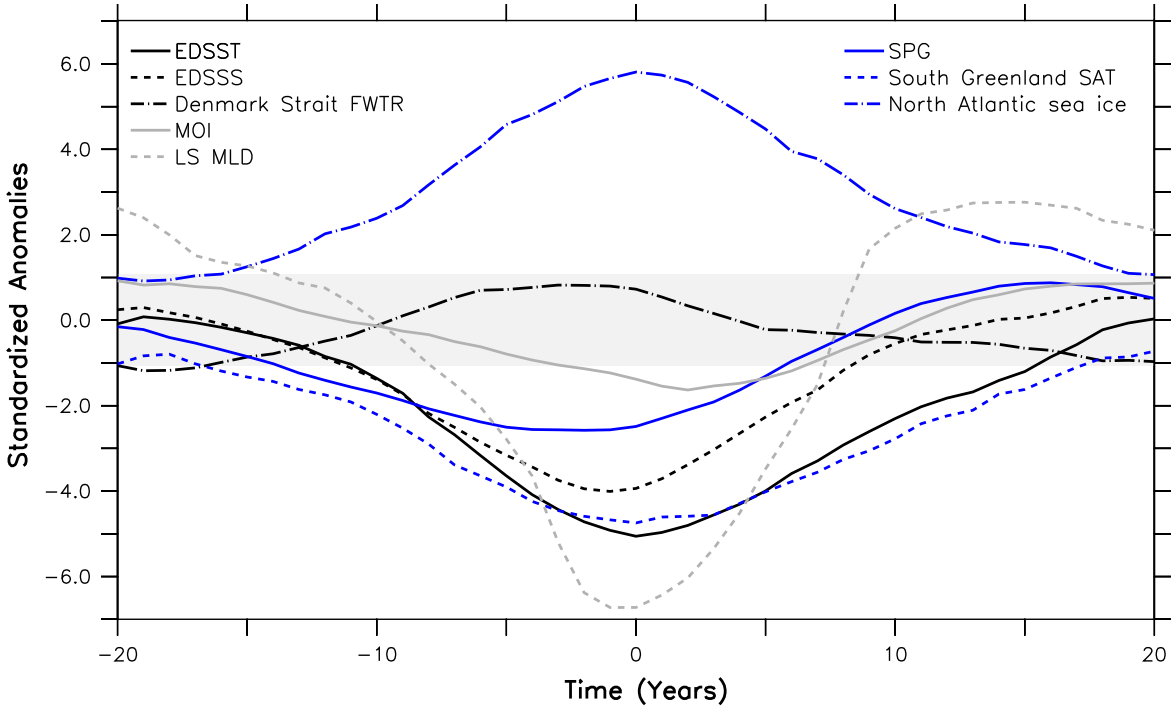

Figure 4.3: Standardized anomalies of the EDSST, EDSSS, SPG strength, MOI (the two latter defined as in Section 3.1), southward liquid FWTR through the Denmark Strait, late-winter (March) sea ice concentration for the Atlantic sector (averaged between 30°N–90°N and 100°W–0°), southern Greenland SAT (averaged between 60°N–65°N and 40°W–50°W), and Labrador Sea MLD in March (averaged between 55°N–60°N and 40°W–50°W), during the previous and following 20 years of the composite of 10 cold events selected from the Past1000s (triangles in Fig. 4.1b). Year 0 corresponds to the coldest year of the event. Standardization is done with respect to PiControl after smoothing with an 11-year running mean. For the sake of clarity, we only show a single interval of significance at the 99% confidence level (between ±1.1; shading), corresponding to the largest non-significant anomaly among all depicted variables; anomalies exceeding this interval are hence always significant.

EDSST and Eirik Drift SSS (hereafter EDSSS) changes on decadal and longer time scales are very highly correlated ($r \sim 0.8$; $p<0.05$) throughout the entire millennium in all the Past1000s (not shown). Within the northern North Atlantic, freshening when cooling, and vice versa, is also described by marine proxy-based reconstructions for the last millennium [Moffa-Sánchez et al., 2014a, , H. F. Kleiven et al., personal communication, 2014] and by recent direct measurements [Yashayaev, 2007].

The anomalous pattern in oceanic surface properties during the cold events (Figs. 4.2 and 4.3) is mainly explained by a northwestward contraction of the SPG (Fig. 4.2c). In its climatological mean (Fig. 4.2c, contours), the northern branch of the SPG transports relatively warm and saline water from the North Atlantic Current westward into the Labrador Sea via the Irminger Current. Thus, a shrinking SPG, which shows statistically significant negative anomalies about 14 years before the peak of the event (Fig. 4.3), corresponds to progressively colder and fresher surface conditions in the western subpolar North Atlantic (Fig. 4.3). These latter therefore result from reduced volume transport within the northern SPG, which advects less heat and salt westward, and not from the transport of waters with fresher and colder

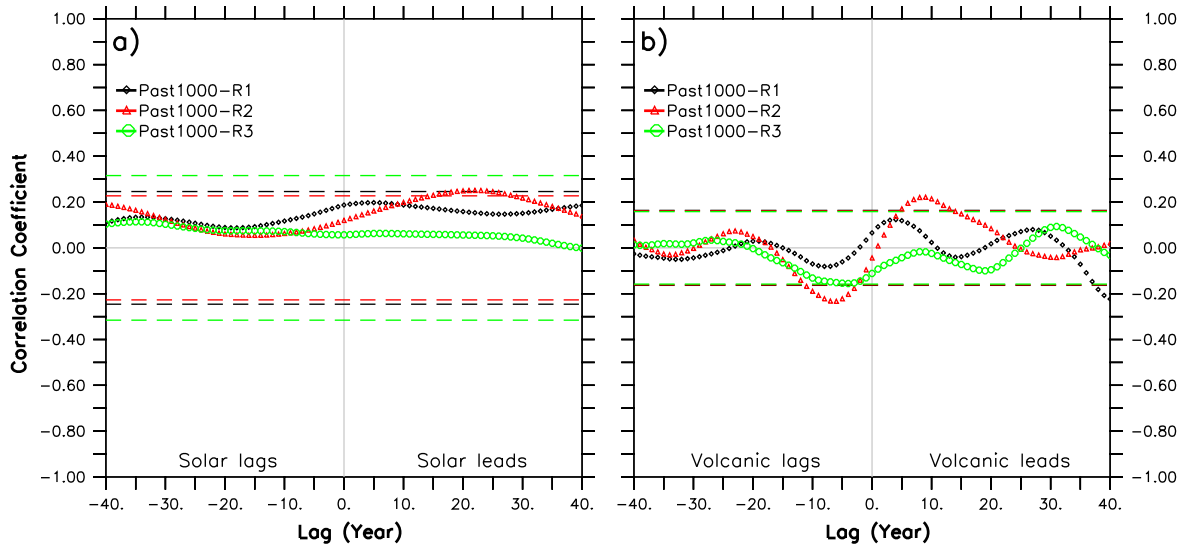

Figure 4.4: Lag-correlations between the EDSST and **(a)** the TSI or **(b)** the volcanic forcing (Fig. 4.1a) in Past1000-R1 (black diamonds), R2 (red triangles), and R3 (green circles), after smoothing with an 11-year running mean. Horizontal dashed lines identify the corresponding 95% confidence interval.

anomalies from the Arctic via the East Greenland Current, as observed, for instance, during the 20th-century Great Salinity Anomaly [Gelderloos et al., 2012]. Other sources of heat or freshwater to the area, like local surface fluxes (not shown) or the freshwater transport (FWTR) southward from the Arctic Ocean through the Denmark Strait (Fig. 4.3), show no clear contribution to the surface anomalies during the cold events, in contrast to what was deduced from climate reconstructions [e.g., Moffa-Sánchez et al., 2014b].

The weakening of the SPG can be triggered either by a substantial reduction in the wind-stress curl over the Irminger Current, or by differential density anomalies between the gyre's local center and boundaries, negative to the west and positive to the east (not shown), as has been also described by previous studies based on models of diverse complexity [e.g., Langehaug et al., 2012; Born and Stocker, 2014]. In either case, once the SPG starts to weaken, the reduced westward advection of salinity incites a density decrease at the upper levels of the western subpolar basin. With ocean convection here largely controlled by surface densities, and the latter mainly by salinity, relatively light surface waters reinforce water column stability and, eventually, shut down late winter convective mixing at the peak the cold events (Figs. 4.2d, contours, and 4.3). Colder surface conditions in the Labrador Sea in turn reduce the heat flux to the atmosphere and thus the buoyancy loss. This further strengthens water column stratification, contributing to the shutdown of the oceanic deep convection as well [Gelderloos et al., 2012]. The latter reinforces the SPG weakening by maintaining fresher (hence lighter) anomalies at the surface subpolar basin and, thereby, by reducing the density gradient within the gyre [Born and Stocker, 2014]. These positive feedbacks dominate the northern North Atlantic climate variability in the initial developing phase of the cold events, which lasts about 10–15 years (Fig. 4.3). Then, the induced surface cooling becomes sufficiently strong to compensate the haline-driven decrease in surface density in the Labrador Sea. As a result, surface densities progressively increase here until the water column becomes again unstable, enhancing oceanic deep convective mixing (Fig. 4.3). The latter strengthens the SPG, which in turn reinforces

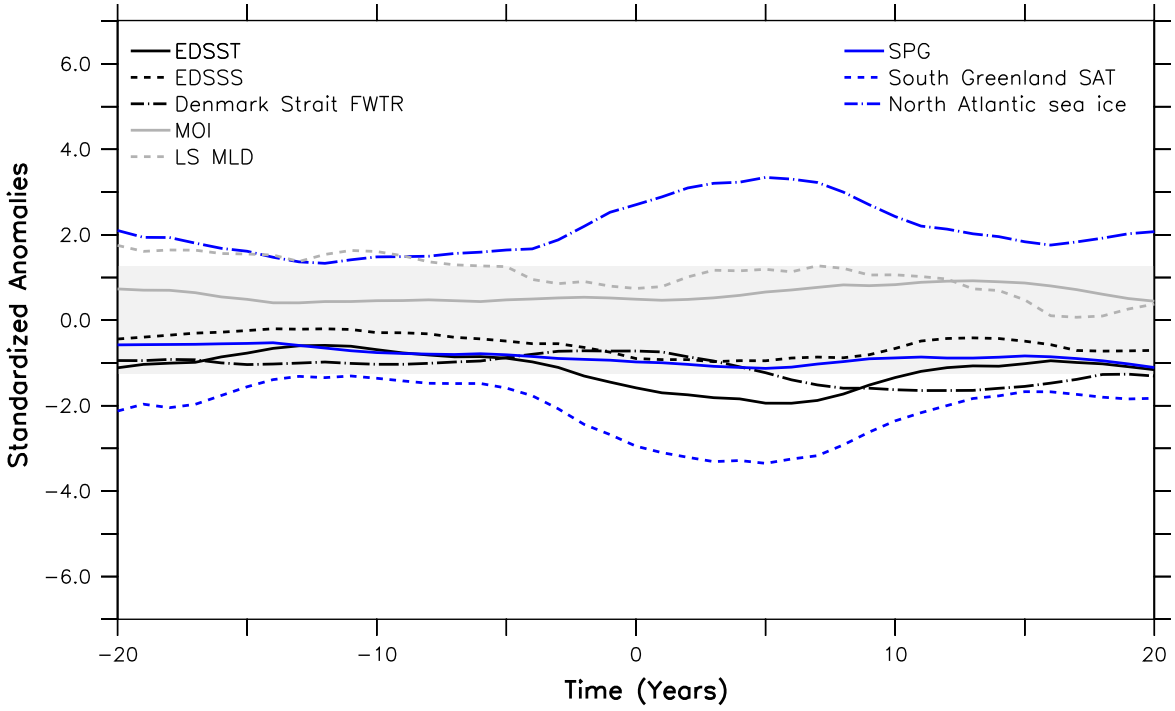

Figure 4.5: Standardized anomalies during the previous and following 20 years of the composite of seven strong volcanic eruptions during the past millennium (vertical bars in Fig. 4.1b). Year 0 corresponds to the year of the eruption. Calculation is done as in Fig. 4.3. Shading masks non-significant anomalies at the 99% confidence level (between ±1.3), considering the same range for all variables, as in Fig. 4.3.

the advection of heat and salt westward into the Labrador basin. EDSSTs and EDSSSs thus gradually increase toward conditions similar to those before the cold event within about 2–3 decades (Fig. 4.3), although with a slower recovery for the EDSST than for the EDSSS. The simulated weakening of the subpolar barotropic circulation in the North Atlantic throughout such events agrees with reconstructions of the current speed strength over the Eirik Drift during similar cold periods in the last millennium [H. F. Kleiven et al., personal communication, 2014].

A reduced northward HTTR by a slowed AMOC is often considered as the main trigger of anomalously cold conditions in the North Atlantic [e.g., Knight et al., 2005]. In contrast to the SPG, the AMOC shows no significant weakening preceding the peak of the cold events (Figs. 4.2g and 4.3). Instead, the deep water formation shutdown in the Labrador Sea during the cold events drives a progressive and delayed decline of the AMOC (Figs. 4.2h and 4.3), with the minimum strength typically occurring about 5 years after the coldest year (Figs. 4.2i and 4.3). An important AMOC weakening can thus also develop due to anomalous SPG-driven fresher surface conditions, and not only due to larger freshwater contributions from the Arctic Ocean [e.g., Miller et al., 2012; Moffa-Sánchez et al., 2014b].

The same general mechanism is at play for the ensemble of analogous cold events identified in PiControl, determined with a selection criterion based on the distribution of PiControl EDSST anomalies (Figs. 4.6 and 4.7). The mechanism therefore pertains to internal variability of the North Atlantic climate.

Unlike during a cold event, the response of the North Atlantic climate to the strongest volcanic eruptions is mainly characterized by an expansion of the sea ice within the North

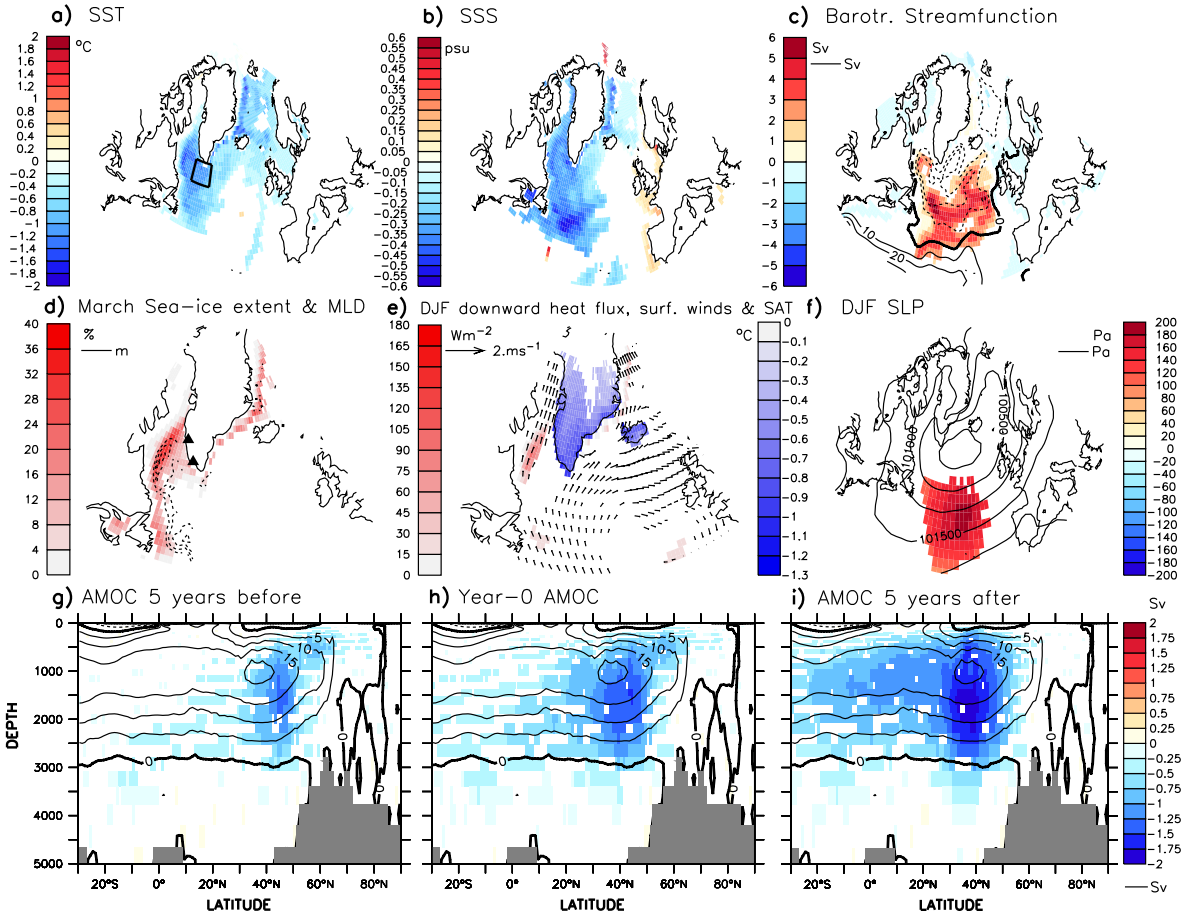

Figure 4.6: Anomalies for the composite of four cold events selected from PiControl (gray and blue triangles in Fig. 4.1c), calculated as in Fig. 4.2. **(d)** Ocean MLD shown here is in contours at 250 m intervals.

Atlantic and anomalously cold conditions at the Eirik Drift site and over South Greenland for about 10 years after the eruption (Figs. 4.5). No clear signal is detected in the other variables discussed in Fig. 4.3 after the eruption, and especially a weakening of the SPG, which is the main mechanism underlying the cold events described here. We hence exclude strong volcanic eruptions as their possible trigger.

There are several arguments that support the hypothesis that cold events like those described here could have influenced deeply population in Greenland in the 13th and 14th centuries. For instance, anomalously cold upper-ocean conditions enhance winter sea ice growth in the western subpolar North Atlantic (Fig. 4.2d, shading) for about 20–30 years during a cold event (Fig. 4.3). The simulated sea ice growth agrees well with diatom-based reconstructions [e.g., Massé et al., 2008] and with historical records during the end of the Norse colonies in Greenland [Ogilvie et al., 2000]. With the Norse settlements located in the western coast of Greenland (Fig. 4.2d, triangles), the anomalously large sea ice extent would conceivably have hindered navigation[1], isolating the fjords where the Norse were settled from the open sea, as well as seal hunting offshore [Dugmore et al., 2012].

[1]Even severe winters nowadays can render coastal voyages along the Labrador Sea coasts impossible, as for example during the winter of 1991/92 [Fagan, 2000]

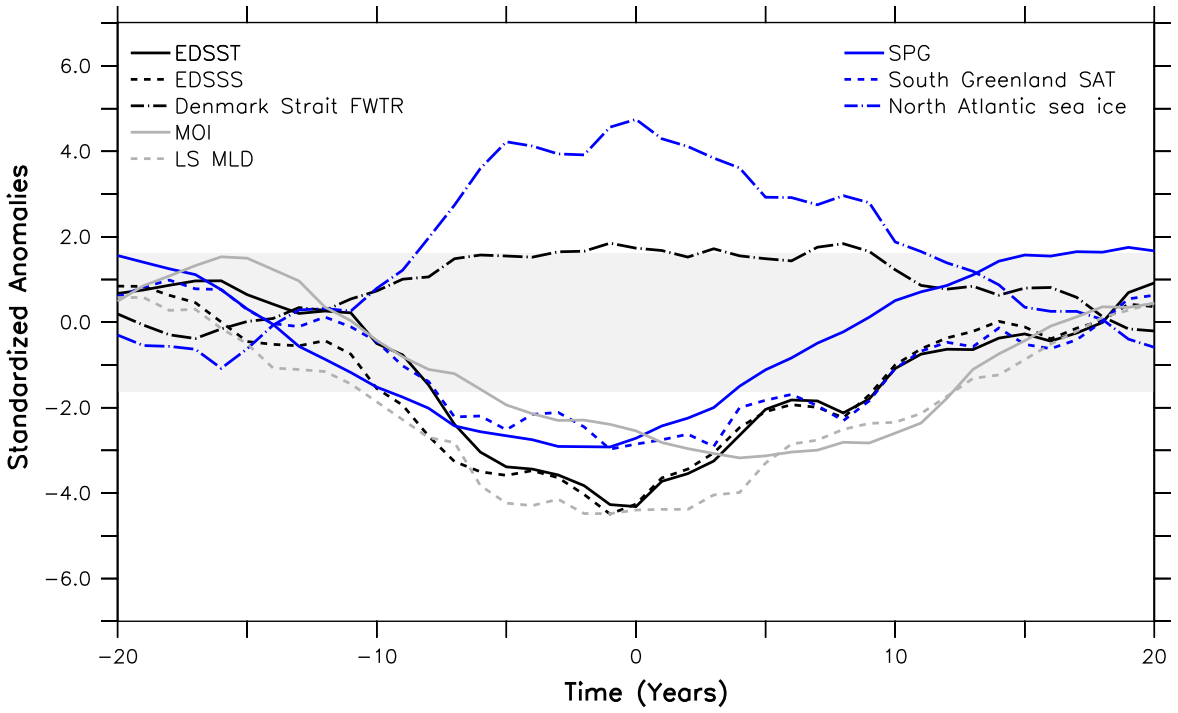

Figure 4.7: Standardized anomalies during the previous and following 20 years of the composite of four cold events selected from PiControl (gray and blue triangles in Fig. 4.1c). Year 0 corresponds to the coldest year of each cold event. Calculation is done as in Fig. 4.3. Shading masks non-significant anomalies at the 99% confidence level (between ±1.6), considering the same range for all variables, as in Fig. 4.3.

Increased sea ice cover in the Labrador Sea also hampers heat fluxes between the ocean and the atmosphere in the wintertime (Fig. 4.2e, red shading), which in turn results in a large-scale cooling of the overlying air masses. Anomalously cold surface atmospheric conditions and extended sea ice cover in the Labrador Sea promote increased atmospheric stability [Hoskins and Karoly, 1981], reducing the strength of the low-pressure systems over the North Atlantic during the cold events. This leads to a winter SLP pattern that consistently entails significant positive anomalies over the western subpolar North Atlantic, and that describes a blocking-like structure (Fig. 4.2f). This contrasts with previous studies that associated extremely cold conditions in the Labrador Sea during the instrumental period with positive NAO phases [Visbeck et al., 2003]. Our results are in general agreement with previous model-based results for the last millennium [e.g., Moffa-Sánchez et al., 2014a], although in Moffa-Sánchez et al. [2014a] the center of positive pressure anomalies is located further east, over the British Isles and during periods of reduced solar incoming radiation.

During the cold events, the anomalous northward atmospheric flow resulting from SLP anomalies (Fig. 4.2e, arrows) transports relatively cold near-surface air from the Labrador Sea and the expanded sea ice cap toward south Greenland. Here, significant colder conditions (Fig. 4.2e, blue shading) can last for as long as four decades (Fig. 4.3), in phase with the oceanic surface cooling. Anomalous cold conditions over the Norse settlements can thus result from locally induced oceanic cooling west of Greenland. Major hemispheric-scale climate fluctuations are therefore not necessary to explain the decadal cold periods reconstructed in this region for the last millennium. As further possible stress factors to the Norse societies,

during the simulated cold events the number of days per year with temperatures above the freezing point or of free-snow surface is reduced by between 10 and 20% of the climatology for the region of the Greenland settlements (not shown). In the most extreme case, there are as few as 20 days without snow cover in a year, one of the minimum values detected across all of the simulations. Such reduction implies prolonged periods of unusually or even extremely short harvest seasons. The negative impact on stock supply of these environmental conditions might have posed a high risk of long famines to the local population. Norsemen could then have shifted their dietary from terrestrial farming to marine hunting [Arneborg et al., 2012], although it is also suggested that this adaptation might have limited further changes under transforming socioeconomic agents, eventually causing the failure of the settlements in Greenland [Dugmore et al., 2012].

4.4 Conclusions

This Chapter used last millennium climate simulations to describe and attribute the mechanism governing decadal-scale cold events in the northern North Atlantic seen in temperature reconstructions of this period. Our results indicate that:

1. Decadal cold events in the northern North Atlantic can develop due to internal climate variability alone, although the role of external forcing cannot be excluded, especially concerning the strength of the cold events.

2. The cold events are amplified by positive feedbacks within the subpolar North Atlantic linked to a weakening of the SPG. The associated shutdown of the Labrador Sea deep convection provides a major negative feedback to the cold events, whose dampening phase is then dominated by substantial weakening of the AMOC. The latter thus occurs as a result of anomalous surface salinity conditions driven by changes of the SPG strength, and not as a result of a larger freshwater contribution from the Arctic Ocean. Dynamics underlying the cold events described here thus differ from those explaining similar events during the observational period.

3. Living conditions over Greenland notably deteriorate during the cold events due to locally induced anomalous climate situation. A hemispheric-scale climate reorganization is not necessary to explain reconstructed changes within the area. Especially, a series of cold events might have contributed to demise the Norse settlements in Greenland.

Chapter 5

An abrupt weakening of the subpolar gyre as trigger of Little Ice Age-type episodes

We investigate the mechanism and impacts of a decadal-scale weakening shift in the strength of the SPG that is found in one among three last millennium simulations with a state-of-the-art Earth system model. The SPG shift triggers multicentennial anomalies in the North Atlantic climate driven by long-lasting internal feedbacks relating an anomalous oceanic and atmospheric circulation, sea ice extent, and upper-ocean salinity in the Labrador Sea. Yet changes throughout or after the shift are not associated with a persistent weakening of the AMOC or a shift in the NAO. The simulated transition into an anomalous North Atlantic climate state after the SPG shift agrees well with reconstructed evidence of a similar event between the relatively warm medieval climate and the colder LIA, except for the timing of occurrence. In the model, the SPG shift is caused by a rapid increase in the freshwater export from the Arctic and associated freshening in the upper Labrador Sea. Such freshwater anomaly relates to prominent thickening of the Arctic sea ice, following the cluster of relatively small-magnitude volcanic eruptions by 1600 CE. Sensitivity experiments without volcanic forcing can nonetheless produce similar abrupt events; a necessary causal link between the volcanic cluster and the SPG shift can therefore be excluded. Instead, preconditioning by internal variability explains discrepancies in the timing between the simulated SPG shift and the reconstructed estimates for the LIA onset.

5.1 Introduction

The SPG influences the North Atlantic climate by modulating the transport of heat and salt between the North Atlantic and the Arctic oceans and, particularly, into the Nordic and Labrador seas, where deep water formation takes place (Fig. 1.2) [e.g., Grossmann and Klotzbach, 2009]. Variations in the strength and shape of the SPG can lead to major changes in, for example, the intensity of the AMOC [e.g., Hátún et al., 2005; Moreno-Chamarro et al., 2015] or the distribution of sea ice in the Arctic [e.g., Yoshimori et al., 2010; Jungclaus et al., 2014]. A recent paleoceanographic reconstruction of the Atlantic mid-depth (600–1300 m) gyre circulation over the past 1500 years [Copard et al., 2012] suggested that the SPG weakened between the MCA and the LIA. Although the abruptness of this SPG weakening could not be well defined due to the relatively poor temporal resolution of the proxy used, the finding is consistent with other climate reconstructions from the North Atlantic that do indeed present an abrupt—in some decades—change in the 13th and 14th centuries: climate reconstructions, for example, of upper-ocean temperature [e.g., Sicre et al., 2008, 2014; Ran et al., 2011; Miettinen et al., 2012, 2015; Moffa-Sánchez et al., 2014b] and salinity in the North Atlantic [e.g., Jensen et al., 2004; Moffa-Sánchez et al., 2014b], summer temperatures of northeastern North America [Gennaretti et al., 2014], ice cap growth of the Arctic Canada and off Iceland or East Greenland [Massé et al., 2008; Miller et al., 2012; Miettinen et al., 2015], and of the inflow of Atlantic waters into the Nordic Seas [Dylmer et al., 2013]. Yet attribution and physical mechanism responsible for such an abrupt SPG weakening remain unclear, as well as the connection between this event and the other climate changes reconstructed in the North Atlantic during the LIA. This Chapter thus aims at better understanding the SPG variability on decadal and longer time scales, its related dynamics, and how it contributed to shaping the North Atlantic climate during the last millennium.

A reduction in the meridional heat transported by the AMOC was invoked in earlier studies to explain anomalous cold conditions in the North Atlantic reconstructed during the LIA [e.g., Lund et al., 2006; Miller et al., 2012; Lehner et al., 2013]. This hypothesis, however, found no support in a recent reconstruction of the AMOC strength [Rahmstorf et al., 2015]. Other studies suggested that the cold North Atlantic could have been associated with a shift in the phase of the NAO [Trouet et al., 2009; Copard et al., 2012], as it is well known that the NAO influences the SPG variability through wind forcing and surface buoyancy fluxes [e.g., Eden and Willebrand, 2001; Deshayes and Frankignoul, 2008]. The NAO reconstruction of Trouet et al. [2009] was nevertheless contested in a later study [Lehner et al., 2012], and Ortega et al. [2015] presented an alternative NAO reconstruction in which no phase shift was found between the MCA and LIA. Further uncertainty arises from the fact that the previous studies attributed these North Atlantic climate anomalies during the LIA to either internal climate variability [Drijfhout et al., 2013] or external forcing, including a series of strong, decadally paced volcanic eruptions [e.g., Miller et al., 2012; Schleussner and Feulner, 2013] and changes in the incoming solar radiation during the 13th century [Lehner et al., 2013].

In this Chapter, we use the Past1000 ensemble (see Chapter 2 for further detail) to investigate the mechanisms of decadal to centennial SPG variability under pre-industrial conditions and their implications for the multicentennial climate variability in the North Atlantic. We concentrate on dynamics of an abrupt weakening shift in the SPG strength that is simulated in one ensemble member; this shift separates two relatively stable, multicentennial North Atlantic climate regimes, so that post-shift features resemble those reconstructed during the LIA. We thus aim to answer the following questions: How does this abrupt SPG transition

compare with other dominant features of the simulated SPG strength variability on decadal and longer time scales? (Sections 5.2 and 5.3) What are the main differences between the two climate regimes before and after the shift? And, what mechanism allows the latter regime to be stable for at least two centuries? (Section 5.4) What are the potential triggering factors of the abrupt shift? (Section 5.5) Here, we also use sensitivity experiments to assess the relative role of the initial climate conditions and the imposed volcanic forcing during the shift (Section 5.5.2). To close the Chapter, Section 5.6 discusses and compares modeling results with some of the available reconstructions for the LIA, and Section 5.7 lists our main conclusions.

5.2 The subpolar gyre strength in the Past1000 ensemble

In order to describe SPG variability above decadal time scales during the last millennium, we use the SPG strength defined as in Section 3.1, further smoothed with an 11-year running mean (Fig. 5.1a). Overall, SPG variations in all transient simulations fall within the range of variability in PiControl (Fig. 5.1a, dot-dashed and dotted lines). Two remarkably different behaviors can nevertheless be identified in the Past1000s: whereas the SPG weakens progressively at an almost constant rate throughout the entire last millennium in R1 and R2 (with trends of the order of –0.10 Sv/century), the SPG in R3 shows a rapid shift from a strong to a weak state around 1600 CE. An algorithm for discrete level identification [Little et al., 2011] allows for an objective characterization of the shift: it occurs in about two decades, accounts for a reduction of 0.72 Sv, and separates two stationary states, each covering at least 250 years (horizontal solid lines in Fig. 5.1a for Past1000-R3; also Fig. 5.8). Unlike in Past1000-R3, discrete levels in R1 and R2 succeed each other more rapidly in time and are separated by smaller steps, a behavior that corresponds well with a smooth, long-lasting slowdown. Yet, levels in the three Past1000s take similar values during the last two centuries, ranging between the 5th and the 25th percentiles of the SPG strength in PiControl. A weak SPG state thus robustly develops throughout the last millennium in the three simulations, either smoothly or abruptly.

5.3 Modes of variability of the North Atlantic barotropic streamfunction

In the following, we study the leading modes of variability of the North Atlantic barotropic streamfunction and their major driving mechanisms in order to disentangle the dynamics underlying the decadal-scale shift in the SPG. We focus this analysis on Past1000-R3, aiming at better understanding the physical mechanisms behind the two different circulation regimes of the SPG. Below-described results can, nonetheless, be extended to the other two Past1000s and PiControl. Figure 5.2 illustrates the Empirical Orthogonal Functions (EOFs) and Principal Components (PCs) of the first two variability modes of the barotropic streamfunction in the Atlantic Ocean, between 20°S–80°N and 80°W–20°E, in Past1000-R3. Modes are calculated after applying an 11-year running mean to extract variability on decadal and longer time scales. The first two modes explain together about 50% of the total variability; higher-order modes explain each less than 7% of the total variance and are, therefore, not considered here.

The first mode, hereafter referred to as Intergyre Gyre (28% of the explained total variance; Fig. 5.2a), is characterized by anticyclonic (positive) anomalies straddling the boundary

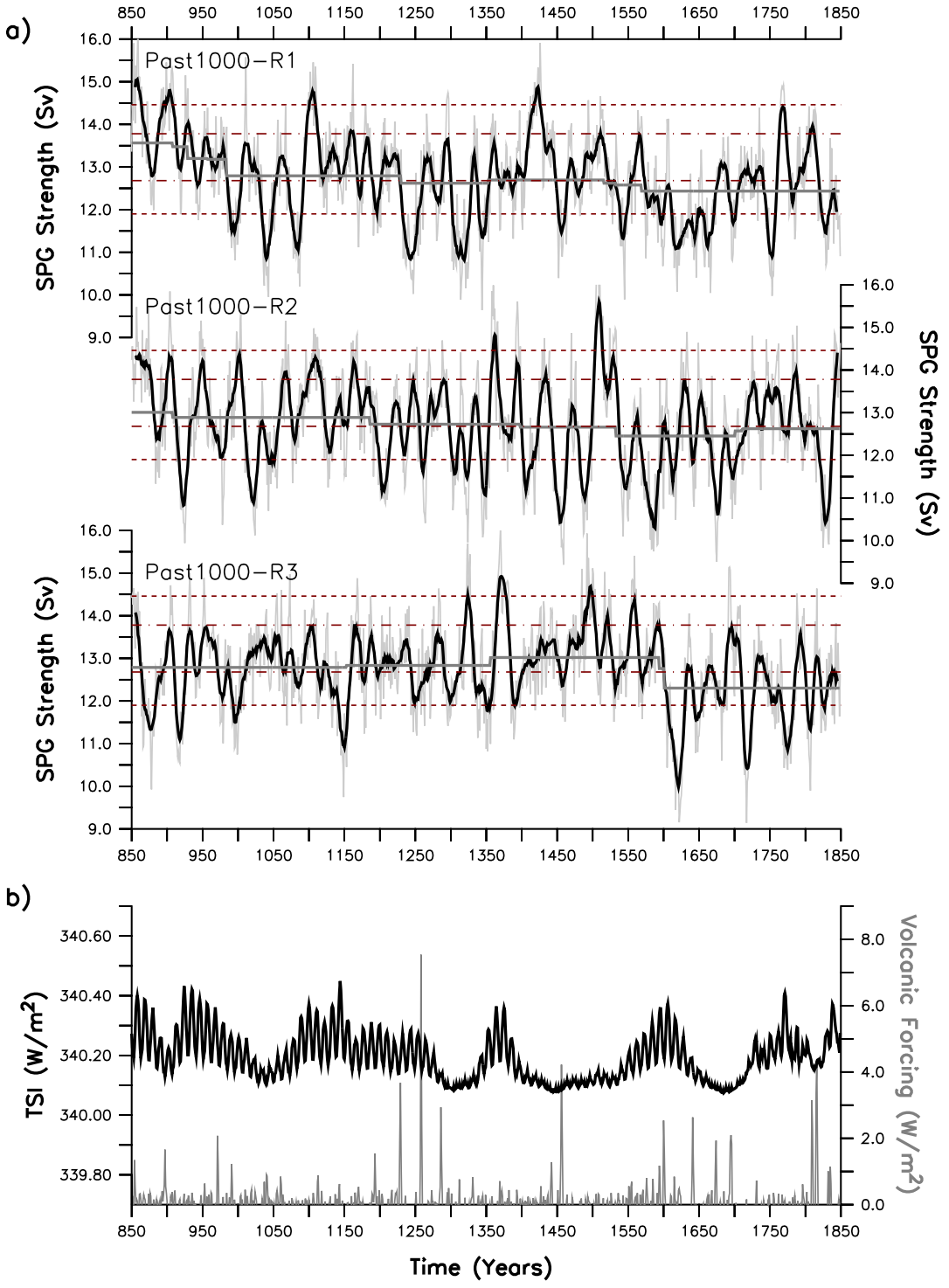

Figure 5.1: **(a)** Index for the SPG strength (in Sv) during the last millennium: light-gray and solid-black lines are respectively annual averages and the corresponding 11-year running mean. Horizontal dash-dotted and dashed lines respectively account for the 25th–75th and 5th–95th percentiles of the SPG strength in PiControl. Horizontal solid lines are the discrete levels extracted following the algorithm described in Little et al. [2011]. **(b)** Solar and volcanic forcings in Past1000-R3, as in Fig. 2.1.

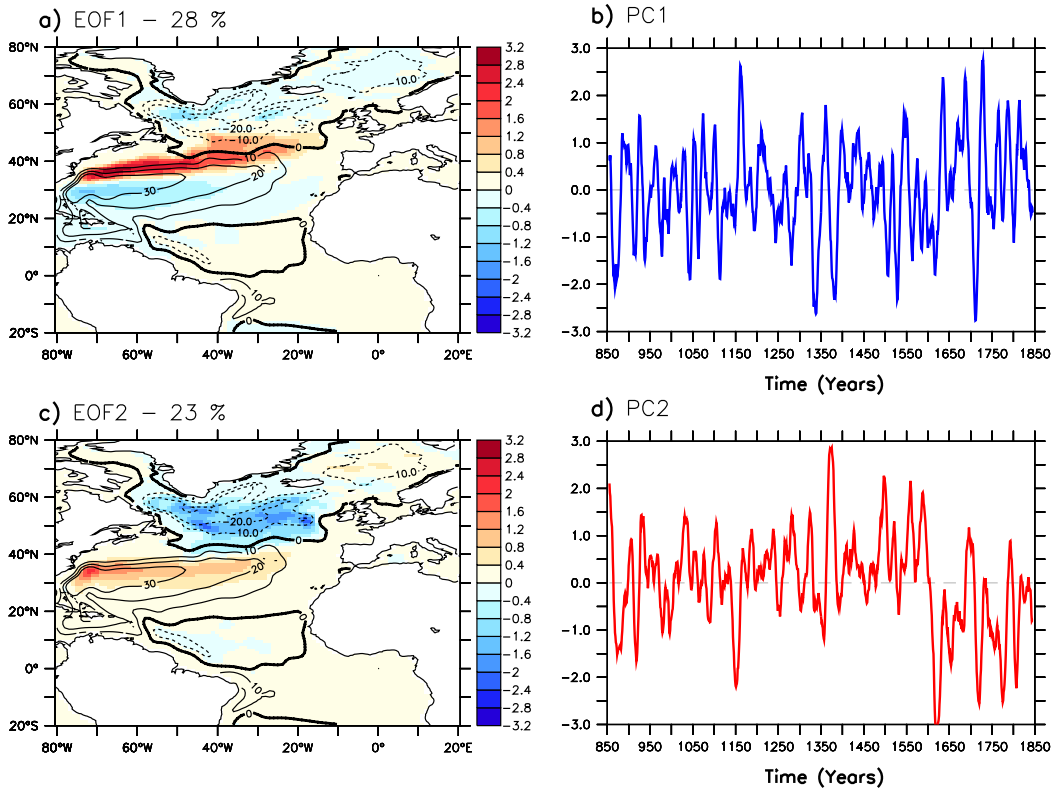

Figure 5.2: EOFs (in Sv; shading in left panels,) and PCs (dimensionless; right panels) of the first (also referred as Intergyre Gyre; upper panels) and second (also referred as Mean Mode; lower panels) leading modes of the North Atlantic barotropic streamfunction above decadal time scales in Past1000-R3. Modes are calculated after applying an 11-year running mean. Explained variances are indicated in **(a)** and **(c)**, with contours representing the climatological mean in PiControl at 10 Sv intervals.

between the subtropical gyre and the SPG. The most remarkable feature of its PC (Fig. 5.2b) is a prolonged period, roughly since 1620 CE, of dominating positive phases. This mode resembles well the anomalous circulation pattern in the North Atlantic Ocean introduced by Marshall et al. [2001] in response to meridional shifts in the zero-line of the wind stress curl between NAO phases. The Intergyre Gyre shows maximum in-phase correlation with the NAO index at lag 0 years (Fig. 5.3a, red triangles), which illustrates the fast adjustment of the oceanic gyre circulation to NAO-related wind stress anomalies. Beside this, the Intergyre Gyre mode lags behind late-winter (March) MLD in the Labrador Sea by 12 years (Fig. 5.3a, green circles), thus supporting earlier studies that highlighted a connection between the North Atlantic surface circulation and deep water formation [e.g., Eden and Willebrand, 2001]. The Intergyre Gyre mode also lags behind the SPG strength and the northward oceanic HTTR at subpolar latitudes (55°N) by 10 years (Fig. 5.3a, blue diamonds and black squares respectively). In turn, the SPG strength and the Labrador Sea MLD are themselves well correlated, with the SPG lagging by 2 years according to the maximum values in their correlation coefficient (of about 0.80; $p<0.05$). These results indicate that a reinforced oceanic deep mixing in the Labrador Sea can lead to a SPG spin-up and to a negative Intergyre Gyre phase, and vice versa. Such a delayed response might be caused by a meridional shift in the boundary between the subpolar and the subtropical gyres; also, it might occur associated with

the development of a particular NAO/Intergyre Gyre phase in response to changes in the northward heat transport by the SPG and, thereby, in the meridional atmospheric temperature gradient and jet stream intensity over the North Atlantic [Grossmann and Klotzbach, 2009].

The second mode of the North Atlantic barotropic streamfunction, hereafter referred to as Mean Mode (23% of the explained total variance; Fig. 5.2c), has a dipole structure with a cyclonic (negative) and anticyclonic center of action over the SPG and subtropical gyre respectively. This pattern thus represents a strengthening of the climatological mean circulation for positive values of its PC, and vice versa. Its PC bears a striking resemblance to the SPG strength and, like this, shows a conspicuous abrupt transition toward a period of almost permanent negative anomalies at around 1600 CE (Fig. 5.2d). In fact, this mode is highly correlated with the SPG strength at lag 1 year, with the latter leading (Fig. 5.3b, blue diamonds). The Mean Mode is also highly correlated with the mean MLD in the Labrador Sea, lagging by 2 years (Fig. 5.3b, green circles), and with the subpolar HTTR, leading by 1 year (Fig. 5.3b, black squares). An enhancement in the Labrador Sea MLD can thus cause a synchronous reinforcement of both gyres (i.e., a positive Mean Mode phase) and of the HTTR poleward, and vice versa. A less clear connection is found, in contrast, between the Mean Mode and the NAO index at lag 4–5 years, of low significance (Fig. 5.3b, red triangles), which might be associated with NAO-related changes in the oceanic deep mixing within the Labrador Sea [e.g., Eden and Willebrand, 2001; Deshayes and Frankignoul, 2008]. According to these results, changes in the Intergyre Gyre and the Mean Mode after 1600 CE are related to the abrupt shift in the SPG strength and associated northward HTTR, as well as to a reduction in the deep water formation in the Labrador Sea, but not particularly to a shift between NAO phases. This is confirmed in the following Section.

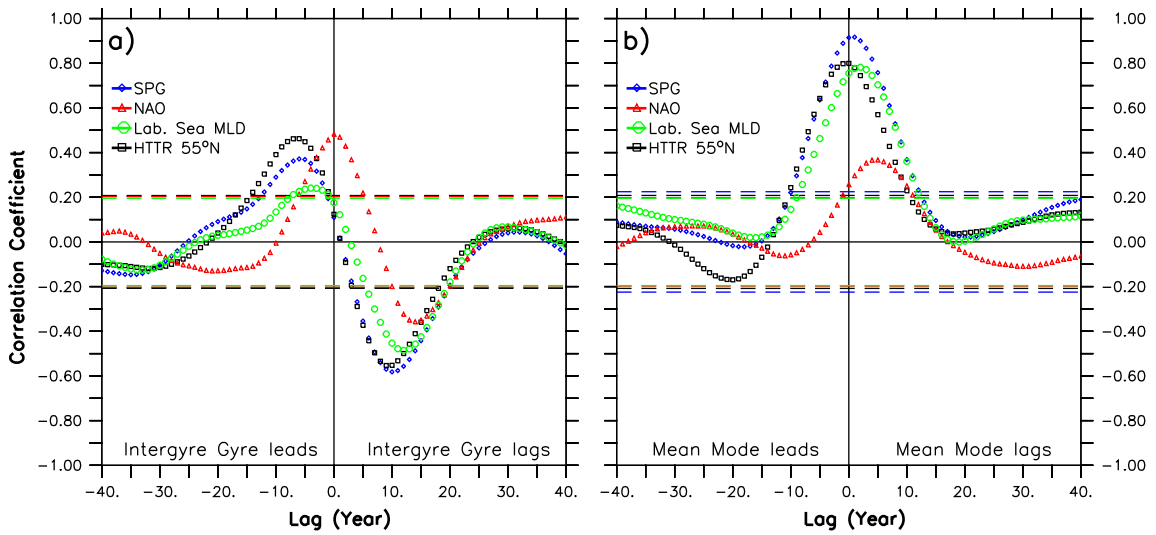

Figure 5.3: Cross-correlation profiles between the PCs of the first (Intergyre Gyre, in **a**) and second (Mean Mode, in **b**) modes of the North Atlantic barotropic streamfunction (from Fig. 5.2) and the low-pass filtered SPG strength (blue diamonds), the NAO (red triangles), late-winter (March) Labrador Sea MLD (green circles), and oceanic meridional HTTR at 55°N (black squares) in Past1000-R3. Time series of the SPG strength, NAO, MLD, and HTTR are defined and shown in Fig. 5.5. Calculations are done after applying an 11-year running mean. Significances at the 95% level are given by horizontal dashed lines.

5.4 North Atlantic climate regimes before and after the shift

This Section compares the two climate regimes in the North Atlantic before and after the shift in the SPG strength in Past1000-R3, and explores the mechanism that renders the later regime stable for at least 250 years. The analysis is performed assuming the pre-shift period as reference regime, and the post-shift period as the anomalous one. Figure 5.4 illustrates the differences between the mean states after (1650–1749 CE) and before (1450–1549 CE) the shift. These two periods are chosen to exclude years immediately around the SPG shift, when climate anomalies are exceptionally large (see, for instance, Fig. 5.5). Similar results are obtained if longer period are considered (for example, for the period 1350–1549 CE and 1650–1849 CE).

The reduced SPG strength after the shift is the result of a broad slowdown of the subpolar barotropic circulation, with the exception of the Irminger gyre (Fig. 5.4a). Although most of the changes in the gyre circulation lie within the subpolar region, the center of the subtropical gyre is also significantly weaker during the later regime. The post-shift anomaly pattern in the North Atlantic barotropic streamfunction thus resembles a negative phase of the Mean Mode (Fig. 5.2c). Despite such changes, a meridional shift in the location of the boundary between the subtropical and the subpolar gyres does not occur after the shift, as evidenced by the fact that the location of the zero wind-stress-curl line stays unchanged between both regimes (Fig. 5.4h).

Broadly speaking, the strength of the SPG is largely controlled by the horizontal gradient in upper-ocean densities between the gyre's center and its boundaries, and wind stress over the subpolar area [e.g., Häkkinen et al., 2011; Born and Stocker, 2014]. The former is herein represented as the difference between upper-ocean (500 m) densities in the western subpolar basin, averaged between 55°N–60°N and 50°W–60°W, and the eastern basin, averaged between 55°N–60°N and 10°W–20°W, further smoothed with an 11-year running mean (Fig. 5.5a). The zonal gradient in upper-ocean densities thus seeks to represent the difference between the gyre's center (or maximum) within the Labrador Sea, where upper-ocean density reaches maximum values, and its eastern boundary (contours in Fig. 5.4a). The zonal density gradient shows relatively high correlation with the SPG strength (maximum correlation coefficient of 0.76, $p<0.05$, at lag 0 years), which indicates that it largely controls SPG variations above decadal time scales. On the other hand, the contribution of the wind stress curl is herein accounted by spatially averaging this over the subpolar region, between 50°N–65°N and 10°W–60°W, also smoothed with an 11-year running mean (Fig. 5.5f). The wind stress curl shows a significant but relatively weak connection with the SPG strength on decadal and longer time scales for the whole millennium (maximum correlation coefficient of 0.34, $p<0.05$, with the wind stress curl leading by 3 years), although it can occasionally be linked to notable variations in the SPG, for example for the period 1350–1400 CE (see Fig. 5.5a,f). The reorganization of the climate after 1600 CE leads to changes in both the upper-ocean density gradient and wind stress curl, as discussed in the following.

The zonal gradient of upper-ocean densities appears strongly weakened as a result of the anomalous fresh, hence light, surface conditions in the western subpolar North Atlantic after 1600 CE (Fig. 5.4b), whereas post-shift changes in upper-ocean densities in the eastern subpolar North Atlantic are much smaller. In the Labrador Sea, in particular, the SSS drops by about 0.20 psu between regimes (Fig. 5.5b) and dominates over the density increase due to surface cooling (compare Fig. 5.4b,d). The surface freshening results from both an increase in the export of sea ice from the Arctic Ocean and Nordic Seas into the Labrador Sea (Fig. 5.5e, discussed below), where it melts and freshens the surface layers, and from a reduced salt

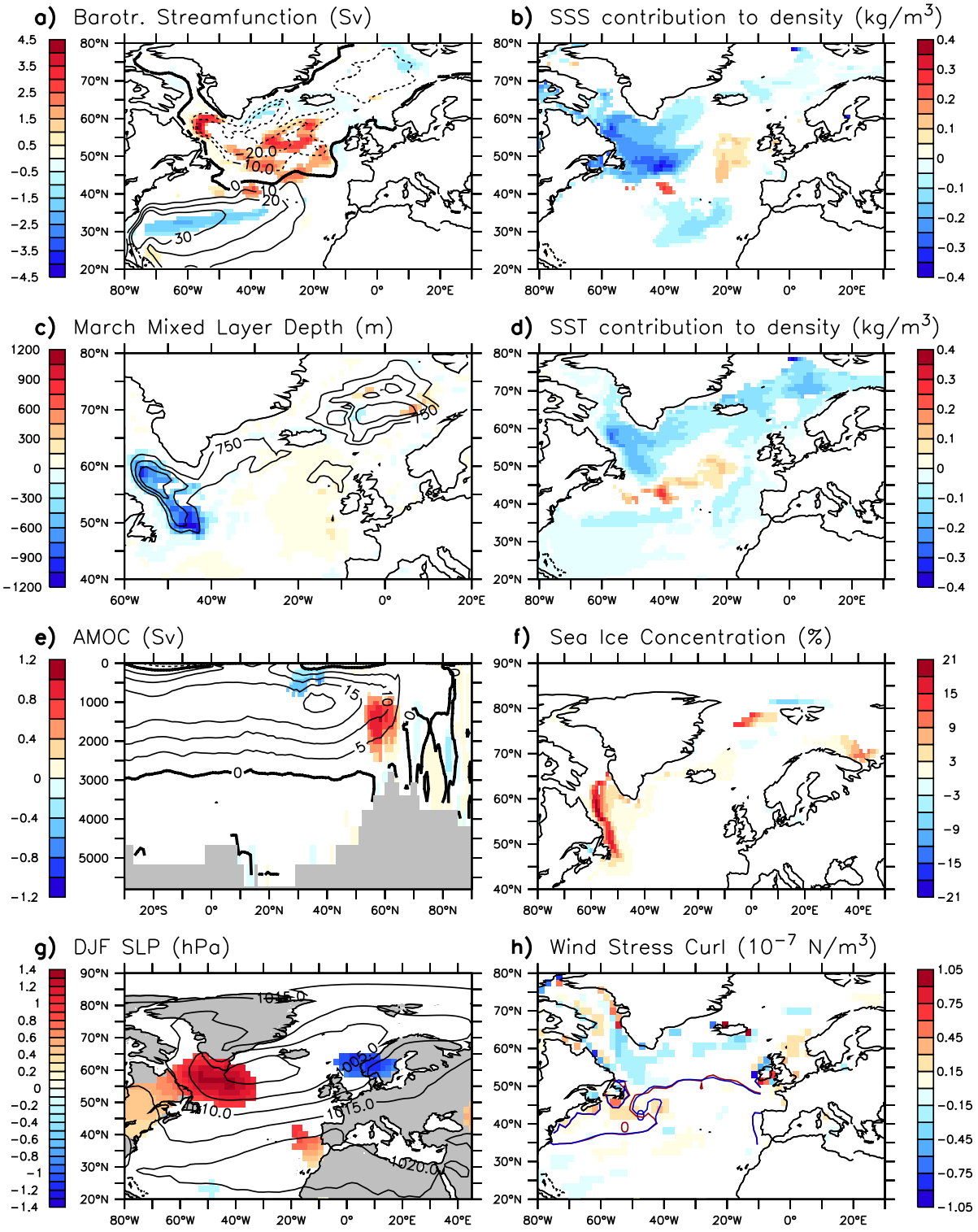

Figure 5.4: (Caption next page.)

Figure 5.4: (Previous page.) Differences between the 100-year climate means after (1650–1749 CE) and before (1450–1549 CE) the shift in Past1000-R3. Only significant anomalies above the 95% confidence level are shown based on the likelihood of occurrence of the signal in PiControl (see Section 3.2). **(a)** Barotropic streamfunction (in Sv; shading) with contours representing the climatological mean in PiControl at 10 Sv intervals (dashed/solid lines correspond to cyclonic/anticyclonic flow). **(b)** SSS contribution to the ocean surface density (in kg/m^3), assuming a linear relationship between both variables. **(c)** Late-winter (March) MLD (in m; shading), with contours representing the climatological mean in PiControl at 750 m intervals. **(d)** SST contribution to the ocean surface density (in kg/m^3), assuming a linear relationship between both variables. Note that the color scale is the same as in **(b)**. **(e)** AMOC (in Sv), with contours representing the climatological mean in PiControl at 5 Sv intervals. **(f)** Sea ice concentration in March (in percent of area). **(g)** Wintertime (DJF) SLP (in hPa; shading), with contours representing the climatological mean in PiControl at 5 hPa intervals. **(h)** Wind stress curl (in 10^{-7} N/m^3; shading), with lines accounting for the zero line before (red) and after (blue) the shift.

transport westward along the Irminger Current (not shown) due to a weaker gyre circulation. The SPG therefore self-maintains its weaker regime after 1600 CE by keeping the western subpolar basin anomalously fresh, hence light.

Changes in the deep water formation in the western subpolar North Atlantic also contribute to sustaining the weak SPG after the shift. In its climatological mean, late-winter cooling of the upper Labrador Sea induces strong vertical mixing down to a depth of several hundred meters (Fig. 5.4c, contours). This forms a core of very dense waters within the gyre's center that strengthens the zonal gradient of upper-ocean densities and, by extension, the gyre's circulation [Born and Stocker, 2014]. After the SPG shift, however, ocean deep mixing is locally hampered in the Labrador Sea, as fresher (hence lighter) surface conditions develop here (Figs. 5.4c, and 5.5b). This contributes to reducing the upper-ocean densities in the western subpolar region and, hence, the SPG strength.

Late-winter MLD in the Labrador Sea, although weaker than pre-shift conditions, still reaches values above 2000 m after the shift; deep waters are thus still formed within the Labrador Sea. Likewise, no remarkable changes occur in the oceanic deep convection within the Nordic Seas after 1600 CE (Fig. 5.4c) or in the strength of the Greenland–Scotland Ridge overflow (not shown). As a result, the SPG shift is associated with non-significant changes in the circulation pattern of the AMOC (Fig. 5.4e). The AMOC strength (MOI in Fig. 5.5c) does not exhibit any long-lasting shift after 1600 CE, in contrast to the SPG, even though it temporally weakens between 1600 CE and 1640 CE during the shift.

Changes in the large-scale circulation of the Atlantic Ocean alter the poleward oceanic HTTR. Whereas the HTTR at 26°N is only slightly reduced after the SPG shift, since it is here mostly driven by the AMOC (Fig. 5.5c), at subpolar latitudes (55°N), where it is principally driven by the SPG, the HTTR shows a conspicuous reduction from 1600 CE onwards. On the one hand, such HTTR changes lead to an accumulation of heat at mid-latitudes in the upper ($\sim$ 1000 m) North Atlantic after the shift that, in turn, induces an upper-ocean warming along the path of the North Atlantic Current up to 50°N–55°N, approximately (Fig. 5.4d). On the other hand, a smaller amount of upper-ocean heat reaching the intergyre region is consequently transported poleward along a weakened SPG's eastern branch after the shift. The resultant deficit in upper-ocean heat farther downstream leads to significantly colder surface conditions

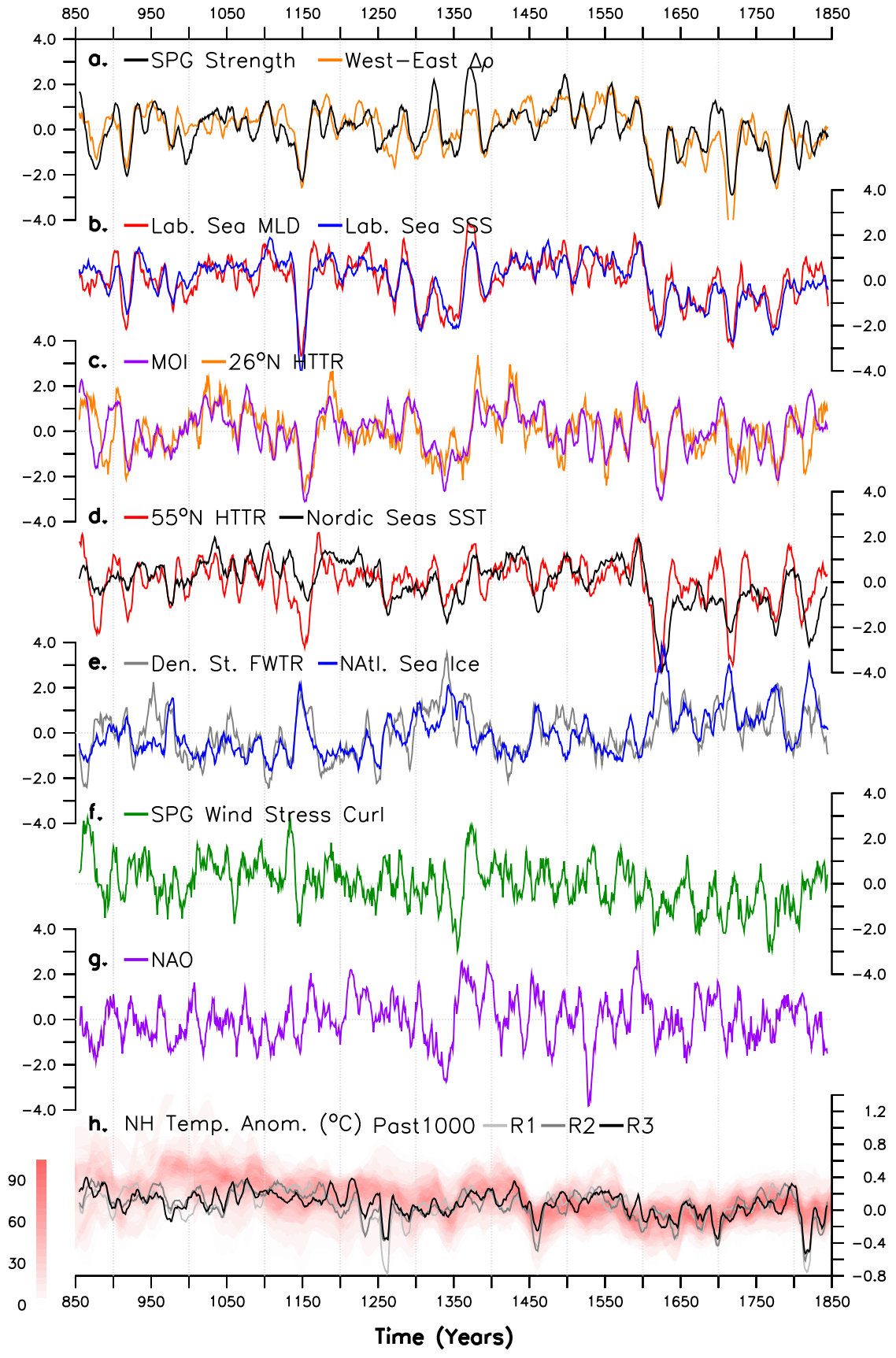

Figure 5.5: (Caption next page.)

Figure 5.5: (Previous page.) **(a–g)** Standardized anomalies of different variables in Past1000-R3. Standardization is done after applying an 11-year running mean. Values in parentheses correspond to the mean ± standard deviation in the last millennium. **(a)** SPG strength (12.77±0.80 Sv), and west–east gradient of upper-ocean densities (see Section 5.4; 0.285±0.055 kg/m^3). **(b)** Late-winter (March) MLD, and SSS in the Labrador Sea, both averaged between 45°N–63°N and 40°W–60°W (749±165 m and 33.46±0.14 psu respectively). **(c)** MOI (20.89±0.79 Sv), and meridional HTTR in the Atlantic Ocean at 26°N (0.975±0.030 PW). **(d)** Meridional HTTR in the Atlantic Ocean at 55°N (0.485±0.22 PW), and Nordic Seas SST, averaged between 65°N–80°N and 20°W–20°E (3.89±0.40 °C). **(e)** Late-winter (March) sea ice concentration in the North Atlantic sector, averaged between 50°N–85°N and 80°W–40°E (25.4±1.3 % of area), and total (liquid+solid) FWTR through the Denmark Strait (4309±370 km^3/year). **(f)** Wind stress curl averaged over the subpolar region (see Section 5.4; (1.559±0.075)·10^{-7} N/m^3). **(g)** Decadal wintertime (DJF) NAO index, calculated as in Section 3.1 after applying an 11-year running mean (61% of the explained total variance; anomaly pattern not shown, but similar to the one in Fig 1.4, left). **(h)** Simulated NH SAT anomalies in the Past1000 ensemble (in °C; gray lines), with respect to the period 1500–1849 CE and smoothed with 11-year running mean. Also, overlap of NH temperature reconstructions (in percent; shading), as in Fig. 1.1.

in both the western subpolar region and Nordic Seas, where, in particular, SSTs drop by about 0.4 °C on average after the shift (Fig. 5.5d). SATs between the two climate regimes mirror this pattern (similar to the one shown in Fig. 5.10d). The SPG shift alone is thus able to induce large-scale, long-lasting colder surface conditions in the North Atlantic sector.

Cooling of the upper Nordic and Labrador seas leads to a post-shift overall expansion and thickening of the sea ice in the North Atlantic and Arctic oceans (Fig. 5.5e); for the sea ice extent, this is particularly prominent in the Labrador, Nordic, and Barents seas (Fig. 5.4f). As a result, a larger amount of sea ice is exported toward the Labrador Sea after the shift. The total (liquid plus solid) FWTR through the Denmark Strait hence increases by about 200 km^3/year on average after the shift (Fig. 5.5e), mainly due to an increase in the solid component (not shown). Larger FWTR into the Labrador Sea also contributes to the surface freshening (Fig. 5.4b) and, by extension, helps sustain the weaker SPG regime after the shift. Besides, the insulating effect due to expanded sea ice in the northern Labrador Sea weakens the underlying surface circulation along the West Greenland and Labrador currents (Fig. 5.4a).

Colder surface conditions and expanded and thicker sea ice reduce surface heat losses in the Labrador Sea (not shown). This increases stability in the overlying atmosphere after the shift [Hoskins and Karoly, 1981], inducing statistically significant positive anomalies in winter SLP over the western subpolar North Atlantic that describe a blocking-like structure (Fig. 5.4g). The Icelandic Low appears displaced eastward from its climatological position after the shift, as illustrated by the significant negative anomalies in the winter SLP to the east of its center. This anomalous SLP pattern does not resemble any particular NAO phase (see for example Fig. 1.4), and the NAO index does not exhibit any regime change associated with the SPG shift (Fig. 5.5g). The development of anomalous high pressure south of Greenland after the shift in turn causes a statistically significant reduction of the wind stress curl over the subpolar basin, particularly to the west of the basin (Figs. 5.4h and 5.5f) that also contributes to slowing down the SPG. This mechanism illustrates the role of the atmosphere in the weaker SPG regime from 1600 CE onward.

In summary, two main contributions are found sustaining the weak SPG regime after the shift: first, a long-lasting upper-ocean freshening in the Labrador Sea that reduces the zonal gradient in upper-ocean densities within the subpolar North Atlantic, and that is further maintained by the own weak SPG and larger export of sea ice from the Nordic Seas and the Arctic; and second, a long-lasting reduction in the wind stress curl due to an anomalous blocking-like structure over the subpolar North Atlantic.

5.5 Mechanism triggering the shift in the subpolar gyre strength

This Section first describes the chain of events that leads to the development of the SPG shift in Past1000-R3, and then highlights the possible triggering mechanisms. Our dynamical interpretation is confirmed by means of sensitivity experiments.

5.5.1 The subpolar gyre shift in Past1000-R3

The volcanic cluster that peaks in 1600 CE with the eruption of the Huaynaputina volcano in Peru [Verosub and Lippman, 2008] marks the onset of the shift between North Atlantic climate regimes described in Section 5.4. This cluster is composed of volcanic eruptions of relatively small magnitude compared to other major and better-known events in the last millennium (Fig. 5.1b). Nonetheless, the cluster accumulates a negative anomaly in the globally averaged net radiative flux at the top of the atmosphere down to –5 W/m^2 right after 1600 CE, and of approximately –2 W/m^2 during the following 20 years (Fig. 5.6a). Over the 10 years following these eruptions, the NH total sea ice volume increases by 10% from 28000 km^3 to 30800 km^3 (Fig. 5.6a). The increase is remarkable north of Greenland, where the sea ice thickens, and in the Barents and Nordic seas, where the sea ice edge advances extensively southward (not shown). An anomalous, albeit of smaller amplitude, growth in the Arctic sea ice is also found in this same simulation after the strong volcanic eruptions in 1250 CE or 1815 CE (Fig. 5.5e, for the North Atlantic sector). Arctic sea ice growth typically occurs in all three Past1000s after some, though not all, strong volcanic eruptions (Fig. 4.5), in agreement with earlier studies [e.g., Zhong et al., 2011; Zanchettin et al., 2012]. Other relatively abrupt events of sea ice growth in this simulations are, in contrast, caused by internal cold events in the subpolar North Atlantic [Moreno-Chamarro et al., 2015, Chapter 4], as for example around 1150 CE or 1350 CE, and should hence not be mistaken for a response to strong volcanic eruptions.

The abrupt (in just a decade) rise in NH sea ice translates into an abrupt increase in the sea ice export from the Arctic Ocean and Nordic Seas toward the subpolar North Atlantic through the Denmark Strait (Fig. 5.6b). The solid component of the FWTR, that is sea ice, thus reaches a maximum positive anomaly of about 900 km^3/year in the 1620s CE, and remains predominantly positive thereafter until the 1660s CE. As also shown in Born et al. [2010], freshwater bound in ice can very effectively impact both oceanic deep convection and the SPG strength, because ice remains concentrated at the ocean surface during the advection, and because its maximum export is reached in late winter, during the main convection season in the subpolar North Atlantic. As the sea ice flows southward, warmer surface waters melt it progressively, decreasing the surface salinity of the upper subpolar North Atlantic and, especially, of the Labrador Sea (Fig. 5.6c). The largest salinity reduction in Past1000-R3, of about 0.5 psu, thus occurs around 1620 CE, synchronously with the largest freshwater export

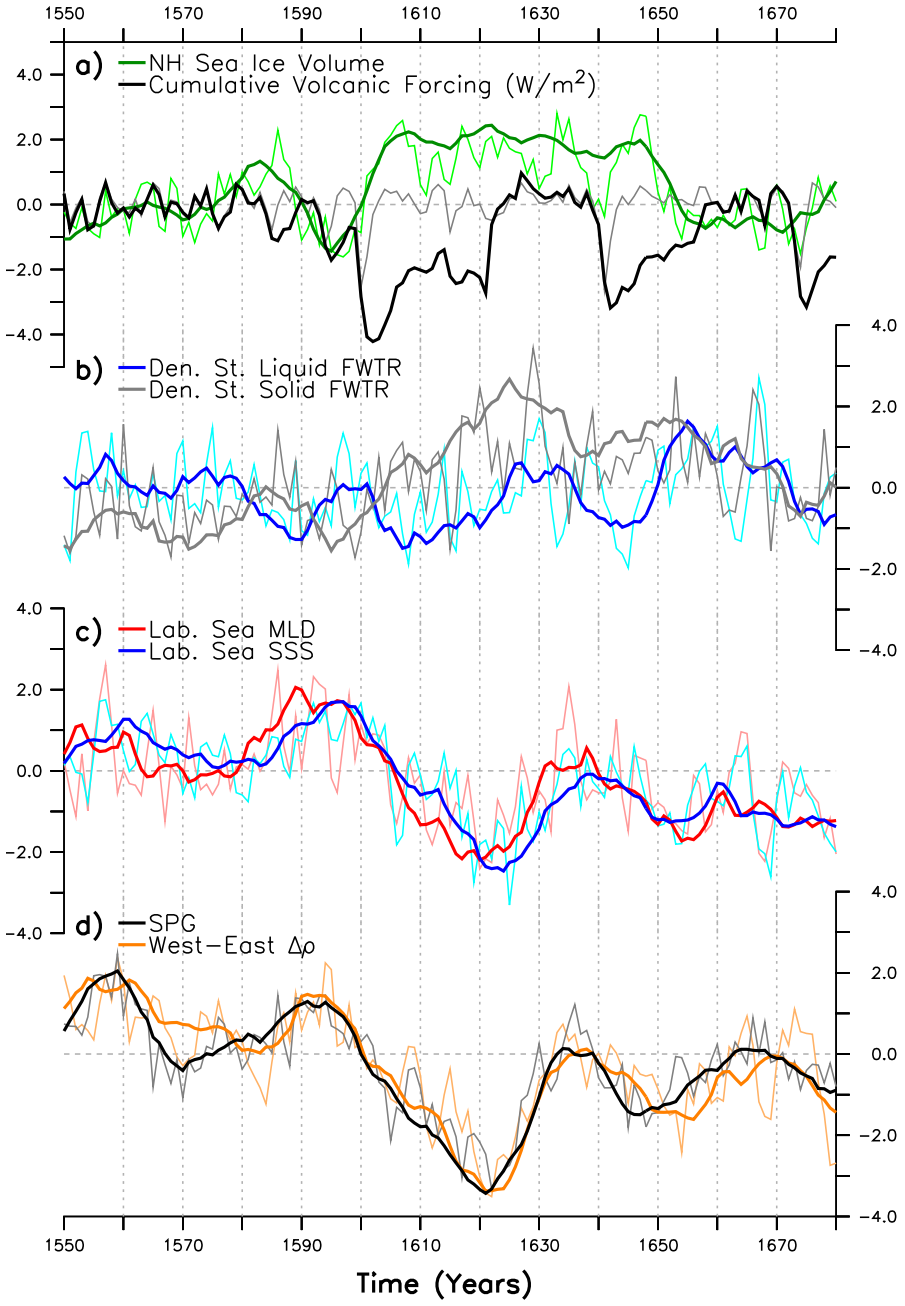

Figure 5.6: Standardized annual anomalies of variables in Past1000-R3 throughout the SPG shift, between 1550 CE and 1680 CE (thin lines), with thick lines as their corresponding 11-year running means. Values in parentheses correspond to the mean ± standard deviation in the last millennium. **(a)** NH sea ice volume (28000±1700 km^3). Also, simulated volcanic forcing (thin line), as in Fig. 5.1b, and accumulated volcanic forcing (thick line), both in W/m^2. **(b)** Liquid and solid components of the FWTR through the Denmark Strait (3192±436 km^3/year and 1115±402 km^3/year respectively). **(c)** March MLD, and SSS in the Labrador Sea, as in Fig. 5.5 (748±273 m and 33.46±0.19 psu respectively). **(d)** SPG strength, and west–east gradient of upper-ocean densities, as in Fig. 5.5 (12.7±1.1 Sv and 0.286±0.076 kg/m^3 respectively).

from the Arctic. Fresher, hence lighter, conditions in the upper Labrador Sea considerably reduce the west–east gradient of upper-ocean densities in the subpolar region (Fig. 5.6d). The SPG thereby weakens by about 5 Sv until a minimum strength of nearly 9 Sv (Fig. 5.6d). Increase in water column stratification due to surface freshening additionally induces a strong reduction in late-winter oceanic convective mixing: minimum values of only 100 m for the mean MLD in the Labrador Sea are found between 1620 CE and 1630 CE (Fig. 5.6c). Deep water formation is thus shut down, leading to substantial AMOC slowdown for about 20–30 years (Fig. 5.5c).

The development of the initial anomalies in the Labrador Sea triggers two positive feedbacks within the SPG that lead to further weakening of the gyre. Firstly, a debilitated SPG transports less heat poleward between 1600 CE and 1620 CE (Fig. 5.5d). As a result, the upper Nordic Seas cool down, inducing anomalously strong sea ice growth in the area. Consequently, sea ice export through the Denmark Strait reinforces (Fig. 5.6b), leading to further salinity drop in the upper Labrador Sea (Fig. 5.6c). Secondly, a weaker SPG also transports less salt toward the western subpolar basin (not shown), thus sustaining the anomalously fresh conditions in the upper Labrador Sea. As a weaker SPG also transports less heat westward, temperatures in the upper Labrador Sea are eventually cold enough to increase upper-ocean densities, despite the haline-driven lightening (from 1620 CE onward, Fig. 5.6d). As upper-ocean density increases, deep water formation progressively resumes, mixing waters from the upper and deeper levels. This process reduces the magnitude of the negative salinity anomaly in the upper Labrador Sea, hence strengthening the gradient of upper ocean densities and the SPG. Yet the recovery of the SPG strength is not complete, as sufficient salinity anomalies remain in the western subpolar basin to keep a weaker SPG regime stable afterward, as discussed in Section 5.4.

5.5.2 Testing the mechanism triggering the shift

Experimental setup

Three ensembles of sensitivity experiments are designed to assess the robustness of the simulated SPG shift under different initial conditions and applied external forcing. The first ensemble focuses on long-term preconditioning and consists of five all-forcing simulations initiated in 1593 CE (hereafter AllFor-1 to 5). This ensemble includes the original Past1000-R3 as AllFor-1. The second ensemble focuses on short-term preconditioning and consists of five all-forcing simulations initiated in 1600 CE (hereafter AllFor-6 to 10). The third ensemble focuses on the role of the volcanic forcing and consists of 10 simulations initiated in 1593 CE in which there is no volcanic forcing for the period 1593–1650 CE (hereafter NoVol-1 to 10). All simulations are initiated in January 1st, and are run until, at least, 1699 CE. Each ensemble member is generated from the original Past1000-R3 (AllFor-1) by inducing an infinitesimal perturbation in the atmospheric vertical diffusivity during the first integration year, except for the first member of the NoVol ensemble. This method for ensemble initialization is a common procedure with MPI-ESM [e.g., Zanchettin et al., 2013], because it produces a rapid divergence of climate trajectories and, therefore, an adequate ensemble spread.

Results

The SPG strength for all simulations is plotted in Figure 5.7, overlying their associated discrete levels. The change in the SPG strength between the two discrete levels in years 1620 CE

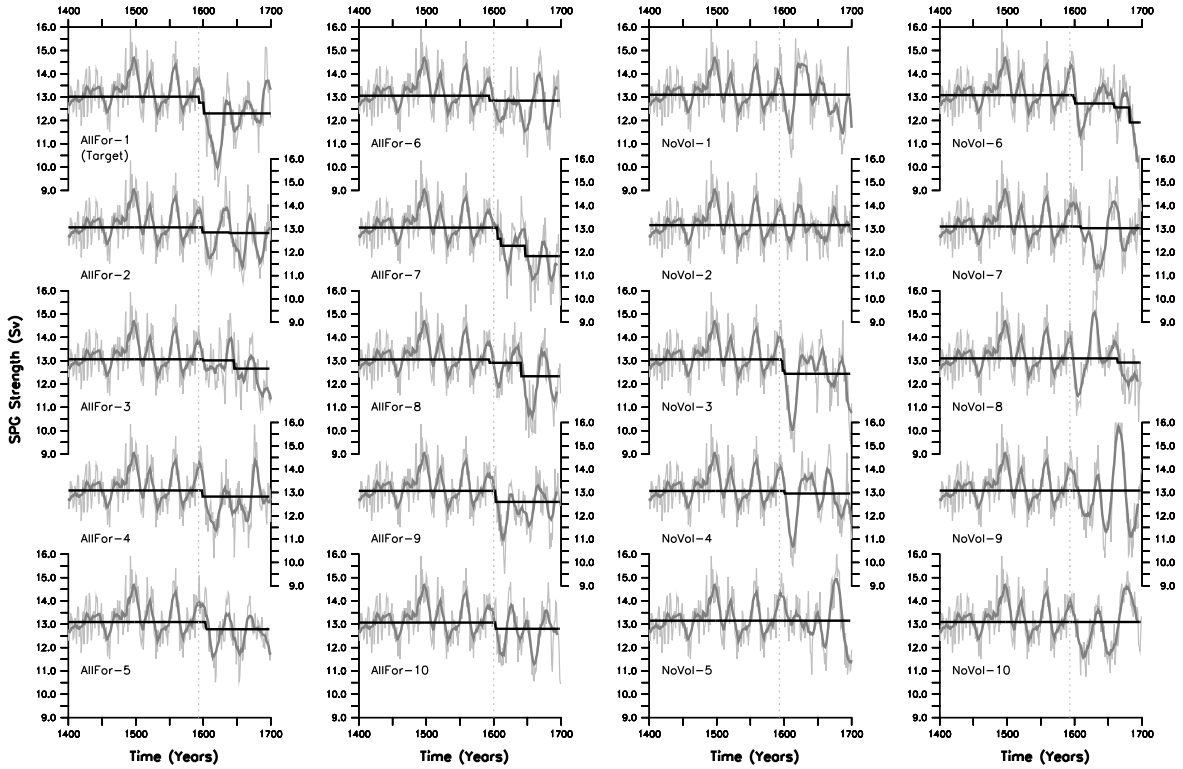

Figure 5.7: SPG strength (in Sv) in the sensitivity experiments, as in Fig. 5.1: thin and solid lines are respectively annual averages and the 11-year running mean. Horizontal solid lines are the discrete levels. Vertical dotted lines indicate the starting year of each integration.

and 1590 CE is additionally shown in Figure 5.8 (along the horizontal axis). The choice of these particular years is arbitrary as levels extend for more than one. Although we are mainly interested in shifts occurring around 1600 CE, as in the target, we also include the delayed shift in AllFor-8 around 1640 CE (Fig. 5.8, asterisk; using discrete levels in years 1640 CE and 1670 CE) because it occurs after a large volcanic eruption (Fig. 5.1b) and exhibits features similar to the target (see below).

The magnitude of the change in the SPG strength after 1600 CE varies widely across the AllFor simulations, ranging between 0.05 and 0.78 Sv (Figs. 5.7 and 5.8). Values are generally larger in the short-term preconditioning ensemble (AllFor-6 to 10), ranging from 0.21 to 0.78 Sv, than in the long-term preconditioning ensemble (AllFor-2 to 5), between 0.05 and 0.31 Sv, except for the 0.72 Sv shift in the target (AllFor-1). Only AllFor-7, AllFor-8, and AllFor-9, which all belong to the short-term preconditioning ensemble, show a SPG shift larger than 50% of the target. The chance of reproducing a shift as strong as the target thus increases in experiments initiated in 1600 CE, presumably because they are initiated closer to the onset of the shift, and their climate trajectories therefore cannot sufficiently diverge. On the other hand, four AllFor simulations show a relatively small reduction in the SPG strength, below 0.25 Sv. The substantial differences found in the SPG evolution across the experiments suggest that the volcanic forcing alone does not suffice to robustly trigger a SPG shift. The volcanic cluster must then occur together with a favorable combination of background climate conditions.

Within the NoVol ensemble, a SPG shift occurs only in NoVol-3 (0.62 Sv) and NoVol-6

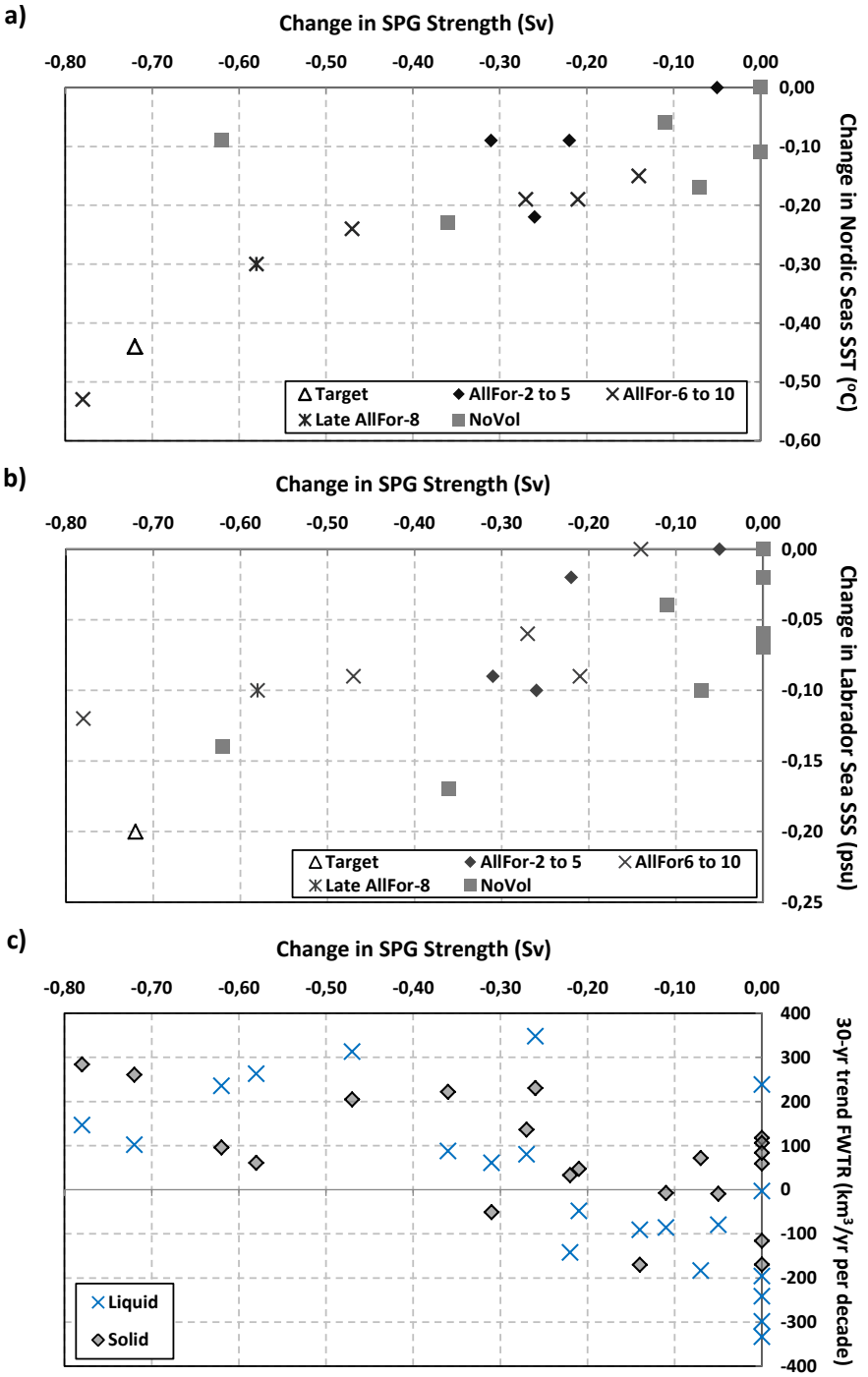

Figure 5.8: Scatter plots for the sensitivity experiments: **(a–b)** Change between the two discrete levels in years 1620 CE and 1590 CE in the Nordic Seas SST (in °C) and Labrador Sea SSS (in psu) against the analogous change in the SPG strength (in Sv). Variables are defined as in Fig. 5.5. **(c)** 30-year trend, between 1600 CE and 1629 CE, in the liquid (crosses) and solid (diamonds) FWTR through the Denmark Strait (in km^3/year per decade) against the change in the SPG strength (in Sv) between discrete levels in years 1620 CE and 1590 CE. The FWTR trend of the later shift in AllFor-8 is calculated between 1640 CE and 1669 CE (asterisk in **a** and **b**), and between 1590 CE and 1619 CE in AllFor-7, since this simulation undergoes a faster increase than the others do (first cross starting from the left in **a** and **b**).

(0.36 Sv). The volcanic forcing is hence not a necessary factor to trigger a shift in the SPG. However, since most of the NoVol experiments show no shift after 1600 CE at all, we can also conclude that, within the limits of our small ensemble size, the volcanic cluster seems to increase the likelihood of the occurrence of a SPG shift.

Discrete levels are also obtained for the Labrador Sea SSS and Nordic Seas SST in the sensitivity experiments, for the same regions as in Figure 5.5 (time series not shown). Their associated changes around the shift plotted against the change in the SPG strength (Fig. 5.8a,b for the SSS and the SST respectively) allow evaluating the magnitude of the changes in the Nordic Seas with respect to those within the subpolar North Atlantic, as well as assessing whether the shift simulated in each experiments involves the entire North Atlantic/Arctic region, as shown to be the case of the target (see Section 5.4). According to Figure 5.8, the larger the change in the SPG strength is, the colder and fresher conditions develop, respectively due to reduced heat and salt transports by the SPG, in the upper Nordic and Labrador seas after the shift. Changes in the SPG strength and Nordic Seas SST appear to follow a non-linear relationship, with an even colder Nordic Seas surface for the strongest SPG shifts. This result might be related to the presence of positive feedbacks between the subpolar North Atlantic and the Nordic Seas involving the upper-ocean temperatures in the Nordic Seas, the sea ice transport through the Denmark Strait, and the SPG strength. Six simulations experience changes in the Labrador and Nordic seas larger than 50% of the target; most simulations exhibit much weaker changes or none at all. Furthermore, only AllFor-7 shows changes in the SPG strength and Nordic Seas SST larger than the target, whereas none of the experiments shows changes in the Labrador Sea SSS larger than the target. The probability of simulating a shift in the North Atlantic climate at least as strong as the target is thus relatively small (10%, or 2 over 20). The North Atlantic climate will most likely experience relatively small transitions even if it is following a trajectory close to those featuring an abrupt and strong shift between two regimes. This could explain why the SPG and, in general, the North Atlantic undergo a smooth transition throughout the past millennium instead of a strong shift in Past1000-R1 and R2 (Fig. 5.1a).

As described before, the target SPG shift in AllFor-1 (Past1000-R3) is driven by anomalous large export of freshwater from the Arctic into the Labrador Sea. This is illustrated by the 30-year trend between 1600 CE and 1629 CE in the total (liquid plus solid) FWTR through the Denmark Strait, of about 360 km^3/year per decade (Fig. 5.8c). Similar trends are also found in the other five simulations featuring the largest SPG shifts (Fig. 5.8c), although these can be due to increases mainly in the solid component –as in the target–, in the liquid one, or in both components simultaneously (Fig. 5.8c). The relative importance of each FWTR contribution remains unclear and can relate, for example, to the region where deep convection preferentially occurs in the model and during the years when the discharge of freshwater occurs. Regardless of the case, and as shown for the target (Fig. 5.6), an increase in the Arctic freshwater export can lead to a broad freshening of the upper Labrador Sea and, in turn, to a substantial, long-lasting SPG weakening, which drives further reduction in the salt transport along its northern rim. All simulated shifts are therefore triggered by an increase in the FWTR, independently of the type of experiment considered.

In those experiments with a small or absent shift, the 30-year trend in the total FWTR varies between approximately ±500 km^3/year per decade (Fig. 5.8c). In some cases, small SPG shifts are even associated with a decrease in one or both components of the FWTR. For similar values of the total FWTR trend, for example between 300 and 450 km^3/year per decade, the change in SPG strength ranges between 0 and 0.78 Sv. This suggests, first, that the SPG is not too

sensitive to the FWTR from the Arctic in our model, and, second, that at least the positive climate feedbacks described before must get activated after the discharge of freshwater in order to trigger a SPG shift.

5.6 Discussion

5.6.1 Attribution of the subpolar gyre changes in the last millennium

The millennial-scale weakening of the SPG strength that develops either smoothly over the past millennium in Past1000-R1 and R2 or abruptly in R3 must be driven by the imposed external forcing throughout this period, because the SPG strength in PiControl does not show any long-term trend (not shown). However, differences across the Past1000s also suggest that any influence of the external forcing is shaped by internal climate variability. In none of the transient simulations, the SPG strength shows significant cross-correlation with the solar or volcanic forcing (Fig. 5.1b for these two forcings; cross-correlation profiles not shown). Also, a clear response to strong volcanic eruptions was found neither in the North Atlantic climate, nor in the SPG strength (Fig. 4.5). This result contrasts with previous studies associating weaker SPG with periods of low solar irradiance [Moffa-Sánchez et al., 2014a] or anomalous (weaker or stronger) SPG to volcanic forcing [Zhong et al., 2011; Zanchettin et al., 2012; Schleussner and Feulner, 2013]. Zanchettin et al. [2013], nevertheless, showed that multiple response pathways to short-lived radiative perturbations like volcanic eruptions can exist, whose activation crucially depends on background climate conditions. By extension, a linear and unique response of the SPG to volcanic eruptions should not necessarily be expected. The simulated long-lasting trend in the SPG strength might also be attributed to varying orbital parameters [Kaufman et al., 2009]. A detailed investigation on the impact of the external forcing on the SPG dynamics at millennial time scales is however beyond the scope of this thesis.

The sensitivity experiments studied in Section 5.5.2 highlighted the role of internal climate variability at the onset of the SPG shift in Past1000-R3, although the volcanic forcing was found increasing the likelihood of occurrence of a SPG shift. These results contrast with previous studies in which similar abrupt events were attributed to the volcanic forcing alone in climate simulations of the past millennium [Miller et al., 2012; Schleussner and Feulner, 2013; Schleussner et al., 2015]. The sensitivity experiments used here, however, still include changes in the other imposed external forcings (see Section 5.5.2), of which only solar activity and volcanic eruptions were found relevant to decadal climate variability [Fernández-Donado et al., 2013]. Nonetheless, were the SPG shift in Past1000-R3 driven by changes in solar activity, rather than by the volcanic forcing, it would have occurred during the maximum around 1600 CE (Fig. 5.1b), in clear opposition to earlier studies associating weaker SPG with solar minima in the past millennium [Moffa-Sánchez et al., 2014a]. It is worth remarking, however, that the late SPG shift found in one of the experiments does not occur during this TSI maximum, but after the Mount Parkers eruption in 1641 CE (All-For-8 in Fig. 5). TSI changes thus seem to be not relevant for the inception of the SPG shift.

5.6.2 The Medieval Climate Anomaly – Little Ice Age transition

Climate changes in the North Atlantic simulated after the shift in the SPG strength and reconstructed during the LIA are indeed in broad agreement. In particular, Copard et al.

[2012], based on the Nd isotopic composition (εNd) of deep-sea corals, concluded that the SPG underwent a transition in the course of the 13th and 14th centuries from an enhanced phase during the MCA to a weak phase during the LIA (Fig. 5.9a). In accordance with such reconstructed SPG weakening, several SST records based on different proxies show a rapid cooling at the beginning of the LIA, for instance, in the Nordic Seas [e.g., Berner et al., 2011] (Fig. 5.9c), off North Iceland [e.g., Sicre et al., 2008; Ran et al., 2011] (Fig. 5.9b), or in the eastern Labrador Sea [Moffa-Sánchez et al., 2014b] (Fig. 5.9e). Other SST reconstructions show, in contrast, warmer conditions during the LIA than during the MCA, for example, in the eastern subpolar North Atlantic [e.g., Miettinen et al., 2012] (Fig. 5.9d) or off northeastern Newfoundland [Sicre et al., 2014]. All these SST reconstructions thus draw a characteristic pattern of cold Nordic and Labrador seas opposed to a warm eastern subpolar North Atlantic and North Atlantic Current that resembles the simulated post-shift SST anomaly pattern (Fig. 5.9h) and that, in the model, results from a broad redistribution in upper-ocean heat content by the SPG alone (see Section 5.4). The simulated reduction in the oceanic meridional HTTR at subpolar latitudes after the SPG shift (Fig. 5.5d) also corresponds well with a reconstructed reduction in the inflow of warm and saline Atlantic waters into the Nordic Seas during the MCA–LIA transition [Dylmer et al., 2013]. Likewise, simulated post-shift cold and fresh upper Labrador Sea conditions (Figs. 5.4 and 5.5) agree with those oceanographic reconstructions in which an increasing influence of the Arctic waters on subpolar latitudes was found [Jensen et al., 2004; Ran et al., 2011; Moffa-Sánchez et al., 2014b] (Fig. 5.9f). Last but not least, simulated expanded sea ice conditions after the SPG shift (Figs. 5.4f and 5.5e) match reconstructed changes in the sea ice-proxy IP25 from the North Icelandic Shelf after 1300 CE [Massé et al., 2008] (Fig. 5.9g), as well as the abrupt increase in ice-cap growth over the Arctic Canada and Iceland [Miller et al., 2012]. Yet, agreement between simulated post-shift anomalies and those reconstructed in the LIA mainly concerns their magnitude and duration, but not their timing of occurrence.

The inception of the simulated and reconstructed anomalies respectively occur in the early 17th century and around the 13th and 14th centuries. Dominance of internal climate variability can nevertheless explain such differences in the timing and, therefore, reconcile reconstructed and simulated variability. Schleussner and Feulner [2013] reported that the onset of the LIA can occur at different times in an ensemble of simulations with the Climber-3α model, which the authors attributed to the sensitivity of the subpolar variability to minor changes in the North Atlantic freshwater budget in their model. They were thus able to simulate an earlier LIA onset (around 1450 CE) in the North Atlantic by forcing the Nordic Seas with a constant freshwater offset. It is unknown whether MPI-ESM-P features a similar sensitivity to the freshwater export from the Arctic, but we argue that an analogous temporal spread in the onset of the shift as in Schleussner and Feulner [2013] can be expected: only when a sufficient amount of freshwater is discharged toward the subpolar North Atlantic under the appropriate climate conditions, a SPG shift can occur. In fact, some temporal spread in the onset of the shift is found in the sensitivity experiments analyzed in Section 5.5.2 after 1600 CE. However, this hypothesis was not tested for a shift before 1593 CE.

In view of these results, could the regime shift described here be regarded as onset of a LIA-like episode in the North Atlantic? To answer this question, we can compare the transient climate evolution of the three Past1000 simulations. Their global and hemispheric mean SAT exhibit similar millennial negative trends and cold excursions in response to the strongest volcanic eruptions, and are similar to the reconstructed ones for this period (Fig. 5.5h, for the NH mean SAT). Compared to Past1000-R1 and R2, the SPG shift in Past1000-R3 therefore

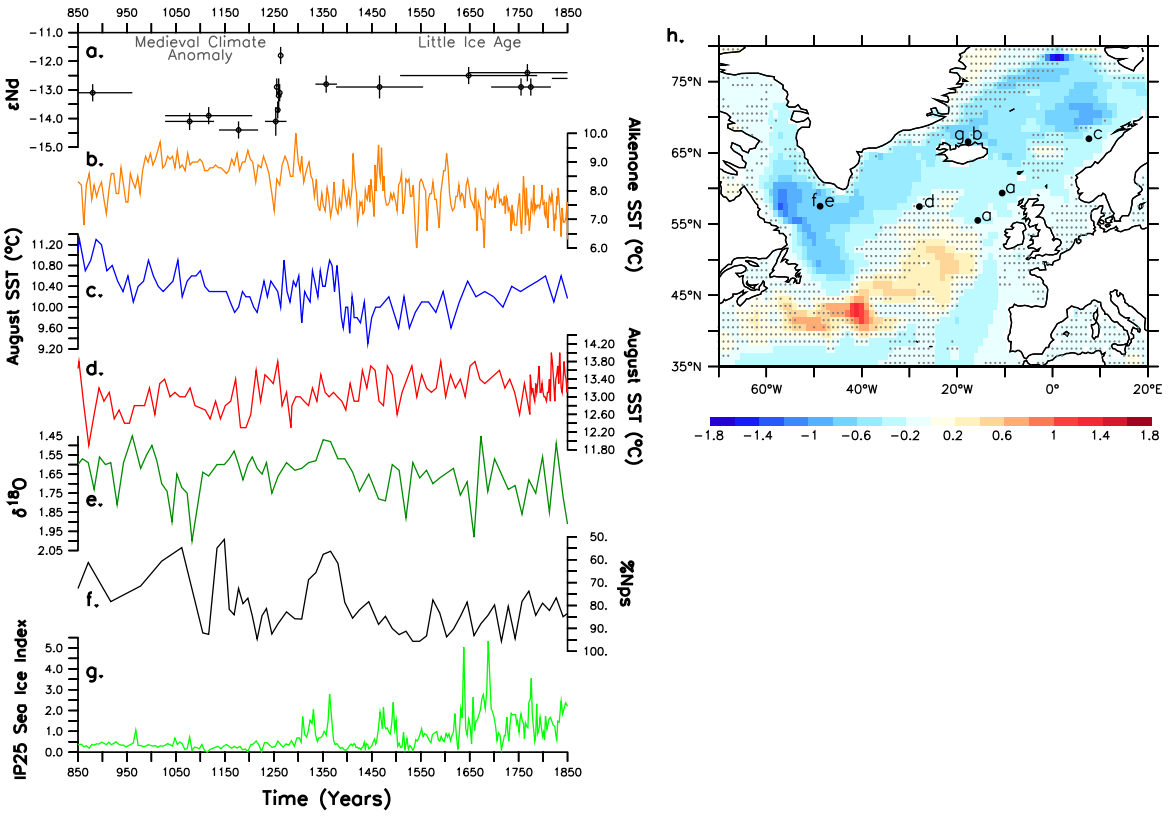

Figure 5.9: Reconstructions of the North Atlantic climate variability in the pre-industrial past millennium: **(a)** εNd values from deep-sea corals in the Rockall Trough [Copard et al., 2012]. **(b)** Alkenone SST reconstruction off North Iceland (in °C) [Sicre et al., 2008]. **(c)** August SST reconstruction from the Vøring Plateau (in °C) [Berner et al., 2011]. **(d)** August SST reconstruction from the Reykjanes Ridge (in °C) [Miettinen et al., 2012]. **(e–f)** Respectively *T. quinqueloba* δ^{18}O and percentage of the polar species *N. paquiderma (sinistral)* (Nps) from the Eirik Drift [Moffa-Sánchez et al., 2014b]. **(g)** IP25 sea ice proxy from off North Iceland [Massé et al., 2008]. **(h)** Simulated after (1650–1749 CE) minus before (1450–1549 CE) SST anomalies, from Fig. 5.4 (in °C; shading, with hatching indicating non-significant anomalies). Locations of the core sites of the reconstructions shown in **(a–g)** are also indicated.

does not shape the global or the hemispheric evolution of the climate throughout the past millennium; rather, climatic changes associated to the shift arise more prominently on regional scales in the North Atlantic/Arctic sector, as discussed in Section 5.4. The pattern of SAT anomalies between the MCA and the LIA in the North Atlantic/Arctic for the three Past1000s are relatively alike (Fig. 5.10). Similarities between Past1000-R3 and R1 or R2 are illustrated by the relatively high spatial correlation coefficient between the corresponding anomaly patterns (numbers in Fig. 5.10a,b). Interestingly, the pattern of MCA–LIA anomalies in Past1000-R3 is mainly explained by climate changes due to the shift in the SPG strength (Fig. 5.10d, and associated spatial correlation coefficient). The three Past1000s therefore present similar cold conditions in the North Atlantic at the end of the pre-industrial period, which we referred to as the LIA. But, while the transition from a relatively warm MCA to a relatively cold LIA develops smoothly in Past1000-R1 and R2, it occurs abruptly in Past1000-R3, in both cases mainly driven by changes in the SPG strength alone. Hence, in our

model world there exits two possible realizations of the climate evolution during the past millennium, so that the actual onset of the LIA described in the reconstructions would then just be another possible realization.

Our dynamical interpretation of the transition toward LIA-type episodes differs from previously suggested mechanisms for other similar abrupt climate transitions in the North Atlantic [Miller et al., 2012; Drijfhout et al., 2013; Lehner et al., 2013; Schleussner and Feulner, 2013; Schleussner et al., 2015]. These modeling studies primarily related the cold climate conditions in the North Atlantic to a slowdown of the meridional heat transport by the AMOC, in agreement with records describing a weak AMOC during the LIA [Lund et al., 2006; Wanamaker et al., 2012]. This hypothesis, nonetheless, contrasts with a recently proposed index for the AMOC strength over the past millennium in which no weakening was reconstructed before the 20th century [Rahmstorf et al., 2015], more in accordance with our

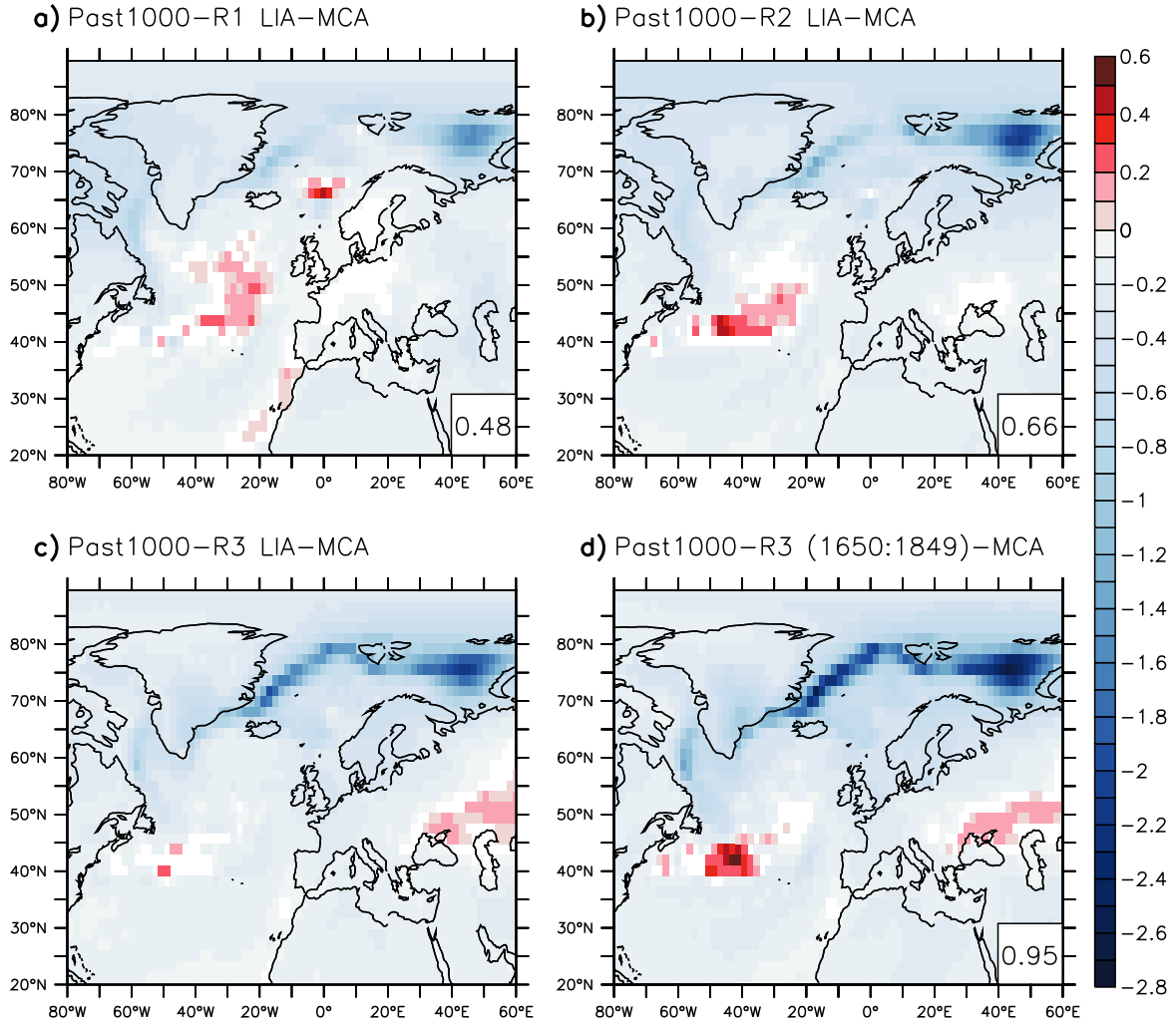

Figure 5.10: SAT anomalies (in °C) of the LIA (1450–1849) with respect to the MCA (950–1250) in **(a)** Past1000-R1, **(b)** Past1000-R2, and **(c)** and Past1000-R3. **d)** SAT anomalies between the last two centuries of the LIA after the SPG shift (i.e., 1650–1849) with respect to the MCA in Past1000-R3. Only anomalies that exceed the 95% confidence level with a two-sided *t* test in PiControl are shown. Spatial correlation coefficients between patterns in **(a)**, **(b)**, or **(d)**, and the one in **(c)** are also respectively shown.

study. A particular case that here deserves special mention is the climate regime shift in the North Atlantic at the onset of the LIA described in climate simulations with the model CLIMBER-3α [Schleussner and Feulner, 2013]. The proposed mechanism included a volcanically forced sea ice expansion in the Nordic Seas, leading to a decrease in the local deep water formation and, thereby, in the overflow through the Greenland–Scotland Ridge. The latter resulted both in a baroclinic spin-up of the SPG due to increasing re-circulation of subtropical water into the subpolar region, and in a LIA-like basin-wide cooling due to weakened heat transport by the AMOC. Although their results were found in agreement with SST reconstructions from the Nordic Seas and the eastern subpolar North Atlantic [Schleussner et al., 2015, the SST reconstructions are also shown here in Fig. 5.9c,d], the simulated SPG spin-up in CLIMBER-3α differs from reconstructed evidence of a weaker SPG during the LIA [e.g., Copard et al., 2012; Moffa-Sánchez et al., 2014b]. In addition, whereas the SPG shift in CLIMBER-3α appears as a transition from one stable circulation regime into another unconditionally stable mode, the shift in our model (MPI-ESM-P) can rather be regarded as a modulation of a continuous succession of rapid transition, with similar ranges of variability before and after the shift. The reasons of the different behaviors of the SPG simulated by these two models are unclear. One possible explanation concerns the models' different complexity generating different dominant mechanisms, as shown, for instance, in the case of the bistability of SPG regimes in the multi-model investigation by [Born et al., 2013].

Copard et al. [2012] in turn associated the SPG weakening in their reconstructions with a shift between different NAO phases during the MCA–LIA transition [Trouet et al., 2009]. Ortega et al. [2015], however, proposed a new NAO index for the past millennium in which such a transition is not found, more in agreement with our results for the NAO as well as previous modeling studies [e.g., Lehner et al., 2013; Gómez-Navarro and Zorita, 2013]. All in all, the latest evidence hence suggests that cold conditions reconstructed in the North Atlantic during the LIA were driven neither by an AMOC slowdown, nor by a shift between NAO phases, but by a weakening of the SPG strength and associated meridional heat transport.

5.7 Conclusions

We investigated the decadal to multicentennial SPG variability and underlying mechanisms in an ensemble of three climate simulations (Past1000s) covering the last millennium and conducted with the MPI-ESM-P model. In particular, we described an abrupt shift in the SPG strength detected in one ensemble member around 1600 CE that separates two different regimes of the North Atlantic climate, the later one featuring LIA-characteristics. We also explored the mechanism that renders the later regime stable for at least 250 years as well as the trigger of the SPG shift. Our results were supported by sensitivity experiments in which the initial conditions are slightly modified and/or the volcanic forcing removed. Results indicate that:

1. A millennial-scale weakening of the SPG strength throughout the past millennium is robustly simulated in the three Past1000s; this can be relatively smooth, through a long-term trend, or abrupt, through a decadal-scale shift.

2. The climate regime simulated after the SPG shift is stable on multicentennial time scales due to long-lasting anomalies within the North Atlantic: relatively fresh conditions in the upper Labrador Sea, weak oceanic meridional heat transport in the subpolar North

Atlantic, expanded sea ice in the Labrador and Nordic seas, and persistent blocking-like SLP anomalies over the subpolar North Atlantic. Simulated post-shift climatic anomalies thus resemble reconstructed changes in the area during the LIA, except for the timing of the occurrence. The simulated SPG shift is not associated with a shift in the AMOC strength or phase of the NAO. This dynamical interpretation of the post-shift North Atlantic climate anomalies is, in addition, supported by the analysis of the leading modes of variability of the North Atlantic barotropic streamfunction above decadal time scales. These results describe therefore a new possible mechanism for the onset of LIA-type episodes in the North Atlantic driven by SPG changes alone.

3. The SPG shift is triggered by anomalously large freshwater export from the Arctic and can mainly be attributed to internal climate variability. Volcanic forcing, also in the form of a cluster of small-magnitude volcanic eruptions, can facilitate the inception of the SPG shift, but is not a necessary condition. This highlights the relevance of internal climate variability with respect to externally forced changes in order to explain the evolution of the North Atlantic climate throughout the past millennium.

Chapter 6

A subpolar gyre-driven European Little Ice Age

Climate reconstructions depict a much colder LIA (ca. 1450–1850 CE) over Northern Europe than over the South, and in winter than in summer. We propose a set of mechanisms to explain such regional and seasonal features using an ensemble of three climate simulations of the past millennium that show high temporal and spatial agreement with these reconstructions. The simulated coldest centuries during the LIA (mid 16th to early 18th) are related to a multicentennial weakening of the SPG strength and associated northward heat transport that lead to persistent upper-ocean cooling, expanded sea ice, and reduced winter heat losses in the Nordic and Barents seas. The latter in turn induces high pressure anomalies in winter over much of the North Atlantic and Northern Europe, where, in addition, the frequency of atmospheric blocking events increases, as recorded during these centuries. The associated change in wintertime atmospheric circulation contributes to amplifying the continental cooling by advecting polar air masses southward toward Central Europe, while drastically reducing the influence of the westerlies. This mechanism, however, does not operate during LIA summers, when European cold conditions instead stem from an externally forced radiative cooling of the Earth's surface. Neither of these mechanisms is related to changes in the AMOC or NAO. Sensitivity experiments further suggest that the solar forcing alone cannot trigger a LIA-like episode, although the Maunder solar minimum could be necessary to deepen and lengthen it into the 18th century.

6.1 Introduction

The LIA is commonly identified in global and hemispheric climate reconstructions as a period of relatively cold conditions between the 15th and 19th centuries [Masson-Delmotte et al., 2013]. Continental-scale temperature reconstructions, however, differ both in the timing of its onset as well as in the magnitude and spatial extent of its related cold anomalies [Pages 2k Consortium, 2013]. Over Europe, in particular, the LIA cooling seems to have started around 1200–1300 CE and reached the coldest temperatures around 1600–1700 CE [Pages 2k Consortium, 2013; Luterbacher et al., 2016], with colder conditions over Northern and Central Europe than over the Mediterranean region [Luterbacher et al., 2004, hereafter LUT04]. Most of these reconstructions are, nonetheless, restricted to the summer season (JJA) constrained by the proxies used (mostly tree rings, as in Pages 2k Consortium [2013] and references therein). The few reconstructions that cover both the summer and winter (DJF) seasons show much colder European temperatures in winter than in summer throughout the LIA [LUT04; Dobrovolnỳ et al., 2010], especially over Central Europe and Scandinavia. Documentary evidence also reports colder and longer winters during the LIA than in the previous and following centuries, associated with more frequent, persistent, and severe cold spells and blocking anticyclones [Behringer et al., 2005]. Yet in summer, reports and climate reconstructions rather show fluctuations from extremely hot to much colder periods, and vice versa [e.g., Behringer et al., 2005; Glaser and Riemann, 2009]. The reason of such seasonal discrepancies in the climate during the LIA is, however, not fully understood yet, nor whether they are related to different underlying mechanisms. This Chapter aims to give an answer to these questions.

A variety of mechanisms has been proposed to explain the onset of the LIA and its reconstructed features, yet generally with contradictory evidence. Lehner et al. [2013], and before them, Miller et al. [2012], simulated the cold conditions in the North Atlantic and Europe during the 14th and 15th centuries in response to an externally forced Arctic sea ice expansion and a reduction of the AMOC strength and its associated northward heat transport. In response to such anomalies, Lehner et al. [2013] also described a development of high pressure anomalies over the Barents Sea that could have contributed to cooling Northern Europe in summer and, especially, winter. However, whereas Lehner et al. [2013] attributed the LIA onset mainly to the solar minima before 1500 CE, in climate simulation using a high-amplitude solar forcing reconstruction [Crowley, 2000], Miller et al. [2012] did so invoking decadally paced, strong volcanic eruptions during the 13th century. Further uncertainty relates to the timing of the European LIA onset itself, for these two theories were proposed for the 13th and 14th centuries, not for the following and indeed colder 16th through 18th centuries. Schleussner and Feulner [2013] in turn attributed the European LIA cooling to a volcanically forced reduction in the oceanic heat transport by the AMOC in simulations with an intermediate complexity model. The proposed mechanism involved an abrupt spin-up of the SPG that, nonetheless, disagrees with evidence of a weak gyre during the LIA [e.g., Copard et al., 2012; Miettinen et al., 2012; Moffa-Sánchez et al., 2014b]. On the other hand, efforts to reconstruct past changes in the North Atlantic circulation have not provided yet a conclusive answer as to whether the AMOC and, hence, its associated heat transport were actually weaker during the LIA [e.g., Lund et al., 2006; Wanamaker et al., 2012; Rahmstorf et al., 2015]. Other studies invoked a shift in the NAO toward more negative phases to explain European cold conditions during the LIA [Trouet et al., 2009], although this has not been supported by following modeling studies [e.g., Palastanga et al., 2011; Lehner et al., 2012; Gómez-Navarro

and Zorita, 2013] and a newer NAO reconstruction [Ortega et al., 2015].

In the previous Chapter of this thesis we proposed, based on Earth-system-model simulations and climate reconstructions for the past millennium, that LIA-type events in the North Atlantic can be triggered by a weakening of the SPG strength alone; however, we did not address how and to what extent this event can explain the reconstructed cold conditions over Europe during the LIA. This Chapter thus intends to explore mechanisms of decadal to multicentennial variability in the continental-scale European temperature in our ensemble of three past millennium coupled climate simulation (see Chapter 2 for further detail). In particular, we investigate the role of the SPG-related heat transport in the cold climate conditions reconstructed over Europe during the LIA between the late 16th and 18th centuries, focusing on summer–winter differences. This Chapter therefore seeks to answer the following questions: What are the mechanisms driving the cool temperatures over Europe during the LIA? Do they differ between winter and summer? What is the relative contribution of the SPG and of the AMOC, and their associated heat transports during this period? As for the role of atmospheric variability: are these climate changes related to a specific anomalous phase of the NAO? Or to more frequent blocking situations?

6.2 Reconstructed and simulated European temperatures in the past millennium

The Pages2k project represents one of the most recent and comprehensive efforts to reconstruct temperature changes in Europe during the Common Era [Pages 2k Consortium, 2013; Luterbacher et al., 2016]. The Pages2k reconstruction (Fig. 6.1a, upper panel) provides annually resolved continental-scale temperatures for the summer season (JJA) of the European region between 35°N–70°N and 10°W–40°E (hereafter, European Mean Temperature, or EMT). The reconstructed summer EMT features a long-term cooling between the relatively warm 9th to 13th centuries—the Medieval Climate Anomaly—and the colder 17th and 18th centuries—the LIA, shading in Fig. 6.1a—, followed by a faster warming during the industrial era. In addition to these trends, the Pages2k reconstruction shows decadal-scale cold excursions associated with some of the strongest volcanic eruptions (Fig. 6.1b): for example, the Kuwae eruption in 1450 CE, or that of Mount Tambora in 1809 CE. Such reconstructed features on decadal and longer times scales are relatively well reproduced by SATs in the three Past1000s, and especially by Past1000-R2, as illustrated by their correlation coefficients for the periods 850–2003 CE and 1500–2003 CE (Table 6.1a; the latter period is chosen to allow for comparison with LUT04's winter reconstruction). It is worth noting that the reconstructed relative minimum around 1600 CE is also well captured by the Past1000 ensemble, in contrast to other climate model simulations [Luterbacher et al., 2016], although the reconstructed minimum around 1100 CE finds no analogue in the Past1000s, like in those simulations. For the period of interest during the coldest phase of the LIA in the 17th and 18th centuries, however, model–data show robust co-variation. Correlation coefficients among the Past1000's summer EMTs are in turn comparable to those between each simulation and the Pages2k reconstruction for both periods (Table 6.1a). Therefore, and in terms of intra-model agreement above decadal timescales, the Pages2k reconstruction would be equivalent to an additional Past1000 realization.

For comparison, we calculate the EMT for the winter season (DJF) by spatially averaging the gridded field of European temperatures from LUT04 over the same area as for summer

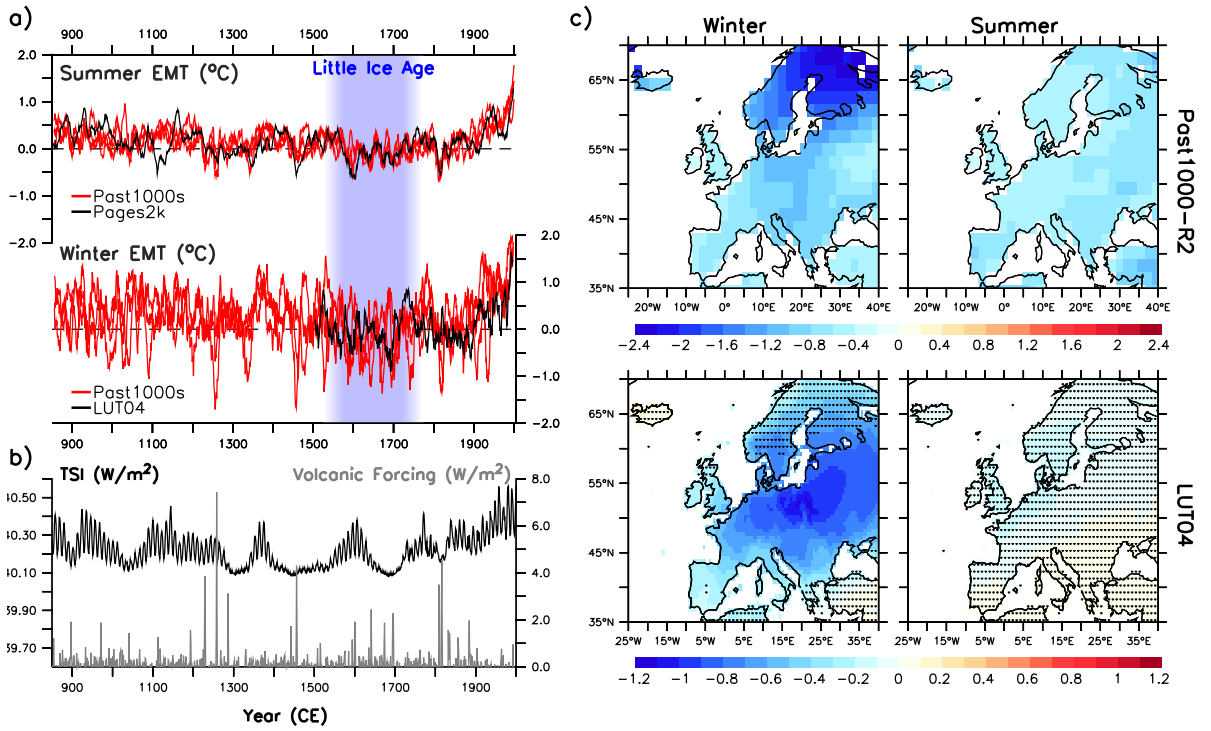

Figure 6.1: **(a)** European mean temperature (EMT) anomalies (in °C; with respect to the period 1500–1849 CE) in summer (upper panel) and winter (lower panel) in the Past1000s (red lines) and for the Pages2k and LUT04's reconstructions (black lines). EMTs are calculated as the spatial average between 10°W–40°E and 35°N–70°N, further smoothed with an 11-year running mean. **(b)** Solar and volcanic forcings in Past1000-R2 (see Fig. 2.1 for a more detailed description). **(c)** Spatial distribution of land temperature anomalies (in °C; with respect to the period 1901–1995 CE) for the period 1575–1724 CE (shading in **a**) simulated in Past1000-R2 (upper panels) and reconstructed in LUT04 (lower panels), in winter (left panels) and summer (right panels). Hatching masks statistically non-significant anomalies above the 95% level, based on the likelihood of occurrence of the signal in PiControl for the simulated anomalies, and on a two-sided *t* test for the reconstructed ones.

(Fig. 6.1a, lower panel). This reconstruction, however, extends back only until 1500 CE. Note that the EMT calculated from the summer temperature field from LUT04 compares well with the Pages2k reconstruction summer EMT (not shown). Similarly as for the summer season, the reconstructed winter EMT shows persistent relatively cold anomalies during the 16th and 17th centuries, and a warming trend in the past two centuries, although the amplitude of the winter anomalies is up to approximately twice that of the summer anomalies during the LIA (compare both panels in Fig. 6.1a). Unlike in summer, agreement between the reconstruction and the Past1000s as well as between the Past1000s themselves is relatively low, with mostly statistically non-significant correlation coefficients for the period 1500–2003 CE (Table 6.1b); values between the reconstruction and the simulations are, nonetheless, within the intra-model agreement range, as they are larger than those between Past1000-R3 and R2 (Table 6.1b). In addition to this, not all simulated winter EMTs feature a similar degree of cooling after the same volcanic eruptions, as for example after the one in 1250 CE, in contrast to the summer season. Internal climate variability therefore contributes more prominently to shaping EMT changes in winter than in summer.

a) Summer

	Pages2k	R1	R2	R3	
Pages2k		0.70	0.76	0.66	1500-2003
R1	0.48		0.75	0.76	
R2	0.52	0.61		0.69	
R3	0.47	0.59	0.58		
	850-2003				

b) Winter

	LUT04	R1	R2	R3	
LUT04		0.35*	0.38*	0.10*	1500-2003
R1	-		0.47	0.46	
R2	-	0.39		0.20*	
R3	-	0.29	0.16*		
	850-2003				

	Pages2k	R1	R2	R3	
Pages2k		0.0079	0.0010	0.0071	1500-2003
R1	0.0058		0.0018	0.0027	
R2	0.0032	0.00016		0.0058	
R3	0.0032	0.000044	0.00015		
	850-2003				

	LUT04	R1	R2	R3	
LUT04		0.084	0.095	0.56	1500-2003
R1	-		0.031	0.0054	
R2	-	0.0034		0.30	
R3	-	0.0068	0.11		
	850-2003				

Table 6.1: Correlation coefficients (upper panels) and p-values (lower panels) between reconstructed and simulated EMTs in **(a)** summer and **(b)** winter, for the periods 850–2003 CE (yellow panels below diagonal) and 1500–2003 CE (gray panels above diagonal). Asterisks denote statistically non-significant values for p>0.05. P-values are calculated accounting for effective degrees of freedom in the time series. EMTs are shown in Fig. 6.1a.

The latter argument can be supported by comparing the reconstructed and simulated EMTs with their corresponding NH mean temperature in summer and winter above decadal time scales. In the reconstructions (Fig. 6.2b), the summer EMT falls well within the maximum values of agreement between NH temperature reconstructions (darkest gray shading in Fig. 6.2b), whereas winter EMT changes are in general larger than the range of NH temperature reconstructions. In the simulations, the difference (residuals) between the EMT and the NH mean temperature is almost flat in both seasons for both the pre- and industrial periods (Fig. 6.2a, for Past1000-R2), although residuals in winter still exhibit mostly negative values during the LIA. Reconstructed and simulated excursions in the NH mean temperature that can mainly be attributed to external forcing factors, such as those after a volcanic eruption, the LIA cooling from the 16th to 18th centuries, or the 20th-century warming [Fernández-Donado et al., 2013], are thus of similar magnitude and timing in the corresponding summer EMT; the latter's variability above decadal time scales is therefore mainly attributed to externally forced changes in the Earth's energy balance. Winter EMT variability is, by contrast, strongly influenced by regional, internal climate changes associated with the European region. This result is key to understand the seasonal differences in the European LIA cooling (see Section 6.4).

Spatially, the period of relatively cold conditions between the late 16th and the beginning of the 18th centuries that is simulated and reconstructed in the EMTs is associated with an anomaly pattern of much colder anomalies in winter, especially over Scandinavia and Central Europe, than in summer, when anomalies are more homogeneously distributed over the Continent (Fig. 6.1c). Simulated changes therefore agree with documentary records of more severe and longer winters during the LIA than during the preceding and following periods over Northern and Central Europe [e.g., Koslowski and Glaser, 1999; Leijonhufvud et al., 2010; Schmelzer and Holfort, 2011; De Jong et al., 2013]. Seasonal differences in the amplitude and spatial extent of the cold anomalies over Europe during the LIA point to different underlying mechanisms for each season, in a way that, in winter, they act toward regionally amplifying such cooling toward the North. It is worth noting, however, that the magnitude of the simulated anomalies is larger than in the LUT04's reconstructions. Such differences might be

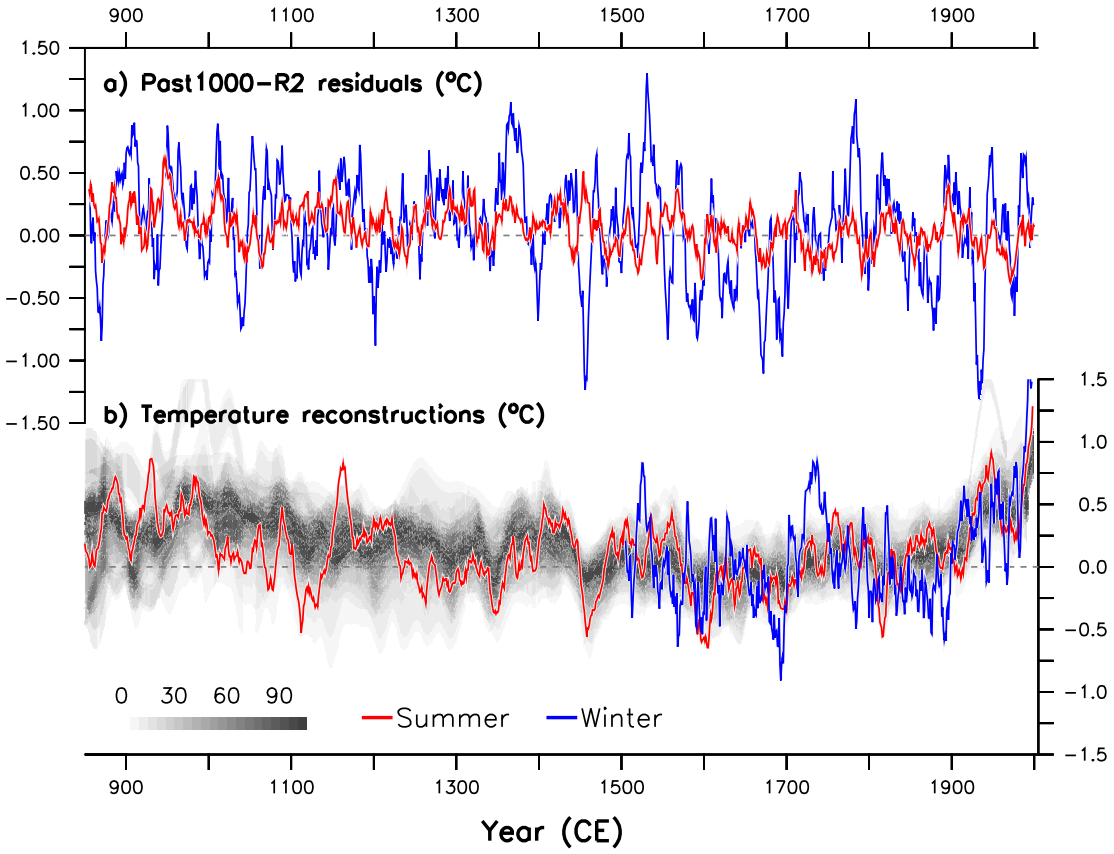

Figure 6.2: **(a)** In Past1000-R2, residuals (in °C) of the EMT, as in Fig. 6.1a, with respect to the NH mean SAT, in winter and summer (blue and red lines respectively), with respect to the mean for period 1500–1849 CE and smoothed with an 11-year running mean. **(b)** Reconstructed EMT anomalies (in °C, as in Fig. 6.1a) in winter and summer (blue and red lines respectively). Also, overlap of NH temperature reconstructions (in percent; shading), as in Fig. 1.1.

consequence of the methodology employed to compute reconstruction fields, as it tends to underestimate the low-frequency variability [e.g., Supplementary Material in Luterbacher et al., 2016]. Support for the magnitude of the simulated LIA cooling is found, for example, in the reconstructed temperatures of Stockholm [Leijonhufvud et al., 2010] and Tallinn [Tarand and Nordli, 2001] for the past 500 years [Leijonhufvud et al., 2010], which show a winter/spring cold anomaly closer to the one simulated in Past1000-R2 than to the one reconstructed in LUT04 (–1.32 °C, –1.31 °C, and –0.69 °C respectively for Stockholm, and –1.48 °C, –1.42 °C, and –0.82 °C respectively for Tallinn, all for the period 1575–1724 CE with respect to 1901–1995 CE). Thus, and given the relatively good agreement between the simulated and the reconstructed European temperature anomalies during the LIA, we explore in the following the possible mechanisms behind the climate changes reconstructed during the LIA over Europe in our model, in particular in Past1000-R2. The results can, nevertheless, be extended to the other two Past1000s, implying that the general mechanism described below is active in all realizations.

6.3 Linking the European mean temperature and the northward oceanic heat transport in the past millennium

This Section describes the impact of the northward oceanic heat transport through the Iceland–Scotland Ridge (ISR HTTR) on the European winter and summer climate on decadal and longer time scales, as well as the main driving mechanisms of the ISR HTTR variability. The analysis is restricted to the pre-industrial past millennium for an assessment of the natural climate variability alone. In winter the ISR HTTR explains about 40% ($p<0.05$) of the EMT variability at these times scales, but only about 21% ($p<0.05$) in summer (Fig. 6.3). Similarly as for the EMT, the ISR HTTR exhibits larger variability in winter than in summer. Changes in the winter ISR HTTR are associated with absolute SAT anomalies of about 1 °C over the Scandinavian Peninsula, and of about 0.5 °C in Central and Eastern Europe (Fig. 6.4a, per ISR HTTR standard deviation unit, or stdv). This pattern resembles well the one of winter temperature anomalies over Europe (Fig. 6.1c) and in the North Atlantic during the LIA (not shown, but similar to Fig. 6.6c). In summer, by contrast, regression coefficients of the SAT onto the ISR HTTR do not exceed 0.3 °C/stdv over the entire European continent. The influence that the ISR HTTR exerts on the European temperature variability on decadal and longer time scales is therefore stronger in winter than in summer.

The largest absolute SAT anomaly associated with ISR HTTR changes is located over the Barents and western Nordic seas for both season, where values can reach up to 3.5 °C/stdv in winter, but do not exceed 0.9 °C/stdv in summer. Here, differences across seasons are related to the atmospheric response to changes in sea ice and surface heat fluxes. In winter the temperature difference between the atmosphere and ocean surface is much larger than in summer, with the atmosphere primarily warmed by the underlying and warmer ocean. A decrease in upper-ocean heat content and temperature driven by a weaker ISR HTTR thus induces an extensive sea ice advancement (Fig. 6.4b, shading) that in turn reduces the ocean surface heat flux to the atmosphere (Fig. 6.4b, contours) and, by extension, cools the atmosphere aloft (Fig. 6.4a, shading), and vice versa; as ultimate consequence, a decrease in ISR HTTR leads to a local development of positive SLP anomalies over the Barents and Nordic seas [Hoskins and Karoly, 1981] that can extend farther south and west over the Scandinavian Peninsula and the subpolar North Atlantic, with a maximum absolute value above 80 Pa/stdv over Iceland (Fig. 6.4a, contours). During the summer season, sea ice changes due to ISR HTTR variations are of lesser magnitude and do not induce major changes in both the ocean heat flux and SAT in the Barents and Nordic seas (Fig. 6.4a,b); in addition, only small and mostly statistically non-significant changes in the SLP are associated with the ISR HTTR variability in summer. Therefore, the larger influence that the ISR HTTR exerts on the European temperatures in winter, compared to summer, relates to a widespread change in the atmospheric circulation over parts of the North Atlantic and Europe that brings colder air masses from the Barents Sea and Arctic into the Continent. This mechanism will allow explaining the seasonal differences in the European temperature anomalies during the LIA (Section 6.4).

In the following, we discuss the relative role of the NAO, the AMOC, and the SPG (indices in Fig. 6.5) in driving the ISR HTTR and, hence, the European temperature variability on decadal and longer time scales over the past millennium. Although the pattern of winter SLP anomalies associated with ISR HTTR changes resembles the NAO (see for example Fig. 1.4), the latter explains only a 11% ($p<0.05$) of the ISR HTTR variability above decadal time scales

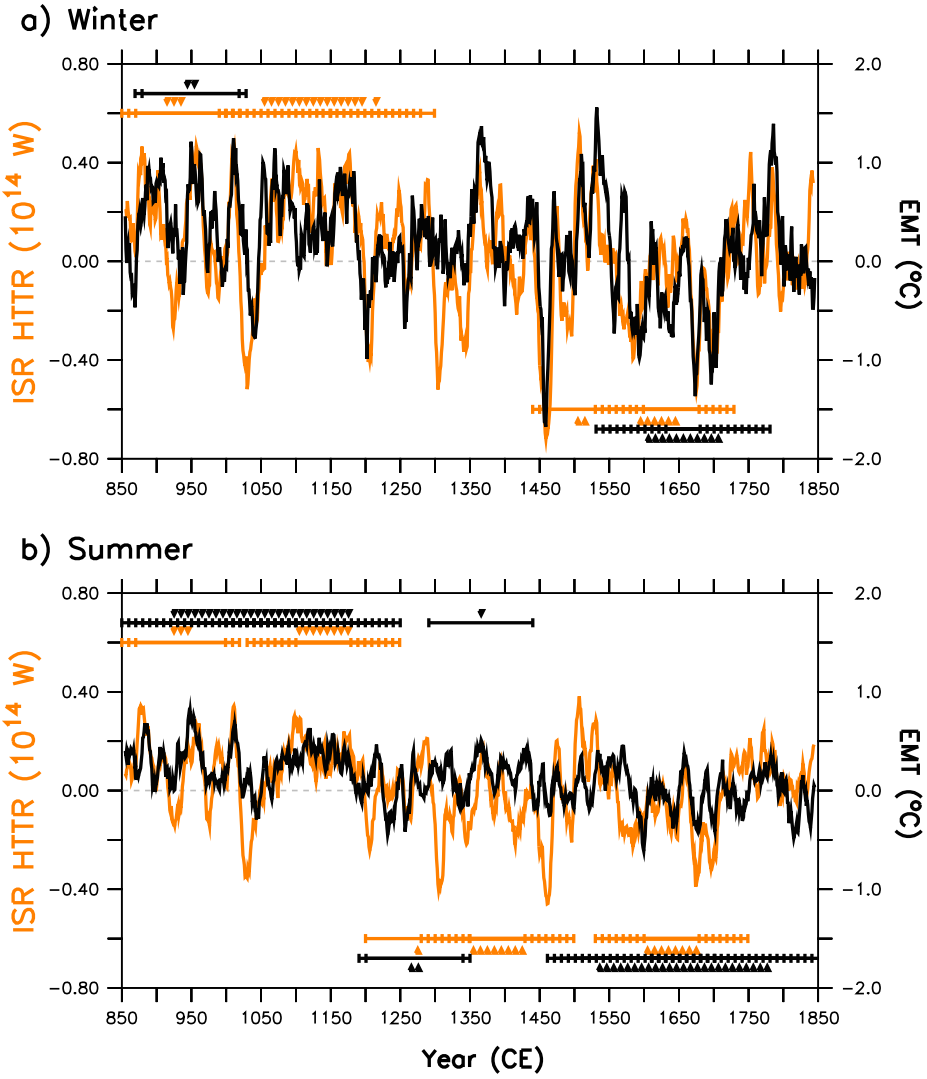

Figure 6.3: In Past1000-R2, anomalies in the ISR HTTR (in 10^{14} W) and the EMT (in °C; as in Fig. 6.1) in **(a)** winter and **(b)** summer, both with respect to the period 1500–1849 CE and smoothed with an 11-year running mean. Note the same vertical axes for both panels/seasons. Horizontal bars above (or below) the time series enclose 150-year periods (marked by tick marks, with the central year marked by a triangle) with positive (or negative) mean values outside the 5th–95th percentiles from a distribution of 150-year-long means in PiControl.

at zero lag (NAO index in Fig. 6.5c); any link between them is however restricted to winter, since their correlation is statistically non-significant in summer (not shown). AMOC changes (Fig. 6.5b), on the other hand, explain about 25% ($p<0.05$) of the ISR HTTR variability in both considered seasons at these time scales, although HTTR fluctuations lead by 2–3 years those in the AMOC. Similar values are found between the AMOC and the SPG at a similar lag (not shown), thus suggesting that it is indeed the SPG which, in general, shapes AMOC variability through heat and salt transport into regions of deep water formation. In turn, changes in the strength of the SPG (Fig. 6.5a) explain about 45% ($p<0.05$) of the ISR HTTR variability both in winter and summer (at zero lag and leading by 3 years respectively). The SPG thus stands as the main driver of the heat inflow into the Nordic Seas and Arctic Ocean and, by extension, of the European winter temperatures above decadal timescales.

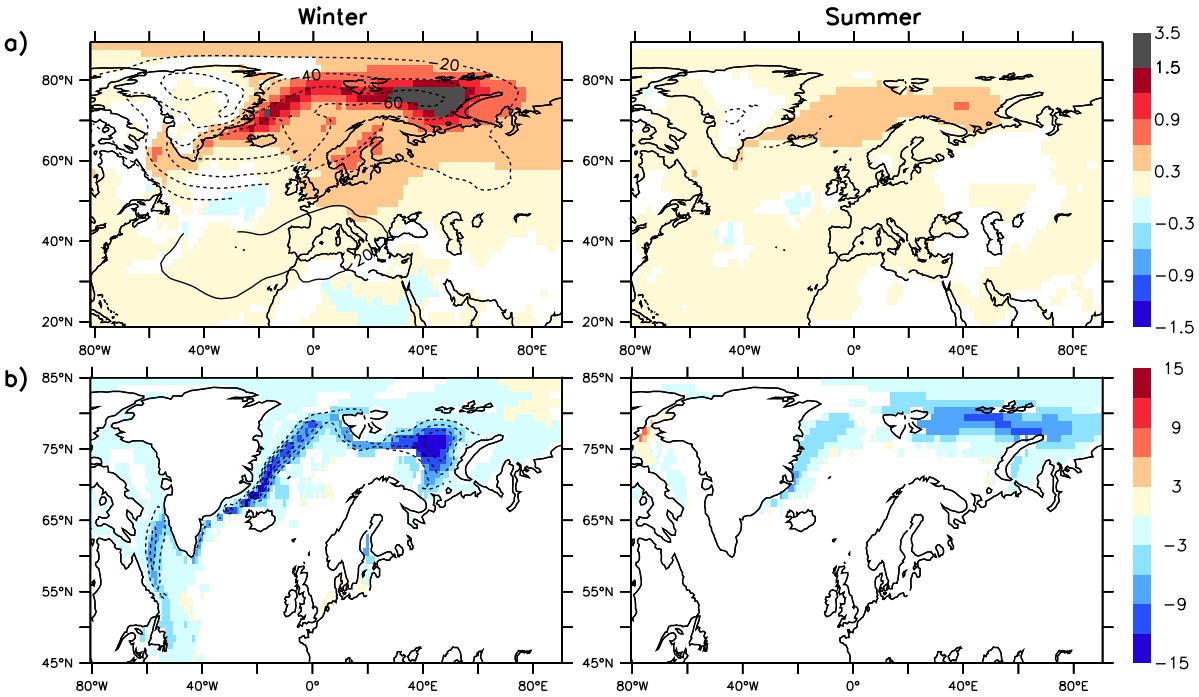

Figure 6.4: In Past1000-R2, regression coefficients of the **(a)** SAT (shading, in °C) and SLP (contours at 20-Pa intervals), and of the **(b)** sea ice concentration (shading, in percent of area) and ocean surface downward heat flux (contours at 10-W/m^2 intervals) onto the standardized ISR HTTR in winter (left panels) and summer (right panels). Sea ice concentration is for late-winter (March) and late-summer (September). Note the same color scale for both panels in **(a)** and **(b)**, which is also adapted for a better view of values over Europe. Only statistically significant values above the 95% level are shown based on two-sided t test in the PiControl climatology. Calculations are performed after applying an 11-year running mean and for the period 850–1849 CE.

6.4 Behind the seasonal features of the European Little Ice Age

In addition to the general good agreement over the past millennium between the EMT and the ISR HTTR above decadal timescales, all series show a period of statistically significant negative anomalies between ca. 1550 CE and 1750 CE for the winter and summer seasons (Fig. 6.3). Accordingly, the SPG also presents a period of consistent relatively weak strength (Fig. 6.5a) that is primarily related to a reduction of the barotropic streamfunction along the North Atlantic Current (Fig. 6.6a). The LIA cooling therefore occurs associated with a multicentennial reduction in the SPG-driven heat transport into the Nordic Seas and Arctic Ocean. By contrast, a persistent AMOC slowdown strength (Figs. 6.5b and 6.6b) is not found during the LIA, nor a shift between NAO phases (Fig. 6.5c).

The SPG can self-sustain a (multi)centennial weaker state through a redistribution of the upper-ocean heat and salt in the subpolar North Atlantic and Nordic Seas [Moreno-Chamarro et al., 2016, Chapter 5]. Similarly, we find a sustained reduction in the zonal gradient of seawater density in the subpolar region during the LIA (not shown) driven by an upper-ocean freshening to the west and salinification to the east of the basin (Fig. 6.6e). Associated with the

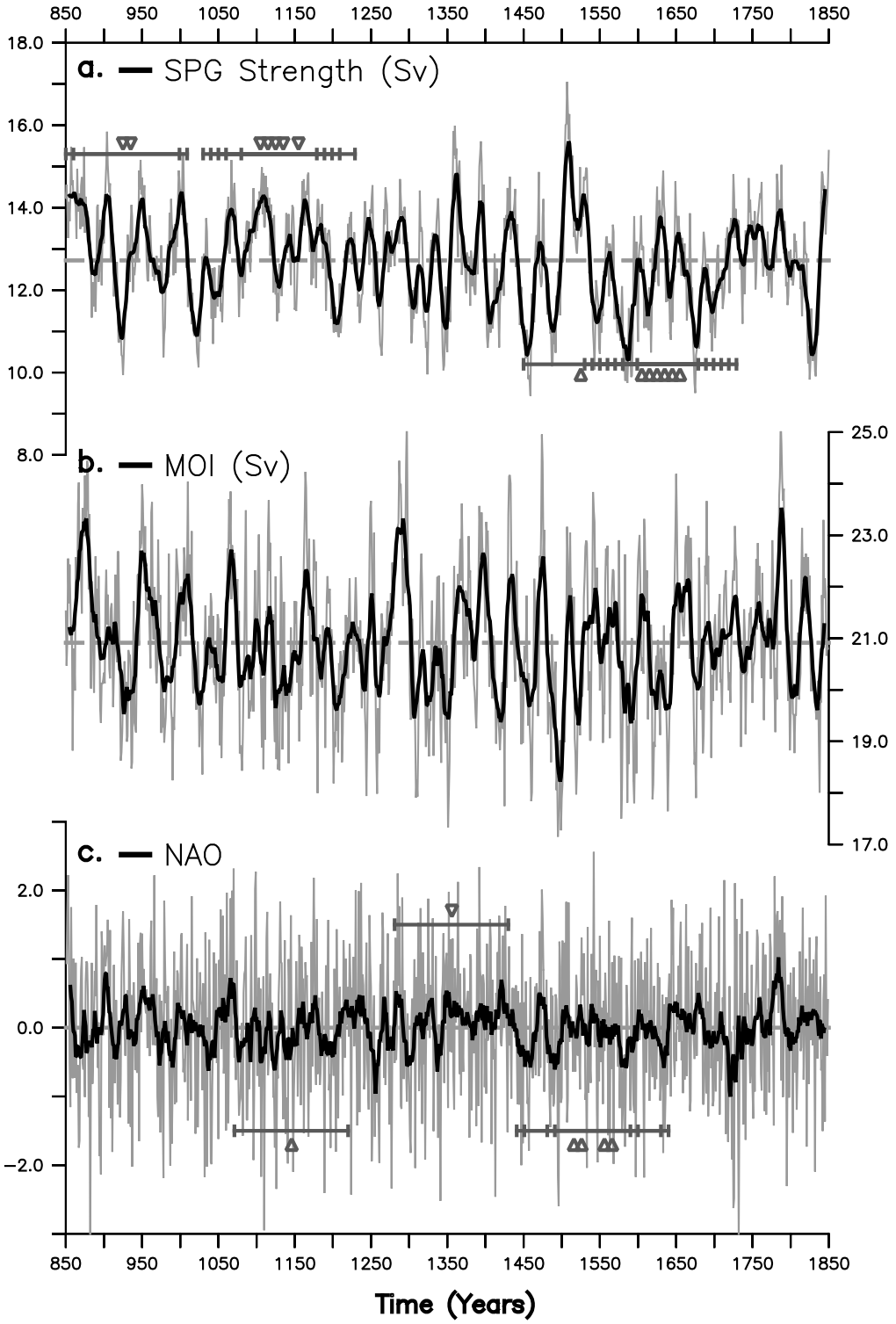

Figure 6.5: In Past1000-R2: **(a)** SPG strength (in Sv), **(b)** MOI (in Sv), and **(c)** wintertime (DJF) NAO index (dimensionless; 55% of the explained total variance; patter not shown but similar to the one in Fig. 1.4, left). Gray and black lines are respectively the yearly values and the 11-year running mean. Horizontal dashed lines are the long-term mean. Horizontal solid bars above and below time series are calculated as in Fig. 6.3.

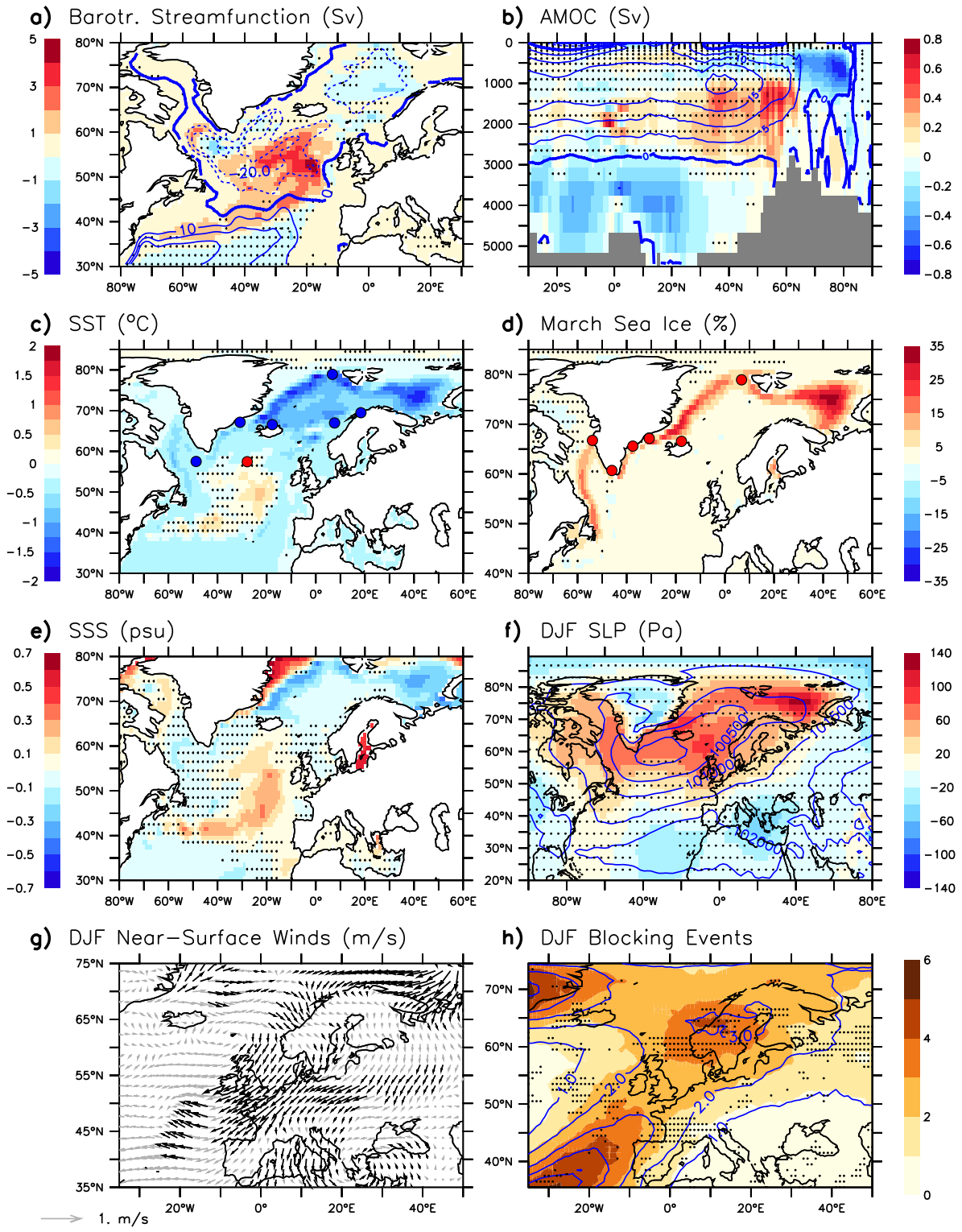

Figure 6.6: (Caption next page.)

Figure 6.6: (Previous page.) In Past1000-R2, anomalies between 1575 CE and 1724 CE (shading in Fig. 6.1a) with respect to the climatology in PiControl in the **(a)** barotropic streamfunction (in Sv, shading), **(b)** meridional overturning circulation (in Sv, shading), **(c)** SST (in °C), **(d)** late-winter (March) sea ice concentration (in percent of area), **(e)** SSS (in psu), and winter (DJF) **(f)** SLP (in Pa) and **(g)** near-surface wind (in m/s). **(h)** DJF blocking frequency between 1575 CE and 1724 CE (shading), calculated using the indicator described in Scherrer et al. [2006]. Note that each increase of one unit in the blocking index corresponds to five or more additional days under blocked atmospheric situations. Hatching and gray arrows in **(a–g)** masks statistically non-significant anomalies above the 95% level, based on the likelihood of occurrence of the signal in PiControl; for the sake of clarity, hatching in **(h)** mask statistically significant anomalies instead. Contours represent the climatological mean in PiControl. Blue/red circles indicate relatively cold/warm upper-ocean temperatures and expanded/decreased sea ice conditions during the LIA (in **c** and **d** respectively), inferred from a collection of available proxies (shown in Fig. 6.7).

SPG weakening, both the Nordic and Barents seas undergo a long-lasting period of widespread upper-ocean cooling and expanded sea ice over the LIA centuries (Fig. 6.6c,d). Simultaneously, the weaker SPG tends to pile up heat content, thereby warming the upper layers (upper 1000 m approximately) of the eastern subpolar North Atlantic (Fig. 6.6c). The simulated response in the upper-ocean temperature and sea ice to a weak gyre agrees well with reconstructed changes during the LIA in this area (dots in Fig. 6.6c,d, and Copard et al. [2012] for a SPG reconstruction, shown in Fig. 5.9a).

Anomalously cold upper-ocean and expanded sea ice conditions throughout the LIA lead to reduced surface heat flux to the atmosphere in the Barents Sea (not shown) and, hence, to more stable wintertime atmospheric conditions (Fig. 6.6f), in agreement with results shown in Section 6.3 and those for earlier centuries of the past millennium in Lehner et al. [2013]. The development of extensive positive SLP anomalies in winter over the Barents and Nordic seas,

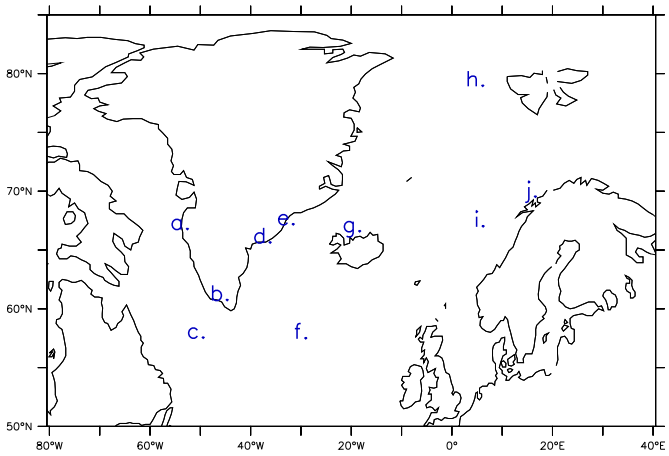

Figure 6.7: Core sites of reconstructions of upper-ocean temperature in Fig. 6.6c **(c)** Moffa-Sánchez et al. [2014b], **(e)** Miettinen et al. [2015], **(f)** Miettinen et al. [2012], **(g)** Sicre et al. [2008], **(h)** Spielhagen et al. [2011], **(i)** Berner et al. [2011], and **(h)** Hald et al. [2007], and of sea ice conditions in Fig. 6.6d **(a)** Sha et al. [2016], **(b)** Jensen et al. [2004], **(d)** Andresen et al. [2013], **(e)** Miettinen et al. [2015], **(g)** Massé et al. [2008], and **(h)** Werner et al. [2011].

Northern Europe and the subpolar North Atlantic leads to substantial, long-lasting changes in the atmospheric circulation over the European continent during this period (Fig. 6.6g): on the one hand, it leads to anomalous near-surface north-northeasterlies over Central and Eastern Europe, that favor the advection of air masses from the Barents Sea and Arctic, indeed colder, into the European continent; on the other hand, it leads to anomalous easterlies over Western Europe and the North Atlantic that block the entrance of warm and humid air masses from the North Atlantic to the Continent. Together with changes in upper-ocean salinity, high pressure anomalies can also contribute to sustaining the weaker SPG by reducing the wind stress over the subpolar North Atlantic during the LIA [Moreno-Chamarro et al., 2016, Chapter 5]. Over the European continent, in turn, more stable atmospheric conditions increase the frequency of wintertime blocking events during the LIA, and especially over Scandinavia (Fig. 6.6h). Blocking events are notoriously associated with weather extremes, like cold spells and floods [e.g., Trigo et al., 2004; Lau and Kim, 2012], that could thus have occurred more often throughout the LIA, in agreement with the documentary records from these centuries [Behringer et al., 2005]. Such atmospheric configuration, which is rooted in a weaker SPG, therefore allows explaining the reconstructed climate changes over the European continent during LIA winters (Fig. 6.1c).

The mechanism proposed for the winter season is, however, not at play during the LIA summer season: anomalies in SLP and near-surface winds are mostly statistically non-significant for the period 1575–1724 CE (Fig. 6.8), even though the magnitude of the SPG weakening and upper-ocean cooling remains relatively constant all year round (not shown). This result is consistent with the small impact the ISR HTTR has on the European summer climate (Section 6.3) and does not support the mechanism proposed in Lehner et al. [2013] for the summer cooling in the late 15th century. Another mechanism must therefore drive the reconstructed and simulated summer cooling in Europe. According to results in Section 6.2, European temperatures on decadal and longer time scales show high co-variability with those for the whole NH in summer (Fig. 6.2); in turn, NH temperature variations mainly respond to

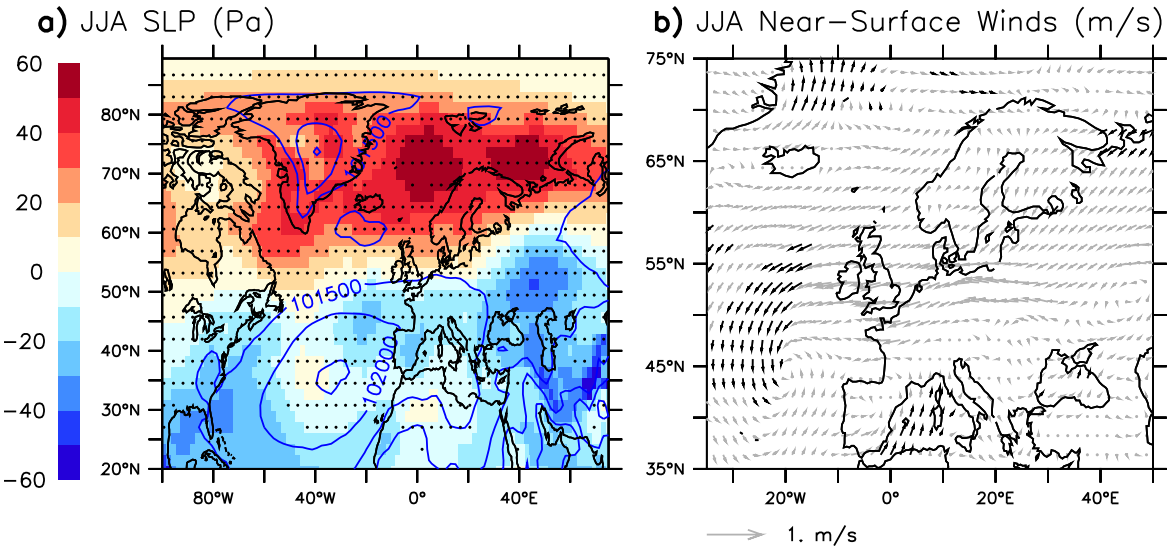

Figure 6.8: In Past1000-R2, anomalies between 1575 CE and 1724 CE (shading in Fig. 6.1a) with respect to the climatology in PiControl in summer (JJA) **(a)** SLP (in Pa) and **(b)** near-surface winds (in m/s), as in Fig. 6.6.

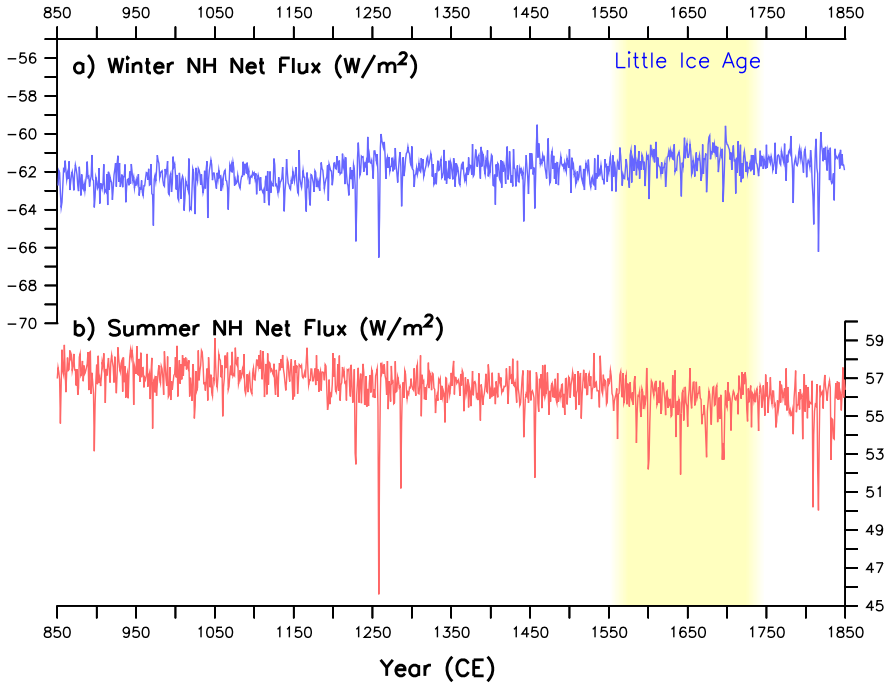

Figure 6.9: In Past1000-R2, net downward radiative flux (in W/m^2), accounting for both long and short waves, at the top of the atmosphere on average for the Norther Hemisphere in **(a)** winter and **(b)** summer. Shading covers the LIA period 1575–1724 CE, as in Fig. 6.1a.

externally forced variations in the Earth's energy balance [Fernández-Donado et al., 2013]. In the Past1000 ensemble, NH summers during the LIA are characterized by a reduction in the net downward radiative flux at the top of the atmosphere of about –0.75 W/m^2 (for the period 1575–1724 CE, with respect to each Past1000's pre-industrial climatology; Fig. 6.9a for Past1000-R2) that leads to cooling through less surface heating (not shown). The corresponding LIA winters show instead an increase of about 0.52 W/m^2 (Fig. 6.9b)—that is, less energy leaves the Earth—as a result of colder surface conditions. These anomalies are similar both in sign and magnitude for the European continent alone, and for the entire globe. This radiative imbalance, which occurs embedded in an millennial-scale trend due to orbital changes, can most likely be attributed to external forcing factors, namely volcanic, solar, and/or the greenhouse gas one. These results thus allow concluding that the European LIA summer cooling stems from externally driven changes in the Earth's radiative balance during these centuries. The mechanism proposed above for the winter season in turn leads to a regional amplification of such cooling over the Continent. Furthermore, the lack of persistent changes in the atmospheric circulation and the direct link to radiative forcing in summer, in contrast to winter, are compatible with records of fluctuating temperatures between anomalously hot and cold summers in Central Europe, embedded in a multicentennial period of anomalously cold winters [e.g., Behringer et al., 2005; Glaser and Riemann, 2009]. Our model results thus enable us to explain the reconstructed seasonal features of the European temperature during the LIA.

6.5 Attribution of the European Little Ice Age cooling to external forcing

Changes in the external forcing are the most likely responsible of the period of cold temperatures that is consistently simulated in the Past1000 ensemble and reconstructed in the European temperatures. In particular, the 17th and 18th centuries were characterized by an increase in the volcanic activity, a transition toward the Maunder minimum in the incoming solar radiation (Fig. 6.1b), and by a slight decrease in the greenhouse gas concentrations (Fig. 2.1c). We perform and analyze two sensitivity experiments for the pre-industrial past millennium (850–1849 CE) in order to disentangle the role of the solar forcing in the onset of the European LIA: Past1000-R4, which includes only changes in the incoming solar radiation (without orbital changes), and Past1000-R5, which includes all forcings but the solar (see Chapter 2 for a more detailed description of the forcings). Implementation of these experiments follows the same protocol as for the other Past1000s (see Chapter 2 for details).

In contrast to the full-forcing Past1000s (i.e., Past1000-R1 to R3), the simulated summer EMTs in the two sensitivity experiments show less agreement with the reconstructed temperature changes over the past millennium (Fig. 6.10a), with mostly statistically non-significant correlations (not shown). Notwithstanding this, the summer EMT in the all-but-solar Past1000-R5 falls well within the range of the full-forcing ensemble (gray shading in Fig. 6.10a) after some of the strongest volcanic eruptions, like the one in 1250 CE, in 1809/10 CE, or those throughout the 17th century. This seems not to be the case of the only-solar Past1000-R4, whose summer EMT rarely shows long-lasting agreement with the range of the full-forcing ensemble. On the other hand, winter EMTs for both Past1000-R4 and R5 exhibit a similar range of variability to the full-forcing ensemble and LUT04's reconstruction (Fig. 6.10b). These results are consistent with those in Section 6.2, since summer and winter EMTs are primarily related to externally forced global changes and to internal-regional climate variability of the European region respectively.

Spatially, patterns of continental cooling during LIA summers and winters in Past1000-R5 are similar to those in the full-forcing simulations and can, thus, be explained by the mechanism proposed above: Past1000-R5 shows an anomalously weaker SPG strength during the centuries extending the LIA (Fig. 6.11b), which is further associated with colder conditions in the upper Nordic and Barents seas and expanded sea ice edges (Fig. 6.12, lower panels). However, such centennial SPG weakening is statistically non-significant, and the magnitude of the climate anomalies in the North Atlantic/Arctic region is smaller than in the full-forcing Past1000s (compare Figs. 6.12 and 6.6). In summer, this seems to be related to a delayed onset of the LIA cooling over Europe in Past1000-R5, by about 50 years with respect to the full-forcing ensemble or the Pages2k reconstruction (Fig. 6.10a), that results in much warmer conditions during the coldest centuries around 1600 CE. In winter, by contrast, the not-so-cold cold conditions over Europe in Past1000-R5 seem to be associated with relatively warm temperatures between 1650 CE and 1724 CE (Fig. 6.10b), after the coldest decades of the LIA, although these changes are within the range of the full-forcing ensemble and somehow agree with the LUT04's reconstruction after 1700 CE. The forcing imposed in Past1000-R5 thus seems not enough to force a LIA of a magnitude like the one simulated with all forcings, although it is not fully clear the reason of such discrepancy, which might even be related to internal climate dynamics.

The solar-only Past1000-R4, on the other hand, features warmer winters over Central and

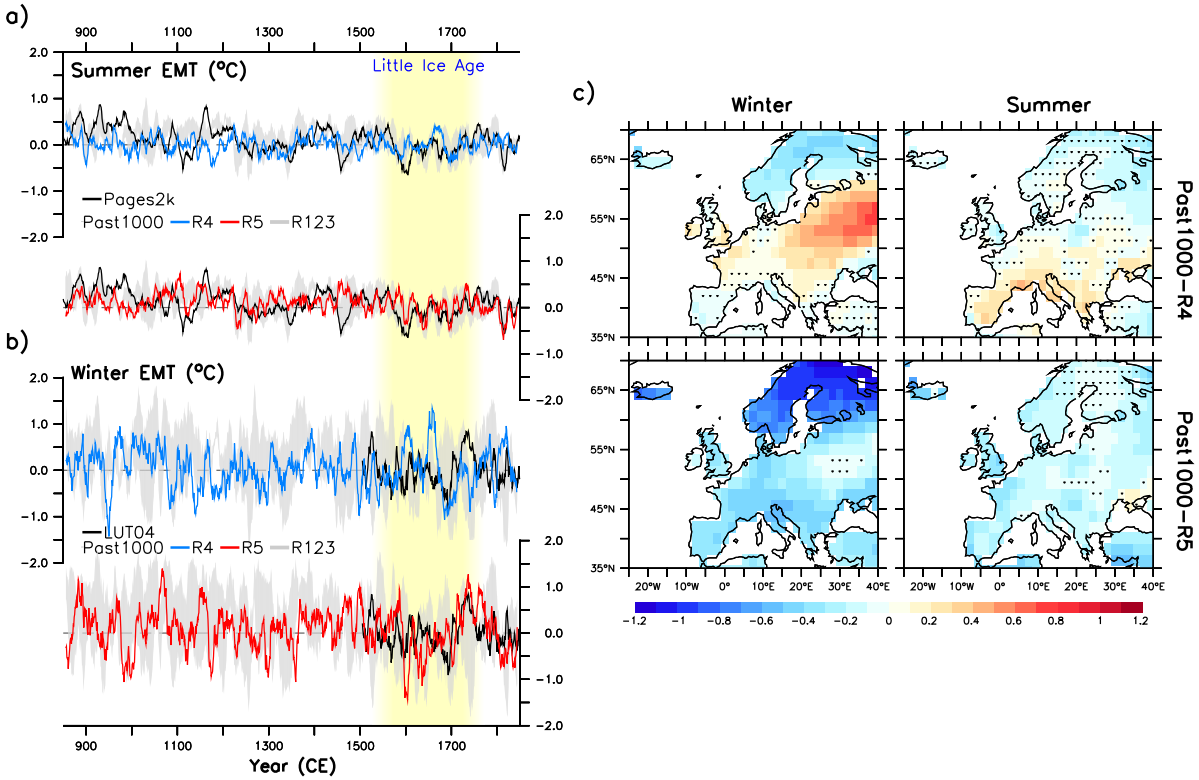

Figure 6.10: **(a)** EMT in Past1000-R4 and R5 (blue and red lines respectively) in **(a)** summer and **(b)** winter, and the corresponding Pages2k and LUT04's reconstructions (black lines), as in Fig. 6.1a. Gray shading indicates the range of EMTs in the full-forcing Past1000 ensemble, from Fig. 6.1a. **(c)** Spatial distribution of land temperature anomalies (in °C) between 1575 CE and 1724 CE (shading in **a** and **b**) in Past1000-R4 and Past1000-R5 (upper and lower panels respectively), with respect to the climatology in PiControl. Note that the simulated anomalous patterns shown in Fig. 6.1c do not substantially change if they are calculated with respect to the PiControl climatology (not shown), and can therefore be directly compared with those shown here. Hatching masks statistically insignificant anomalies above the 95% level, based on the likelihood of occurrence of the signal in PiControl.

Eastern Europe during the first half of the LIA, followed by a rapid cooling persisting into 1700–1750 (Fig. 6.10b,c). These changes might be forced by those in the solar forcing throughout this period (Fig. 6.1b), although similar episodes of continental winter warming/cooling are not clearly discernible for other solar maximum/minimum throughout the pre-industrial past millennium. In addition, Past1000-R4 shows no (multi)centennial changes in the SPG strength during the entire millennium (Fig. 6.11a), nor during the LIA. The upper-ocean cooling and expanded sea ice conditions that are simulated between 1575 CE and 1724 CE are statistically non-significant over most areas (Fig. 6.12, upper panels); such changes might indeed be the fingerprint of the decadal cold event occurring between ca. 1650 CE and 1710 CE (this can be detected, for example, in the SPG strength in Fig. 6.11a; Moreno-Chamarro et al. [2015], Chapter 4), although they can also be caused by the solar Maunder minimum around 1700 CE (Fig. 6.1b). Regardless of the case, changes in the solar forcing as implemented in the model alone appear not to suffice to trigger a European continental cooling as strong and significant as that reconstructed during the LIA, which is consistent with the fact that the LIA onset is simulated in the full-forcing during the solar maximum peaking around 1600 CE. Nonetheless,

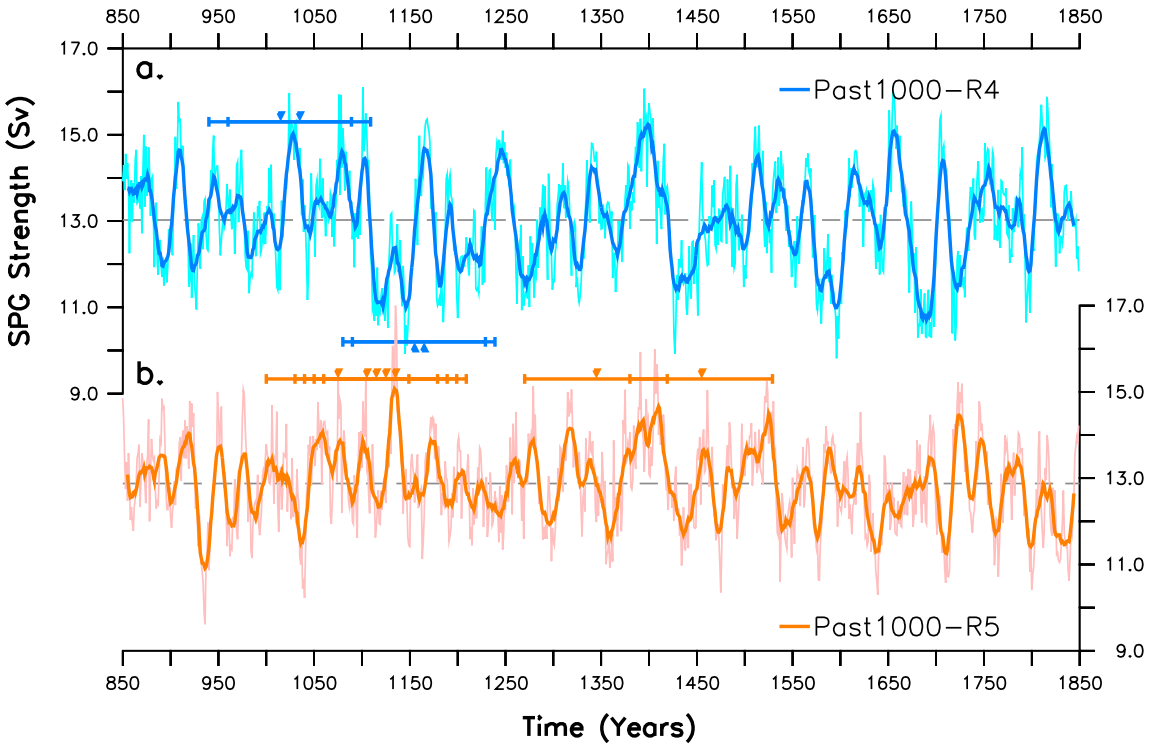

Figure 6.11: The SPG strength (in Sv), as in Fig. 6.5a, in **(a)** Past1000-R4 and **(b)** R5.

results in Past1000-R4 and R5 also suggest that the Maunder minimum in the solar forcing might contribute to deepening the LIA cooling and making it persist over a multicentennial period. These results should, however, be taken with a grain of salt, since they are based on a single realization of each forcing configuration; relatively large ensembles of such experiments are needed for a complete understanding of the range of variability associated with all relevant forcings in the past millennium [e.g., Otto-Bliesner et al., 2015].

6.6 Discussion

This Chapter discussed the mechanisms underlying winter and summer climate changes from the 16th to 18th centuries during the LIA over Europe. We thus showed that the response of the atmospheric circulation to a reduction in the SPG-driven poleward heat transport can lead to a regional amplification of the continental cooling during the LIA winters, with respect to summer, which is, moreover, consistent with reconstructions and records of the European climate covering these centuries. In the model, the atmospheric response specifically consists of widespread high pressure anomalies over the Nordic and Barents seas, Northern Europe, and the subpolar North Atlantic (Fig. 6.6f), which somehow resemble a negative NAO phase, even though the actual NAO shows no long-lasting change (Fig. 6.5c). Under such conditions, an index calculated by subtracting SLP values over Morocco to those over Scotland, similarly as for the NAO reconstruction in Trouet et al. [2009], exhibits an abrupt reduction at the onset of the LIA, around 1550 CE (not shown). Trouet et al. [2009]'s reconstruction might therefore reflect a change to mostly blocked wintertime atmospheric conditions over Europe, as described in Section 6.4, rather than a shift into a persistent anomalous NAO phase.

The analysis of the two sensitivity experiments suggested a relative important role of the

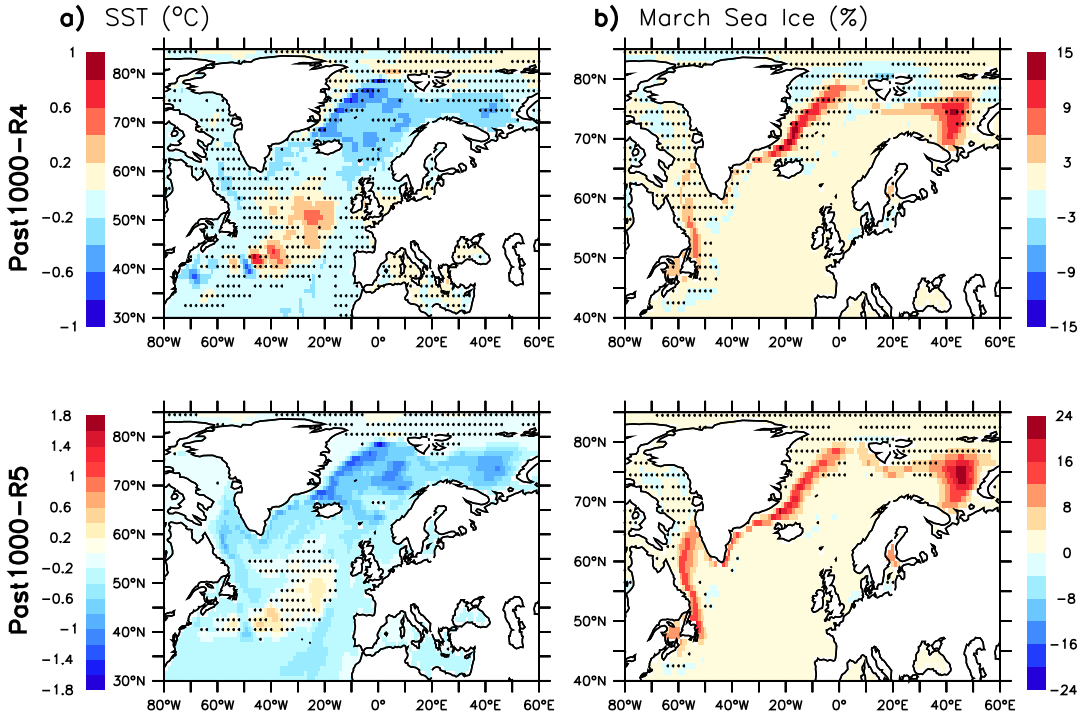

Figure 6.12: SST and sea ice concentration anomalies (left and right panels respectively) during the LIA in Past1000-R4 and R5 (upper and lower panels respectively), calculated as in Fig. 6.6.

solar forcing in sustaining the European cold conditions during the LIA, albeit not in its onset, as also conjectured in Chapter 5 [Moreno-Chamarro et al., 2016]. Therefore, one of the other imposed forcings alone or a combination of them seems to be responsible for triggering the LIA. A multi-model assessment of the relative contribution of each individual forcing based on Past1000 simulations with state-of-the-art climate models revealed that the LIA-related global cooling between 1600 CE and 1850 CE was largely driven by volcanic forcing, with minor contributions from the solar or greenhouse gas concentration changes [Atwood et al., 2015]. Along this same line, we showed in Chapter 5 of this thesis that the volcanic forcing can aid to trigger LIA-like events in the North Atlantic that can eventually impact the European climate, although we found this mechanism highly influenced by internal climate dynamics. Taken together, these results thus sketch the LIA as a "perfect storm" of both a volcanically driven onset, yet deeply influenced by internal climate dynamics, and a following solar-related deepening. Due to the nonlinear and chaotic nature of the climate, however, we are unable to determine the exact contribution of each forcing and/or the internal climate variability in determining such an event; as stated previously, such analysis requires the performance of rather large ensembles of single-forcing experiments.

According to results so far, it is likely that the intense volcanism between ca. 1550 CE and 1600 CE caused the inception of the LIA. Even though volcanic eruptions during this period are, in general, of much smaller magnitude than other events during the past millennium, they follow each other closely (Fig. 6.1b). Reconstructions of the volcanic forcing, like the one applied in our Past1000 ensemble from Crowley and Unterman [2013], further indicate that aerosols from these eruptions mostly contributed to the northern extra-tropics, thereby inducing a persistent and rather localized radiative forcing. Such a peculiar configuration might be responsible of increasing NH's albedo and, by extension, of causing the continental

summer cooling simulated during the LIA, as previously shown in Section 6.4. Extended to the winter season, this cooling might also explain the late-winter sea ice growth that is robustly simulated in the Past1000 ensemble between ca. 1550 CE and 1650 CE in the North Atlantic and Arctic oceans (for example, Fig. 5.5e for Past1000-R3). Such response in the sea ice can in turn trigger a multicentennial SPG weakening through freshening of the Labrador Sea, as shown in Chapter 5, ultimately activating the above-described amplifying mechanism in winter. Substantial differences however exist between available volcanic forcing data-sets for the past millennium, and in particular concerning the latitudinal distribution of the volcanic aerosols. Constraining the uncertainties on volcanic forcing is therefore necessary in order to substantiate the hypothesis proposed above.

6.7 Conclusions

This Chapter investigated the extent to which SPG dynamics and related northward heat transport could have caused the coldest European period during the LIA (between ca. 1550 CE and 1750 CE). The analysis, based on an ensemble of climate simulations of the past millennium (Past1000s), focused on the dichotomy of the summer and winter climate evolution during the LIA, aiming at clarifying the underlying driving mechanisms. Our results indicate that:

1. Reconstructed and simulated European temperatures consistently show colder anomalies in LIA winters than in their respective summers. This stems from an amplifying mechanism that is more efficient in winter than in summer, and that relates a multicentennial weakening in the SPG strength and its associated heat inflow into the Nordic and Barents seas, with long-term changes in the atmospheric circulation over the European continent and more frequent and persisting blocking events and related cold spells. This mechanism does not require an AMOC slowdown or a shift between NAO phases. In summer, by contrast, the LIA-related cooling emanates mainly from reduced continental heating, and not from widespread changes in the atmospheric circulation. This set of mechanisms thus allow explaining the pattern and magnitude of the reconstructed climate anomalies during the LIA for both seasons over Europe based on SPG changes alone.

2. Comparison among Past1000 simulations with different forcing configurations suggest that the Maunder minimum in the solar forcing is necessary to sustain and deepen this cold episode into the late 17th and 18th centuries, but not for its onset.

Chapter 7

Conclusions and final remarks

The main goal of this thesis was to better understand the climate variability of the North Atlantic, Arctic, and European regions at decadal to multicentennial time scales during the preindustrial past millennium. Focusing on this particular period allowed assessment of natural climate changes alone. Most of the analysis was based on an ensemble of three transient climate simulation for this period, performed with a state-of-the-art Earth system model including the most relevant external forcings for this period. When needed, results were supported by sensitivity experiments with different forcing configurations and/or initial conditions. Additionally, we compared our model results with those from the most recent (up to date) climate reconstructions.

7.1 Summary of findings

We conclude this thesis revisiting the research questions raised in the Introduction:

1) What physical mechanisms allow explaining the main features of the cold conditions in the North Atlantic and Europe during the LIA?

The relatively cold conditions over Northern and Central Europe during LIA winters, compared to the Mediterranean region or their respective summers, are explained by atmospheric circulation changes over the European continent driven by a weakening of the SPG and its associated northward heat transport. This mechanism is, however, only at play during the winter season, when it amplifies the externally forced radiative cooling between the mid-16th and the early 18th century.

What relative role did the reconstructed changes in the SPG play in driving the North Atlantic and European cooling during the LIA, with respect to those in the AMOC or the NAO?

We find no evidence supporting a reduction in the oceanic northward heat transport by the AMOC as the main driver of the cold conditions in the North Atlantic or Europe during the LIA, nor the hypothesis of a more variable NAO or a shift toward predominantly negative NAO phases in these centuries. Rather, the weakening of the SPG stands as the principal cause of the cold period that the North Atlantic underwent during the LIA. The SPG weakening and, hence, LIA-type events can nonetheless develop smoothly, throughout the centuries, or abruptly, in the course of a few decades. The onset of the abrupt SPG weakening, although aided by volcanic forcing, is strongly influenced by internal climate dynamics, which can further explain the discrepancy with the reconstructed estimates.

3) Is the physical mechanism that allows explaining decadal cold events in the North Atlantic related to any global or hemispheric phenomenon triggered by a particular external forcing?

Decadal cold events can develop unpredictably in the subpolar region as a result of internal climate dynamics alone. The amplifying climate feedback primarily relates a weakening of the SPG strength, a broad freshening of the upper Labrador Sea, and a deep convection shutdown. Climate changes associated with these events are rather localized in the western subpolar North Atlantic, and particularly over Western Greenland, where persisting cold conditions during a few decades extend over the former location of the Norse settlements. We therefore reject previous hypotheses associating such cold events with hemispheric or global climate changes or with external forcing.

7.2 Discussion and research perspective

This thesis explored climate processes behind the reconstructed natural climate variability in the preindustrial past millennium. Since natural climate variability can itself be divided into internal and externally forced variability, we repeatedly intended to attribute the study phenomena either to the former or to the latter. In several occasions, however, we found ourselves unable to give a conclusive answer, so that the question remains open for future research. Despite this, this thesis exemplifies well that these two sort of climate variability are key to fully understand climate changes during the past millennium. Thus, for example, Chapter 4 described decadal cold events in the subpolar North Atlantic that can be triggered by internal climatic processes alone, and whose anomalies barely extend farther away from this region. In other words, such cold events can be described as a regional, internal phenomenon of the subpolar North Atlantic. We believe this result must stand as an important warning note when it comes to interpret results from climate reconstructions. Often, climate changes reconstructed in specific locations are interpreted in terms of changes in the external forcing, such as volcanic eruptions, and are further connected to hemispheric or global climate changes, like the onset of the LIA. Yet, they are rarely seen just as signals of local or regional climate, like the decadal cold events described here. Comprehensive climate models can thus help to interpret more accurately these reconstructions, as they allow describing, in multiple realization, the dynamical connections between local and large-scale climate variations.

The abrupt shift in the SPG strength studied in Chapter 5 is another example of the interaction between internal and externally forced climate variability, which is, in this case, twofold. On the one hand, the SPG strength was found following two different trajectories during the preindustrial past millennium, either with a relatively long-lasting weakening (in Past1000-R1 and R2), or with an abrupt shift (in Past1000-R3), but both toward a similar, weak, cold LIA-like state in the last centuries. Such dichotomy might be related to the way climate integrates both externally forced climate variability over time and initial climate conditions, as suggested by the fact that R1 and R2 share the initial ocean state but implement slightly differently the external forcing, whereas R3 has a different initial ocean state but the same forcing as R2. This indicates that initial climate conditions might exert an influence on the evolution of the climate even on multicentennial to millennial time scales that can be comparable to the one commonly attributed to external forcing. If this is the case, climate model experiments of the past millennium should include a relatively large number of ensemble members covering a wide enough range of initial climate conditions, in order to

incorporate as many trajectories as possible.

Another aspect that deserves special mention relating the abrupt onset of the SPG concerns the onset itself, as it stands as a combination between, at least, the volcanic forcing and internal climate dynamics. Our sensitivity experiments were designed to assess the role of the volcanic forcing just for the detected event, and always at the end of the 16th century. It thus remains open whether a similar event can be simulated earlier in the past millennium, more in accordance with climate proxy records. This investigation would require identifying the particular background climate conditions that facilitate the onset of a shift, so that, in a subsequent step, earlier volcanic eruptions in the past millennium can be imposed upon them. In addition to this, the question of whether, and if so how, other external forcings contribute to this event still remains unanswered.

Chapter 6 in turn showed how a weakened SPG-related northward heat transport can lead to a broad change in the winter atmospheric circulation over the European continent that can result in a seasonal amplification of the LIA cooling. Apart from the open question related to the onset of such an event, already tackled in Section 6.6, it is still an enigma whether the relatively early abrupt SPG shift in the 14th and 15th centuries shown in climate proxies is compatible with further weakening in the 17th and 18th centuries, when Europe experienced the coldest centuries of the LIA. This theory, which is sketched in Figure 7.1, seems to be supported by some climate reconstructions within the North Atlantic/Arctic region that show a deepening of the warming/cooling after an early shift [e.g., Massé et al., 2008; Sicre et al., 2008; Berner et al., 2011; Hald et al., 2007; Miettinen et al., 2012; Ran et al., 2011, some in Fig. 5.9].

One of the main shortcomings of this investigation is that it is based on a single climate model; hence, it is still open to discussion, for example, to what extent the biases this model presents [Jungclaus et al., 2013] have influenced our results, or whether other but similar models, or even an updated version of the same model, can reproduce them. Further source of uncertainty arises from the fact that our simulations were performed imposing state-of-the-art reconstructions for the external forcings [Schmidt et al., 2011]. Since updated versions of such reconstructions already exist [e.g., Sigl et al., 2015], one might wonder how this would affect our conclusions. All these questions must, nevertheless and for now, be left open for future studies.

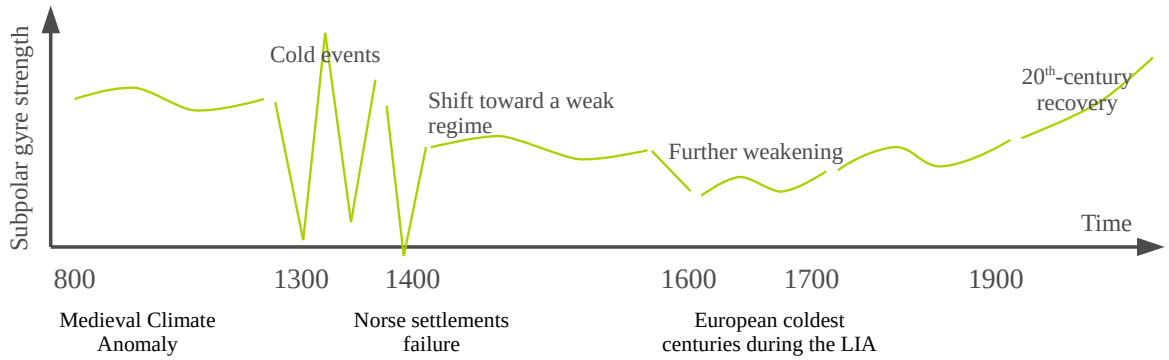

Figure 7.1: A possible evolution of the SPG strength over the pre- and industrial periods according to modeling results in this thesis and climate reconstructions from the North Atlantic and Arctic region (some shown in Fig. 5.9). Evidence of a gyre recovery and further strengthening during the 20th century can be found in Copard et al. [2012] and Jungclaus et al. [2014]. Some historical events described throughout this thesis are also indicated.

In conclusion, this thesis evidenced that SPG dynamics are key to understand the nature of some of the most relevant climate episodes in the North Atlantic, Arctic, and European regions during the past millennium. This finding thus allowed rejecting previous, and indeed unsatisfactory, hypotheses attributing them mainly to AMOC or NAO variations. In particular, the SPG emerged as the main driver of spontaneous, decadal cold events in the subpolar North Atlantic. In addition, the main features of the climate changes in the North Atlantic/Arctic area during the LIA could consistently be explained by a weak SPG state. Finally, the connection between the SPG and the European climate resulted essential to disentangle the seasonality of the European LIA cooling.

Bibliography

Andresen, C., Hansen, M., Seidenkrantz, M.-S., Jennings, A., Knudsen, M., Nørgaard-Pedersen, N., Larsen, N., Kuijpers, A., and Pearce, C. (2013). Mid-to late-Holocene oceanographic variability on the Southeast Greenland shelf. *The Holocene*, 23(2):167–178.

Arneborg, J., Lynnerup, N., Heinemeier, J., Møhl, J., Rud, N., and Sveinbjörnsdóttir, Á. E. (2012). Norse Greenland dietary economy ca. AD 980-ca. AD 1450: Introduction. *Journal of the North Atlantic*, 3:1–39.

Atwood, A., Wu, E., Frierson, D., Battisti, D., and Sachs, J. (2015). Quantifying climate forcings and feedbacks over the last millennium in the CMIP5/PMIP3 models. *Journal of Climate*, (2015).

Bauer, E., Claussen, M., Brovkin, V., and Huenerbein, A. (2003). Assessing climate forcings of the Earth system for the past millennium. *Geophysical Research Letters*, 30(6).

Behringer, W., Lehmann, H., and Pfister, C. (2005). *Cultural consequences of the "Little Ice Age"*, volume 212. Vandenhoeck & Ruprecht.

Berner, K., Koç, N., Godtliebsen, F., and Divine, D. (2011). Holocene climate variability of the Norwegian Atlantic Current during high and low solar insolation forcing. *Paleoceanography*, 26(2).

Born, A., Nisancioglu, K. H., and Braconnot, P. (2010). Sea ice induced changes in ocean circulation during the Eemian. *Climate Dynamics*, 35(7-8):1361–1371.

Born, A. and Stocker, T. F. (2014). Two stable equilibria of the Atlantic subpolar gyre. *Journal of Physical Oceanography*, 44(1):246–264.

Born, A., Stocker, T. F., Raible, C. C., and Levermann, A. (2013). Is the atlantic subpolar gyre bistable in comprehensive coupled climate models? *Climate dynamics*, 40(11-12):2993–3007.

Braconnot, P., Harrison, S. P., Kageyama, M., Bartlein, P. J., Masson-Delmotte, V., Abe-Ouchi, A., Otto-Bliesner, B., and Zhao, Y. (2012). Evaluation of climate models using palaeoclimatic data. *Nature Climate Change*, 2(6):417–424.

Copard, K., Colin, C., Henderson, G., Scholten, J., Douville, E., Sicre, M.-A., and Frank, N. (2012). Late Holocene intermediate water variability in the northeastern Atlantic as recorded by deep-sea corals. *Earth and Planetary Science Letters*, 313:34–44.

Crowley, T. (2000). Causes of climate change over the past 1000 years. *Science*, 289(5477):270.

Crowley, T. and Unterman, M. (2013). Technical details concerning development of a 1200 yr proxy index for global volcanism. *Earth System Science Data*, 5(1):187–197.

Cunningham, L. K., Austin, W. E., Knudsen, K. L., Eiríksson, J., Scourse, J. D., Wanamaker, A. D., Butler, P. G., Cage, A. G., Richter, T., Husum, K., et al. (2013). Reconstructions of surface ocean conditions from the northeast Atlantic and Nordic Seas during the last millennium. *The Holocene*, 23(7):921–935.

De Jong, R., Kamenik, C., and Grosjean, M. (2013). Cold-season temperatures in the European Alps during the past millennium: variability, seasonality and recent trends. *Quaternary Science Reviews*, 82:1–12.

Delworth, T., Manabe, S., and Stouffer, R. (1993). Interdecadal variations of the thermohaline circulation in a coupled ocean-atmosphere model. *Journal of Climate*, 6(11):1993–2011.

Deshayes, J. and Frankignoul, C. (2008). Simulated variability of the circulation in the North Atlantic from 1953 to 2003. *Journal of Climate*, 21(19):4919–4933.

Dobrovolnỳ, P., Moberg, A., Brázdil, R., Pfister, C., Glaser, R., Wilson, R., van Engelen, A., Limanówka, D., Kiss, A., Halíčková, M., et al. (2010). Monthly, seasonal and annual temperature reconstructions for Central Europe derived from documentary evidence and instrumental records since AD 1500. *Climatic Change*, 101(1-2):69–107.

Drijfhout, S., Gleeson, E., Dijkstra, H. A., and Livina, V. (2013). Spontaneous abrupt climate change due to an atmospheric blocking–sea-ice–ocean feedback in an unforced climate model simulation. *Proceedings of the National Academy of Sciences*, 110(49):19713–19718.

Dugmore, A. J., McGovern, T. H., Vésteinsson, O., Arneborg, J., Streeter, R., and Keller, C. (2012). Cultural adaptation, compounding vulnerabilities and conjunctures in Norse Greenland. *Proceedings of the National Academy of Sciences*, 109(10):3658–3663.

Dylmer, C., Giraudeau, J., Eynaud, F., Husum, K., and Vernal, A. D. (2013). Northward advection of Atlantic water in the eastern Nordic Seas over the last 3000 yr. *Climate of the Past*, 9(4):1505–1518.

Eden, C. and Willebrand, J. (2001). Mechanism of interannual to decadal variability of the North Atlantic circulation. *Journal of Climate*, 14(10):2266–2280.

Fagan, B. M. (2000). *The Little Ice Age: how climate made history, 1300-1850*. Basic books.

Fernández-Donado, L., González-Rouco, J., Raible, C., Ammann, C., Barriopedro, D., Garcıa-Bustamante, E., Jungclaus, J., Lorenz, S., Luterbacher, J., Phipps, S., et al. (2013). Large-scale temperature response to external forcing in simulations and reconstructions of the last millennium. *Climate of the Past*, 9:393–421.

Gelderloos, R., Straneo, F., and Katsman, C. A. (2012). Mechanisms behind the temporary shutdown of deep convection in the Labrador Sea: Lessons from the Great Salinity Anomaly Years 1968-71. *Journal of Climate*, 25(19):6743–6755.

Gennaretti, F., Arseneault, D., Nicault, A., Perreault, L., and Bégin, Y. (2014). Volcano-induced regime shifts in millennial tree-ring chronologies from northeastern North America. *Proceedings of the National Academy of Sciences*, 111(28):10077–10082.

Glaser, R. and Riemann, D. (2009). A thousand-year record of temperature variations for Germany and Central Europe based on documentary data. *Journal of Quaternary Science*, 24(5):437–449.

Gómez-Navarro, J. and Zorita, E. (2013). Atmospheric annular modes in simulations over the past millennium: no long-term response to external forcing. *Geophysical Research Letters*, 40(12):3232–3236.

Grossmann, I. and Klotzbach, P. J. (2009). A review of North Atlantic modes of natural variability and their driving mechanisms. *Journal of Geophysical Research: Atmospheres*, 114(D24).

Häkkinen, S., Rhines, P. B., and Worthen, D. L. (2011). Atmospheric blocking and Atlantic multidecadal ocean variability. *Science*, 334(6056):655–659.

Hald, M., Andersson, C., Ebbesen, H., Jansen, E., Klitgaard-Kristensen, D., Risebrobakken, B., Salomonsen, G. R., Sarnthein, M., Sejrup, H. P., and Telford, R. J. (2007). Variations in temperature and extent of Atlantic Water in the northern North Atlantic during the Holocene. *Quaternary Science Reviews*, 26(25):3423–3440.

Hasselmann, K. (1976). Stochastic climate models part I. Theory. *Tellus*, 28(6):473–485.

Hátún, H., Sandø, A. B., Drange, H., Hansen, B., and Valdimarsson, H. (2005). Influence of the Atlantic subpolar gyre on the thermohaline circulation. *Science*, 309(5742):1841–1844.

Hoskins, B. J. and Karoly, D. J. (1981). The steady linear response of a spherical atmosphere to thermal and orographic forcing. *Journal of the Atmospheric Sciences*, 38(6):1179–1196.

Hunt, B. (2009). Natural climatic variability and the Norse settlements in Greenland. *Climatic change*, 97(3-4):389–407.

Hurrell, J. W., Kushnir, Y., and Visbeck, M. (2001). The North Atlantic Oscillation. *Science*, 291(5504):603–605.

Jensen, K. G., Kuijpers, A., Koç, N., and Heinemeier, J. (2004). Diatom evidence of hydrographic changes and ice conditions in Igaliku Fjord, South Greenland, during the past 1500 years. *The Holocene*, 14(2):152–164.

Jiang, H., Eiríksson, J., Schulz, M., Knudsen, K.-L., and Seidenkrantz, M.-S. (2005). Evidence for solar forcing of sea-surface temperature on the North Icelandic Shelf during the late Holocene. *Geology*, 33(1):73–76.

Jungclaus, J., Fischer, N., Haak, H., Lohmann, K., Marotzke, J., Matei, D., Mikolajewicz, U., Notz, D., and Storch, J. (2013). Characteristics of the ocean simulations in the Max Planck Institute Ocean Model (MPIOM) the ocean component of the MPI-Earth system model. *Journal of Advances in Modeling Earth Systems*, 5(2):422–446.

Jungclaus, J. H., Lohmann, K., and Zanchettin, D. (2014). Enhanced 20th century heat transfer to the Arctic simulated in context of climate variations over last millennium. *Climate of the Past*, 10:2201–2213.

Kaufman, D. S., Schneider, D. P., McKay, N. P., Ammann, C. M., Bradley, R. S., Briffa, K. R., Miller, G. H., Otto-Bliesner, B. L., Overpeck, J. T., Vinther, B. M., et al. (2009). Recent warming reverses long-term arctic cooling. *Science*, 325(5945):1236–1239.

Knight, J. R., Allan, R. J., Folland, C. K., Vellinga, M., and Mann, M. E. (2005). A signature of persistent natural thermohaline circulation cycles in observed climate. *Geophysical Research Letters*, 32(20).

Koslowski, G. and Glaser, R. (1999). Variations in reconstructed ice winter severity in the Western Baltic from 1501 to 1995, and their implications for the North Atlantic Oscillation. *Climatic Change*, 41(2):175–191.

Kuijpers, A., Mikkelsen, N., Ribeiro, S., and Seidenkrantz, M.-S. (2014). Impact of medieval fjord hydrography and climate on the western and eastern settlements in Norse Greenland. *Journal of the North Atlantic*, 6:1–13.

Langehaug, H. R., Medhaug, I., Eldevik, T., and Otterå, O. H. (2012). Arctic/Atlantic Exchanges via the Subpolar Gyre*. *Journal of Climate*, 25(7):2421–2439.

Lau, W. K. and Kim, K.-M. (2012). The 2010 Pakistan flood and Russian heat wave: Teleconnection of hydrometeorological extremes. *Journal of Hydrometeorology*, 13(1):392–403.

Lehner, F., Born, A., Raible, C. C., and Stocker, T. F. (2013). Amplified inception of European Little Ice Age by sea ice–ocean–atmosphere feedbacks. *Journal of Climate*, 26(19):7586–7602.

Lehner, F., Raible, C. C., and Stocker, T. F. (2012). Testing the robustness of a precipitation proxy-based North Atlantic Oscillation reconstruction. *Quaternary Science Reviews*, 45:85–94.

Leijonhufvud, L., Wilson, R., Moberg, A., Söderberg, J., Retsö, D., and Söderlind, U. (2010). Five centuries of Stockholm winter/spring temperatures reconstructed from documentary evidence and instrumental observations. *Climatic Change*, 101(1-2):109–141.

Little, M. A., Steel, B. C., Bai, F., Sowa, Y., Bilyard, T., Mueller, D. M., Berry, R. M., and Jones, N. S. (2011). Steps and bumps: precision extraction of discrete states of molecular machines. *Biophysical Journal*, 101(2):477–485.

Lund, D., Lynch-Stieglitz, J., and Curry, W. (2006). Gulf Stream density structure and transport during the past millennium. *Nature*, 444(7119):601–604.

Luterbacher, J., Dietrich, D., Xoplaki, E., Grosjean, M., and Wanner, H. (2004). European seasonal and annual temperature variability, trends, and extremes since 1500. *Science*, 303(5663):1499–1503.

Luterbacher, J., Werner, J., Smerdon, J., Fernández-Donado, L., González-Rouco, F., Barriopedro, D., Ljungqvist, F., Büntgen, U., Zorita, E., Wagner, S., et al. (2016). European summer temperatures since roman times. *Environmental Research Letters*, 11(2):024001.

Mann, M. E., Zhang, Z., Rutherford, S., Bradley, R. S., Hughes, M. K., Shindell, D., Ammann, C., Faluvegi, G., and Ni, F. (2009). Global signatures and dynamical origins of the Little Ice Age and Medieval Climate Anomaly. *Science*, 326(5957):1256–1260.

Marshall, J., Kushnir, Y., Battisti, D., Chang, P., Czaja, A., Dickson, R., Hurrell, J., McCartney, M., Saravanan, R., and Visbeck, M. (2001). North Atlantic climate variability: phenomena, impacts and mechanisms. *International Journal of Climatology*, 21(15):1863–1898.

Marsland, S. J., Haak, H., Jungclaus, J. H., Latif, M., and Röske, F. (2003). The Max-Planck-Institute global ocean/sea ice model with orthogonal curvilinear coordinates. *Ocean Modelling*, 5(2):91–127.

Massé, G., Rowland, S. J., Sicre, M.-A., Jacob, J., Jansen, E., and Belt, S. T. (2008). Abrupt climate changes for Iceland during the last millennium: evidence from high resolution sea ice reconstructions. *Earth and Planetary Science Letters*, 269(3):565–569.

Masson-Delmotte, V., Schulz, M., Abe-Ouchi, A., Beer, J., Ganopolski, A., González Rouco, J., Jansen, E., Lambeck, K., Luterbacher, J., Naish, T., et al. (2013). Information from paleoclimate archives. *Climate change*, pages 383–464.

McGregor, H. V., Evans, M. N., Goosse, H., Leduc, G., Martrat, B., Addison, J. A., Mortyn, P. G., Oppo, D. W., Seidenkrantz, M.-S., Sicre, M.-A., et al. (2015). Robust global ocean cooling trend for the pre-industrial common era. *Nature Geoscience*.

Miettinen, A., Divine, D., Koç, N., Godtliebsen, F., and Hall, I. R. (2012). Multicentennial variability of the sea surface temperature gradient across the subpolar North Atlantic over the last 2.8 kyr*,+. *Journal of Climate*, 25(12):4205–4219.

Miettinen, A., Divine, D. V., Husum, K., Koç, N., and Jennings, A. (2015). Exceptional ocean surface conditions on the SE Greenland shelf during the Medieval Climate Anomaly. *Paleoceanography*, 30(12):1657–1674.

Miller, G. H., Geirsdóttir, Á., Zhong, Y., Larsen, D. J., Otto-Bliesner, B. L., Holland, M. M., Bailey, D. A., Refsnider, K. A., Lehman, S. J., Southon, J. R., et al. (2012). Abrupt onset of the Little Ice Age triggered by volcanism and sustained by sea-ice/ocean feedbacks. *Geophysical Research Letters*, 39(2).

Moffa-Sánchez, P., Born, A., Hall, I. R., Thornalley, D. J., and Barker, S. (2014a). Solar forcing of North Atlantic surface temperature and salinity over the past millennium. *Nature Geoscience*, 7(4):275–278.

Moffa-Sánchez, P., Hall, I. R., Barker, S., Thornalley, D. J., and Yashayaev, I. (2014b). Surface changes in the eastern Labrador Sea around the onset of the Little Ice Age. *Paleoceanography*, 29(3):160–175.

Moreno-Chamarro, E., Zanchettin, D., Lohmann, K., and Jungclaus, J. H. (2015). Internally generated decadal cold events in the northern North Atlantic and their possible implications for the demise of the Norse settlements in Greenland. *Geophysical Research Letters*, 42(3):908–915.

Moreno-Chamarro, E., Zanchettin, D., Lohmann, K., and Jungclaus, J. H. (2016). An abrupt weakening of the subpolar gyre as trigger of Little Ice Age-type episodes. *Climate Dynamics*, pages 1–18.

Ogilvie, A. E., Barlow, L. K., and Jennings, A. (2000). North Atlantic climate c. AD 1000: Millennial reflections on the Viking discoveries of Iceland, Greenland and North America. *Weather*, 55(2):34–45.

Ortega, P., Lehner, F., Swingedouw, D., Masson-Delmotte, V., Raible, C. C., Casado, M., and Yiou, P. (2015). A model-tested North Atlantic Oscillation reconstruction for the past millennium. *Nature*, 523(7558):71–74.

Otto-Bliesner, B. L., Brady, E. C., Fasullo, J., Jahn, A., Landrum, L., Stevenson, S., Rosenbloom, N., Mai, A., and Strand, G. (2015). Climate variability and change since 850 CE: An ensemble approach with the Community Earth System Model (CESM). *Bulletin of the American Meteorological Society*.

Pages 2k Consortium (2013). Continental-scale temperature variability during the past two millennia. *Nature Geoscience*, 6(5):339–346.

Palastanga, V., Van der Schrier, G., Weber, S., Kleinen, T., Briffa, K., and Osborn, T. (2011). Atmosphere and ocean dynamics: contributors to the European Little Ice Age? *Climate Dynamics*, 36(5-6):973–987.

Parker, D. E., Legg, T. P., and Folland, C. K. (1992). A new daily central England temperature series, 1772–1991. *International Journal of Climatology*, 12(4):317–342.

Patterson, W. P., Dietrich, K. A., Holmden, C., and Andrews, J. T. (2010). Two millennia of North Atlantic seasonality and implications for Norse colonies. *Proceedings of the National Academy of Sciences*, 107(12):5306–5310.

Pongratz, J., Reick, C., Raddatz, T., and Claussen, M. (2008). A reconstruction of global agricultural areas and land cover for the last millennium. *Global Biogeochemical Cycles*, 22(3).

Rahmstorf, S., Box, J. E., Feulner, G., Mann, M. E., Robinson, A., Rutherford, S., and Schaffernicht, E. J. (2015). Exceptional twentieth-century slowdown in Atlantic Ocean overturning circulation. *Nature Climate Change*.

Ran, L., Jiang, H., Knudsen, K. L., and Eiríksson, J. (2011). Diatom-based reconstruction of palaeoceanographic changes on the North Icelandic shelf during the last millennium. *Palaeogeography, Palaeoclimatology, Palaeoecology*, 302(1):109–119.

Scherrer, S. C., Croci-Maspoli, M., Schwierz, C., and Appenzeller, C. (2006). Two-dimensional indices of atmospheric blocking and their statistical relationship with winter climate patterns in the Euro-Atlantic region. *International journal of climatology*, 26(2):233–250.

Schleussner, C. and Feulner, G. (2013). A volcanically triggered regime shift in the subpolar North Atlantic Ocean as a possible origin of the Little Ice Age. *Climate of the Past*, 9(3):1321–1330.

Schleussner, C.-F., Divine, D., Donges, J., Miettinen, A., and Donner, R. (2015). Indications for a North Atlantic ocean circulation regime shift at the onset of the Little Ice Age. *Climate Dynamics*, 45(11-12):3623–3633.

Schmelzer, N. and Holfort, J. (2011). Ice winter severity in the western Baltic Sea in the period of 1301–1500: comparison with other relevant data. *International Journal of Climatology*, 31(7):1094–1098.

Schmidt, G. A., Jungclaus, J., Ammann, C., Bard, E., Braconnot, P., Crowley, T., Delaygue, G., Joos, F., Krivova, N., Muscheler, R., et al. (2011). Climate forcing reconstructions for use in PMIP simulations of the last millennium (v1.0). *Geoscientific Model Development*, 4(1):pp33–45.

Schurer, A. P., Tett, S. F., and Hegerl, G. C. (2014). Small influence of solar variability on climate over the past millennium. *Nature Geoscience*, 7(2):104–108.

Seager, R., Battisti, D. S., Yin, J., Gordon, N., Naik, N., Clement, A. C., and Cane, M. A. (2002). Is the Gulf Stream responsible for Europe's mild winters? *Quarterly Journal of the Royal Meteorological Society*, 128(586):2563–2586.

Sha, L., Jiang, H., Seidenkrantz, M.-S., Muscheler, R., Zhang, X., Knudsen, M. F., Olsen, J., Knudsen, K. L., and Zhang, W. (2016). Solar forcing as an important trigger for West Greenland sea-ice variability over the last millennium. *Quaternary Science Reviews*, 131:148–156.

Sicre, M.-A., Hall, I. R., Mignot, J., Khodri, M., Ezat, U., Truong, M.-X., Eiríksson, J., and Knudsen, K.-L. (2011). Sea surface temperature variability in the subpolar Atlantic over the last two millennia. *Paleoceanography*, 26(4).

Sicre, M.-A., Jacob, J., Ezat, U., Rousse, S., Kissel, C., Yiou, P., Eiríksson, J., Knudsen, K. L., Jansen, E., and Turon, J.-L. (2008). Decadal variability of sea surface temperatures off North Iceland over the last 2000 years. *Earth and Planetary Science Letters*, 268(1):137–142.

Sicre, M.-A., Weckström, K., Seidenkrantz, M.-S., Kuijpers, A., Benetti, M., Massé, G., Ezat, U., Schmidt, S., Bouloubassi, I., Olsen, J., et al. (2014). Labrador Current variability over the last 2000 years. *Earth and Planetary Science Letters*, 400:26–32.

Sigl, M., Winstrup, M., McConnell, J., Welten, K., Plunkett, G., Ludlow, F., Büntgen, U., Caffee, M., Chellman, N., Dahl-Jensen, D., et al. (2015). Timing and climate forcing of volcanic eruptions for the past 2,500 years. *Nature*, 523(7562):543–549.

Spielhagen, R. F., Werner, K., Sørensen, S. A., Zamelczyk, K., Kandiano, E., Budeus, G., Husum, K., Marchitto, T. M., and Hald, M. (2011). Enhanced modern heat transfer to the Arctic by warm Atlantic water. *Science*, 331(6016):450–453.

Stevens, B., Giorgetta, M., Esch, M., Mauritsen, T., Crueger, T., Rast, S., Salzmann, M., Schmidt, H., Bader, J., Block, K., et al. (2013). Atmospheric component of the MPI-M Earth System Model: ECHAM6. *Journal of Advances in Modeling Earth Systems*, 5(2):146–172.

Swingedouw, D., Terray, L., Servonnat, J., and Guiot, J. (2012). Mechanisms for European summer temperature response to solar forcing over the last millennium. *Climate of the Past*, 8(5):1487–1495.

Tarand, A. and Nordli, P.-Ø. (2001). The tallinn temperature series reconstructed back half a millennium by use of proxy data. In *The Iceberg in the Mist: Northern Research in pursuit of a Little Ice Age*, pages 189–199. Springer.

Tierney, J. E., Abram, N. J., Anchukaitis, K. J., Evans, M. N., Giry, C., Kilbourne, K. H., Saenger, C. P., Wu, H. C., and Zinke, J. (2015). Tropical sea surface temperatures for the past four centuries reconstructed from coral archives. *Paleoceanography*, 30(3):226–252.

Trigo, R., Trigo, I., DaCamara, C., and Osborn, T. (2004). Climate impact of the European winter blocking episodes from the NCEP/NCAR reanalyses. *Climate Dynamics*, 23(1):17–28.

Trouet, V., Esper, J., Graham, N. E., Baker, A., Scourse, J. D., and Frank, D. C. (2009). Persistent positive North Atlantic Oscillation mode dominated the Medieval Climate Anomaly. *Science*, 324(5923):78–80.

Verosub, K. L. and Lippman, J. (2008). Global impacts of the 1600 eruption of Peru's Huaynaputina volcano. *Eos, Transactions American Geophysical Union*, 89(15):141–142.

Vieira, L. E. A., Solanki, S. K., Krivova, N. A., and Usoskin, I. (2011). Evolution of the solar irradiance during the Holocene. *Astronomy & Astrophysics*, 531:A6.

Visbeck, M., Chassignet, E. P., Curry, R. G., Delworth, T. L., Dickson, R. R., and Krahmann, G. (2003). The ocean's response to North Atlantic Oscillation variability. *The North Atlantic Oscillation: climatic significance and environmental impact*, pages 113–145.

Von Storch, H. and Zwiers, F. W. (2001). *Statistical analysis in climate research*. Cambridge University press.

Wanamaker, A., Butler, P., Scourse, J., Heinemeier, J., Eiríksson, J., Knudsen, K., and Richardson, C. (2012). Surface changes in the North Atlantic meridional overturning circulation during the last millennium. *Nature Communications*, 3:899.

Wang, Y.-M., Lean, J., and Sheeley Jr, N. (2005). Modeling the Sun's magnetic field and irradiance since 1713. *The Astrophysical Journal*, 625(1):522.

Werner, K., Spielhagen, R. F., Bauch, D., Hass, H. C., Kandiano, E., and Zamelczyk, K. (2011). Atlantic Water advection to the eastern Fram Strait–Multiproxy evidence for late Holocene variability. *Palaeogeography, Palaeoclimatology, Palaeoecology*, 308(3):264–276.

Yashayaev, I. (2007). Hydrographic changes in the Labrador Sea, 1960–2005. *Progress in Oceanography*, 73(3):242–276.

Yoshimori, M., Raible, C. C., Stocker, T. F., and Renold, M. (2010). Simulated decadal oscillations of the Atlantic meridional overturning circulation in a cold climate state. *Climate Dynamics*, 34(1):101–121.

Young, N. E., Schweinsberg, A. D., Briner, J. P., and Schaefer, J. M. (2015). Glacier maxima in Baffin Bay during the Medieval Warm Period coeval with Norse settlement. *Science Advances*, 1(11):e1500806.

Zanchettin, D., Bothe, O., Graf, H. F., Lorenz, S. J., Luterbacher, J., Timmreck, C., and Jungclaus, J. H. (2013). Background conditions influence the decadal climate response to strong volcanic eruptions. *Journal of Geophysical Research: Atmospheres*, 118(10):4090–4106.

Zanchettin, D., Timmreck, C., Graf, H.-F., Rubino, A., Lorenz, S., Lohmann, K., Krüger, K., and Jungclaus, J. (2012). Bi-decadal variability excited in the coupled ocean–atmosphere system by strong tropical volcanic eruptions. *Climate Dynamics*, 39(1-2):419–444.

Zhong, Y., Miller, G., Otto-Bliesner, B., Holland, M., Bailey, D., Schneider, D., and Geirsdottir, A. (2011). Centennial-scale climate change from decadally-paced explosive volcanism: a coupled sea ice-ocean mechanism. *Climate Dynamics*, 37(11-12):2373–2387.

Acknowledgement

That I arrived at the very last station of this journey is undoubtedly because of all the help and inspiration I have received throughout these years. My biggest thanks go to my mentor and guide Dr. Johann H. Jungclaus, who was always tremendously generous with his time and advice. I could not have imagined having a better advisor for my Ph.D study. It was a pleasure and great honor to work for you!

I cannot thank Dr. Davide Zanchettin enough for his friendly guidance and expert advice, which have been invaluable throughout all stages of the work, and for his incisive comments on my writings. I apologize for not having always followed them all.

Special thanks are due to Dr. Katjia Lohmann for extended discussions and valuable suggestions which have contributed greatly to the improvement of this thesis.

I want to thank Prof. Dr. Jochem Marotzke for his very clear and fruitful comments as my Panel Chair. Thanks also to Prof. Dr. Gerhard Schmiedl for his help and enthusiasms regarding this work. I am very thankful to Dr. Helmuth Haak for his assistance with model-related problems. I greatly appreciate the support and excellent working conditions received from the Max Planck Society via Institute for Meteorology and its Research School.

I would also wish to express my gratitude to Dr. Antje Weitz, not only for her immense and precious work behind the scenes, but also for her advise, encouragement and, especially, friendship. Thanks to Christina Rieckers for her kind help to clarify all questions concerning health insurances, bank issues, and difficulties with the German language. My thanks also go out to the support I received from Wibke Böhm, Conny Kampmann, Kornelia Müller.

Last thanks are due to friends at the MPI: to Josiane Salame, first my buddy, and eventually my friend; to Rohit Ghosh, for many office hours and lunch breaks, and for proof-reading this thesis; to Becca Rolph, for introducing me into the world of running; to Marlene Klockmann for proof-reading this thesis; and to Lambert Rasche, Jan Ackmann, Victoria Naipal, Alberto Elizalde, Andreas Veira, Christopher Hedemann, Jessica Engels, Jong-yeon Park, Jörg Burdanowitz, Manita Chouksey, Miriam Ferrer González, Mirjana Sakradzija, and Zhuhua Li and many others for great fun during these years.

I will now continue in Spanish.

Quiero dedicar esta tesis a mis padres, Mercedes y Ángel, por todo su trabajo y esfuerzo sin el cual no hubiera podido llegar hasta aquí, así como por todo el apoyo que me han brindado durante estos años por Skype, teléfono, o en persona.

Gracias también a mi hermano, Arturo, así como a mis abuelos, tíos, primos y resto de familiares por su pequeño, pero impagable grano de arena a esta historia. Y en especial, a mi abuela.

Por último, agradecer a Antonio todo su amor, paciencia, ánimo, y, en definitiva, cada uno de los mil y un días que hemos pasado recorriendo juntos esta aventura.

Eidesstattliche Versicherung
Declaration of oath

Hiermit erklre ich an Eides statt, dass ich die vorliegende Dissertationsschrift selbst verfasst und keine anderen als die angegebenen Quellen und Hilfsmittel benutzt habe.
I hereby declare, on oath, that I have written the present dissertation by myself and have not used other than the acknowledged resources and aids.

Hamburg, den 18. April 2016

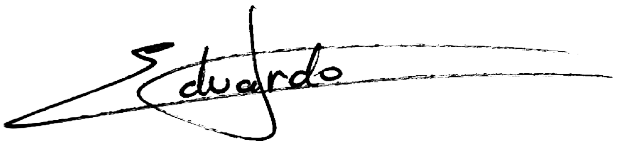

Eduardo Moreno Chamarro